

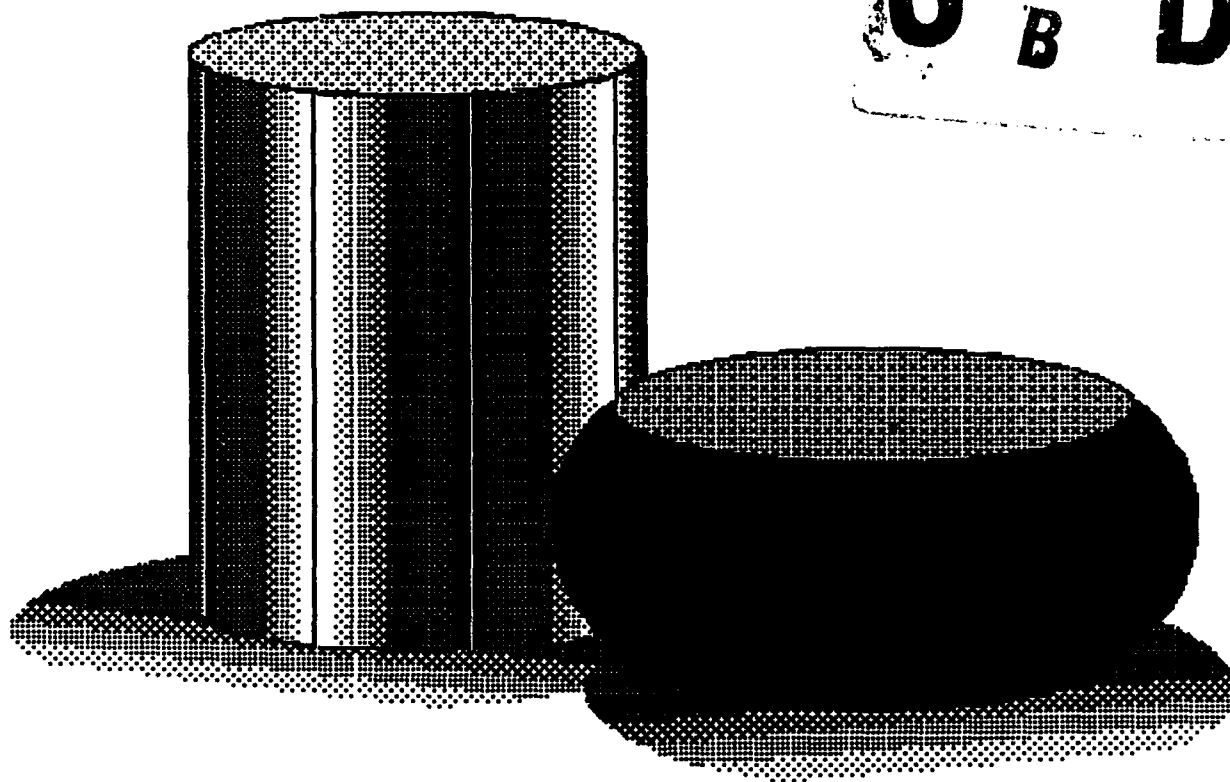
# Atlas of Formability

AD-A268 264



Nickelvac C-276

DTIC  
ELECTE  
AUG 18 1993  
S B D



DISTRIBUTION STATEMENT A  
Approved for public release  
Distribution Unlimited

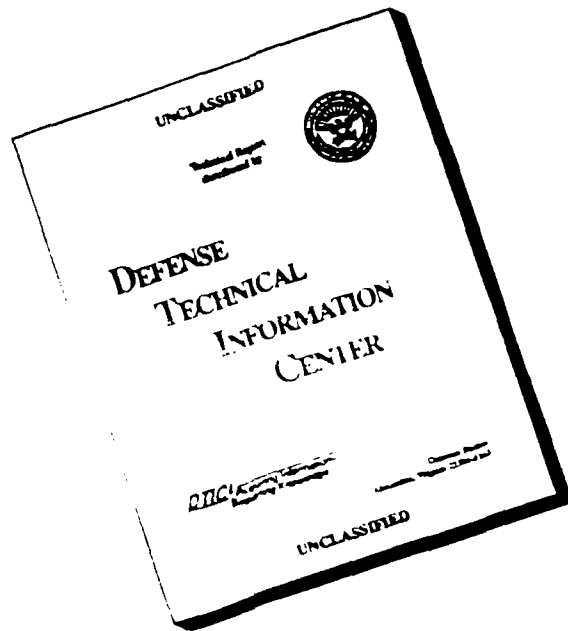
# NCEMT

93 8 16 0 0 1

93-18452



# DISCLAIMER NOTICE



THIS DOCUMENT IS BEST QUALITY AVAILABLE. THE COPY FURNISHED TO DTIC CONTAINED A SIGNIFICANT NUMBER OF PAGES WHICH DO NOT REPRODUCE LEGIBLY.

**ATLAS OF FORMABILITY**

**NICKELVAC C-276**

**by**

**Prabir K. Chaudhury and Dan Zhao**

**National Center for Excellence in Metalworking Technology  
1450 Scalp Avenue  
Johnstown, PA 15904**

**for**

**Naval Industrial Resource Support Activity  
Building 75-2, Naval Base  
Philadelphia, PA 19112-5078**

**November 30, 1992**

**The views, opinions, and/or findings contained in this report are those of the authors and should not be construed as an official Department of the Navy position, policy, or decision, unless so designated by other documentation**

REPORT DOCUMENTATION PAGE			Form Approved OMB No. 0704-0188	
Public reporting burden for this collection of information is estimated to average 1 hour per response, including the time for reviewing instructions, searching existing data sources, gathering and maintaining the data needed, and completing and reviewing the collection of information. Send comments regarding this burden estimate or any other aspect of this collection of information, including suggestions for reducing this burden, to Washington Headquarters Services, Directorate for Information Operations and Reports, 1215 Jefferson Davis Highway, Suite 1204, Arlington, VA 22202-4302, and to the Office of Management and Budget, Paperwork Reduction Project (0704-0188), Washington, DC 20503.				
1. AGENCY USE ONLY (Leave blank)	2. REPORT DATE November 30, 1992	3. REPORT TYPE AND DATES COVERED Final, Sept. 30, 1992 - Nov. 31, 1992		
4. TITLE AND SUBTITLE ATLAS OF FORMABILITY NICKELVAC C-276		5. FUNDING NUMBERS C-N00140-88-C-RC21		
6. AUTHOR(S) Prabir K. Chaudhury Dan Zhao				
7. PERFORMING ORGANIZATION NAME(S) AND ADDRESS(ES) National Center for Excellence in Metalworking Technology (NCEMT) 1450 Scalp Avenue Johnstown, PA 15904		8. PERFORMING ORGANIZATION REPORT NUMBER		
9. SPONSORING / MONITORING AGENCY NAME(S) AND ADDRESS(ES) Naval Industrial Resources Support Activity Building 75-2, Naval Base Philadelphia, PA 19112-5078		10. SPONSORING / MONITORING AGENCY REPORT NUMBER		
11. SUPPLEMENTARY NOTES				
12a. DISTRIBUTION / AVAILABILITY STATEMENT		12b. DISTRIBUTION CODE		
13. ABSTRACT (Maximum 200 words)  In this investigation, flow behavior of Nickelvac C-276 alloy was studied by conducting compression tests over a wide range of temperatures (950 - 1200 C) and strain rates (0.001 - 20 s <sup>-1</sup> ). The true stress-true strain flow curves are presented for each test condition. Constitutive relations were determined from the flow behavior, and a dynamic material modeling was performed on this alloy. Thus, the optimum processing condition in terms of temperature and strain rate was identified as 1075 C and 0.001 s <sup>-1</sup> for this alloy. Microstructural changes during high temperature deformation were also characterized, and selective micrographs are presented together with corresponding flow curves. Dynamic recrystallization and grain growth occurred during high temperature deformation over the range of temperatures tested. The recrystallization is complete at 1050 C and 0.001 s <sup>-1</sup> . This report supplies ample mechanical property and microstructure data on Nickelvac C-276 alloy for engineers in the field of metalworking process design. The data presented here are also essential in finite element analysis of metalworking processes.				
14. SUBJECT TERMS Nickelvac C-276, Deformation Processing, High Temperature Deformation, Processing Map, Metalworking, Microstructure			15. NUMBER OF PAGES 68	
			16. PRICE CODE	
17. SECURITY CLASSIFICATION OF REPORT Unclassified	18. SECURITY CLASSIFICATION OF THIS PAGE Unclassified	19. SECURITY CLASSIFICATION OF ABSTRACT Unclassified	20. LIMITATION OF ABSTRACT	

## TABLE OF CONTENTS

<b>Introduction</b> . . . . .	1
<b>Experimental Procedure</b> . . . . .	1
<b>Results</b> . . . . .	1
<b>Summary</b> . . . . .	64
<b>Implementation of Data Provided by the Atlas of Formability</b> . . . . .	64

DTIC QUALITY INSPECTED 3

ST #A, AUTH USNAVIRSA (MR PLONSKY 8/443-6684)  
PER TELECON, 17 AUG 93 CB

<b>Accession For</b>	
NTIS GRA&I	<input checked="" type="checkbox"/>
DTIC TAB	<input type="checkbox"/>
Unannounced	<input type="checkbox"/>
Justification	
By <i>per Telecon</i>	
Distribution/	
Availability Codes	
Dist	Avail and/or Special
<i>A-1</i>	

## LIST OF TABLE

Table 1. List of figures, testing conditions and microstructural observations for Nickelvac C-276 . . . . .	2
--	---

# Nickelvac C-276

## Introduction

Nickelvac C-276 alloy is known for its high strength retention and oxidation resistance at elevated temperatures. The alloy has a high resistance to pitting and crevice corrosion due to its higher molybdenum content. In many applications, the alloy is selected because of its capability to withstand severe corrosion conditions. The understanding of mechanical and microstructural behavior during high temperature deformation is very important for the forming processes of this material. In this investigation, flow behavior of Nickelvac C-276 was studied by conducting compression tests at various temperatures and strain rates. Constitutive relations were determined from the flow behavior and then, a dynamic material modeling for this alloy was performed. Thus, the optimum processing conditions in terms of temperature and strain rate were determined. Microstructural changes during high temperature deformation were also characterized to aid process design engineers to select processing conditions in terms of resulting microstructure.

## Experimental Procedure

The material used in this investigation was commercially available Nickelvac C-276 solution treated at 1135 C for half an hour and water quenched. The typical microstructure of the as-received material consists of twinned uniform equiaxed grains with an average size of 131  $\mu\text{m}$  (ASTM 2.5) as shown in Figure 1. The chemical composition is as follows (wt%), Ni (bal.):

C	S	Mn	Si	Cr	Co	Fe	Mo	W	V	P
0.002	0.0005	0.41	0.04	15.19	0.30	5.05	15.03	3.22	0.23	0.022

Cylindrical compression test specimens with a diameter of 12.7 mm and a height of 15.9 mm were machined from the bars. Isothermal compression tests were conducted on an MTS testing machine in vacuum. The test matrix was as follows:

Temperature, C (F): 950 (1742), 1000 (1832), 1050 (1922), 1100 (2012), 1125 (2057), 1150 (2102), and 1200 (2192);

Strain rate,  $\text{s}^{-1}$ : 0.001, 0.01, 0.05, 0.1, 0.5, 1, 5 and 20.

Load and stroke data from the tests were acquired by a computer and later converted to true stress-true strain curves. Immediately after the compression test, the specimens were quenched with forced helium gas in order to retain the deformed microstructure. Longitudinal sections of the specimens were examined by optical microscopy. The photomicrographs presented were taken from the center of the longitudinal section of the specimens.

## Results

Table 1 is a list of the figures, test conditions and the observed microstructures. The true stress-true strain flow curves with selective corresponding deformed microstructure are shown in Figure 2 to Figure 57. True stress versus strain rate was plotted in log-log scale in Figure 58 at a true strain of 0.5. The slope of the plot gives the strain rate sensitivity  $m$ , which is not constant over the range of strain rate tested. Log stress vs.  $1/T$  at the same true strain is shown in Figure 59. A processing map at this strain was developed and is shown in Figure 60. The optimum processing condition from the map can be obtained by selecting the temperature and strain rate combination which provides the maximum efficiency in the stable region. This condition is approximately 1075 C and  $10^{-3} \text{ s}^{-1}$  for this material.

Table 1. List of figures, testing conditions and microstructural observations for Nickelvac C-276

Figure No	Temperature C (F)	Strain Rate s <sup>-1</sup>	Microstructure	Page No
			Optical Microscopy	
1	As received		Large equiaxed grains presenting extensive twinning. A uniform grain size of 131 $\mu\text{m}$ (2.5 ASTM) was measured.	4
2	950 (1742)	0.001	Deformed grains showing necklacing at the grain boundaries. An aspect ratio of 3:1 was measured in the strained grains.	5
3	950 (1742)	0.01		6
4	950 (1742)	0.05	Same as above, but there is lesser amount of necklacing.	7
5	950 (1742)	0.1		8
6	950 (1742)	0.5		9
7	950 (1742)	1	Same as above.	10
8	950 (1742)	5		11
9	950 (1742)	20	Same as above. Dynamic recovery is shown by the presence of sub-grain formation in the deformed grains.	12
10	1000 (1882)	0.001	More than 60% of the microstructure is recrystallized (subgrain size $\sim 9.7\mu\text{m}$ ).	13
11	1000 (1882)	0.01		14
12	1000 (1882)	0.05		15
13	1000 (1882)	0.1	Same as above, but more than 60 % of the deformed grains have a substructure with a subgrain size of $\sim 11\mu\text{m}$ .	16
14	1000 (1882)	0.5		17
15	1000 (1882)	1	Similar microstructure as above. However, the twin boundaries show complete recrystallization.	18
16	1000 (1882)	5		19
17	1000 (1882)	20	Same as above, but $\sim 60\%$ of the strained grains have a substructure (subgrain size $\sim 9\mu\text{m}$ ).	20
18	1050 (1922)	0.001	100% recrystallized equiaxed grains. Approximately 95% of the grains are small and have a size of $\sim 35\mu\text{m}$ . The larger grains have a size $> 100\mu\text{m}$ . There is also the presence of some twins.	21
19	1050 (1922)	0.01		22
20	1050 (1922)	0.05	Approximately 70% of the microstructure shows recrystallized equiaxed grains with an average size of 10 $\mu\text{m}$ . The new recrystallized grains have fewer twins. 30% of the grains are still deformed.	23
21	1050 (1922)	0.1		24
22	1050 (1922)	0.5		25
23	1050 (1922)	1	Elongated grains and approximately 60% of the microstructure consists of new recrystallized equiaxed grains with a non-uniform size (average size was estimated $\sim 18\mu\text{m}$ ). Very little twinning was observed.	26
24	1050 (1922)	5		27
25	1050 (1922)	20	$\sim 40\%$ recrystallization. The new equiaxed grains have an irregular size (approximately 15 $\mu\text{m}$ ) and present extensive twinning.	28



26	1100 (1212)	0.001	100 % recrystallized equiaxed grains with a non-uniform size (average ~60 $\mu\text{m}$ ). Twinning is present in the microstructure.	29
27	1100 (1212)	0.01	Same as above, but smaller grain size (average ~50 $\mu\text{m}$ ).	30
28	1100 (1212)	0.05		31
29	1100 (1212)	0.1	Fully recrystallized equiaxed grains with an irregular size ranging from 10 to 68 $\mu\text{m}$ . However, the majority of the grains have an average size of 24 $\mu\text{m}$ . Approximately 10 % of the equiaxed grains have a size of 68 $\mu\text{m}$ .	32
30	1100 (1212)	0.5		33
31	1100 (1212)	1	More than 95% of the microstructure has recrystallized equiaxed grains with a non-uniform grain size. The new grains show twinning.	34
32	1100 (1212)	5		35
33	1100 (1212)	20	More than 75 % of the microstructure has deformed grains with an aspect ratio of ~2:1, and necklacing at the grain boundaries is observed. 100% recrystallization at the twin boundaries is observed.	36
34	1125 (2057)	0.001	100% recrystallized equiaxed grains with a non-uniform grain size (average ~54 $\mu\text{m}$ ). Twinning is also observed.	37
35	1125 (2057)	0.01		38
36	1125 (2057)	0.05	100% recrystallized equiaxed grains with a non-uniform size (average ~45 $\mu\text{m}$ ). Twins are also present.	39
37	1125 (2057)	0.1		40
38	1125 (2057)	0.5		41
39	1125 (2057)	1	Same as above, but the average grain size is smaller than 45 $\mu\text{m}$ .	42
40	1125 (2057)	5		43
41	1125 (2057)	20	100 % recrystallized equiaxed grains with a non-uniform size (also smaller than 45 $\mu\text{m}$ ). Some twinning is also present.	44
42	1150 (2102)	0.001	100% recrystallized equiaxed grains with a non-uniform grain size (average ~65 $\mu\text{m}$ ). Some twins are also present in the microstructure.	45
43	1150 (2102)	0.01	Same as above, but the average grain size is approximately 50 $\mu\text{m}$	46
44	1150 (2102)	0.05		47
45	1150 (2102)	0.1	Same as above, but the average grain size is smaller than 50 $\mu\text{m}$	48
46	1150 (2102)	0.5		49
47	1150 (2102)	1	100% recrystallized equiaxed grains with a non-uniform grain size ( average ~45 $\mu\text{m}$ ). There is also some twinning.	50
48	1150 (2102)	5		51
49	1150 (2102)	20	Same as above, but grain size smaller than 45 $\mu\text{m}$ ).	52
50	1200 (2192)	0.001	100% recrystallized equiaxed grains with a grain size ranging from 39 $\mu\text{m}$ to 220 $\mu\text{m}$ . The smaller proportion is within the 39 $\mu\text{m}$ range and, the majority have an average size of 82 $\mu\text{m}$ . There is also the presence of some twinning .	53
51	1200 (2192)	0.01		54
52	1200 (2192)	0.05	Same as above, but smaller grain size.	55

53	1200 (2192)	0.1	100% recrystallized equiaxed grains with a grain size ranging from 30 to 158 $\mu\text{m}$ . The larger proportion is within the 50 $\mu\text{m}$ range and, the majority have an average size of 70 $\mu\text{m}$ . There is also some twinning.	56
54	1200 (2192)	0.5		57
55	1200 (2192)	1	Same as above, but the average grain size is smaller	58
56	1200 (2192)	5		59
57	1200 (2192)	20	100% recrystallized equiaxed grains with a non-uniform grain size. (average $\sim 42$ $\mu\text{m}$ ). Fairly uniform twinning is present.	60

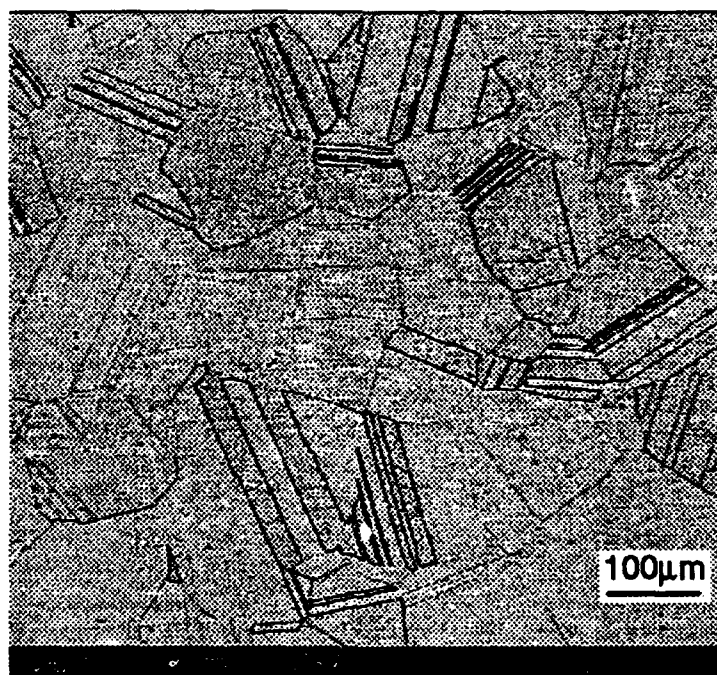


Figure 1. As-received microstructure of Nickelvac C-276.

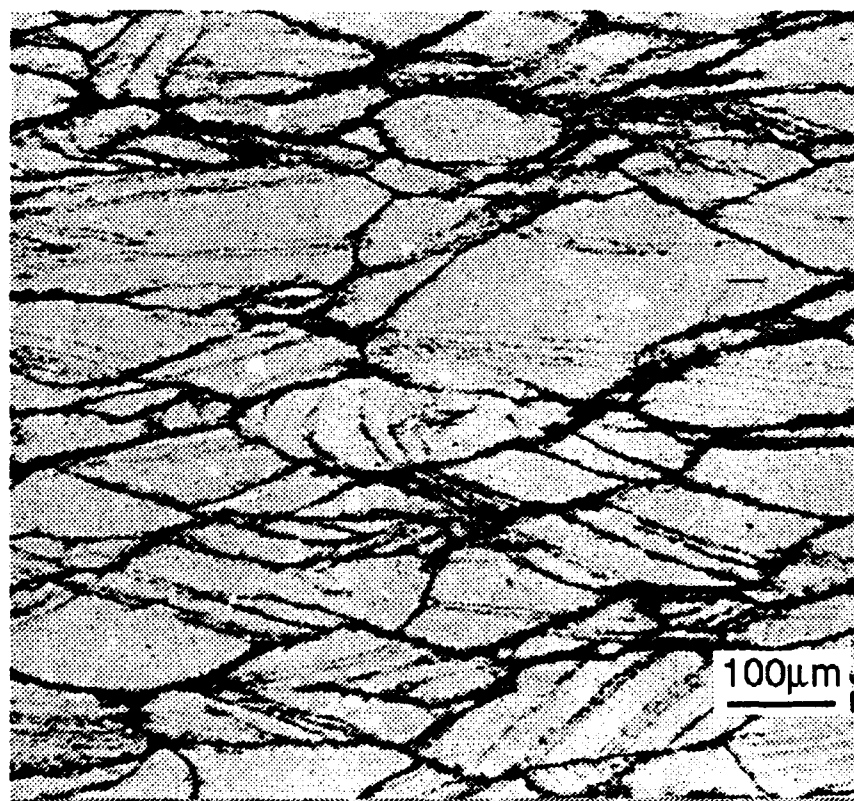
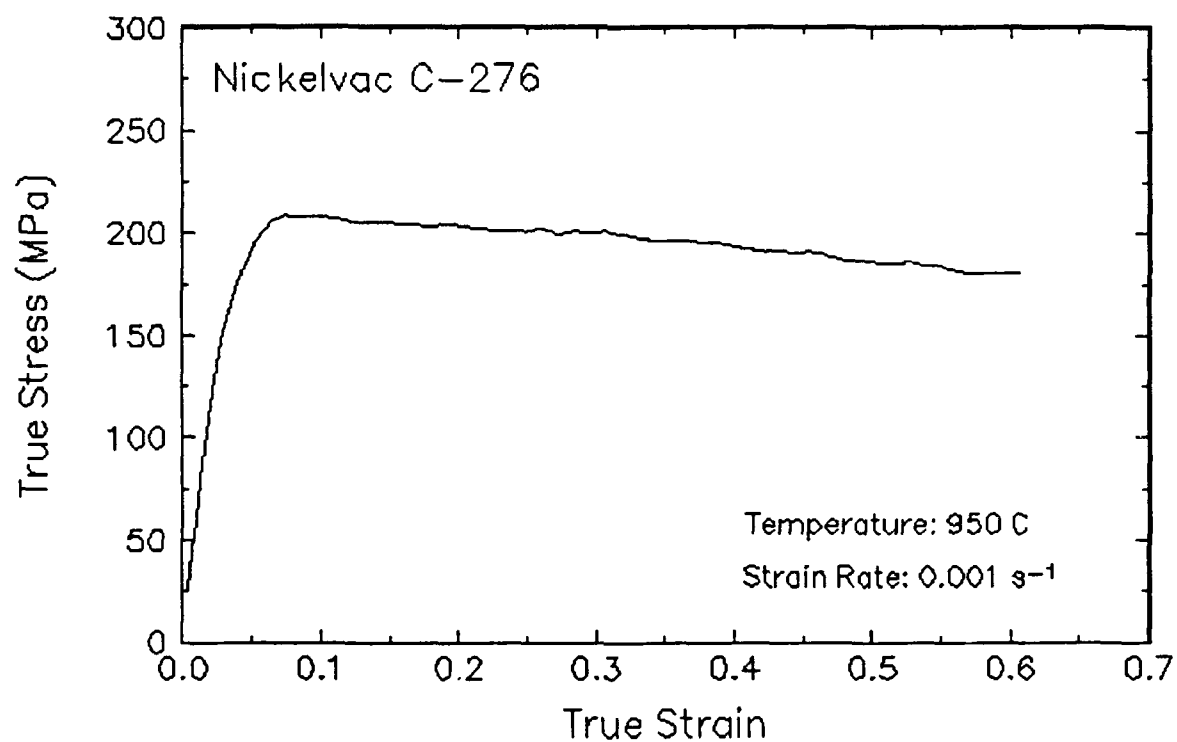


Figure 2. True stress-true strain curve and an optical micrograph from the center of the compressed sample cut through the compression axis, 950 C and 0.001 s<sup>-1</sup>.

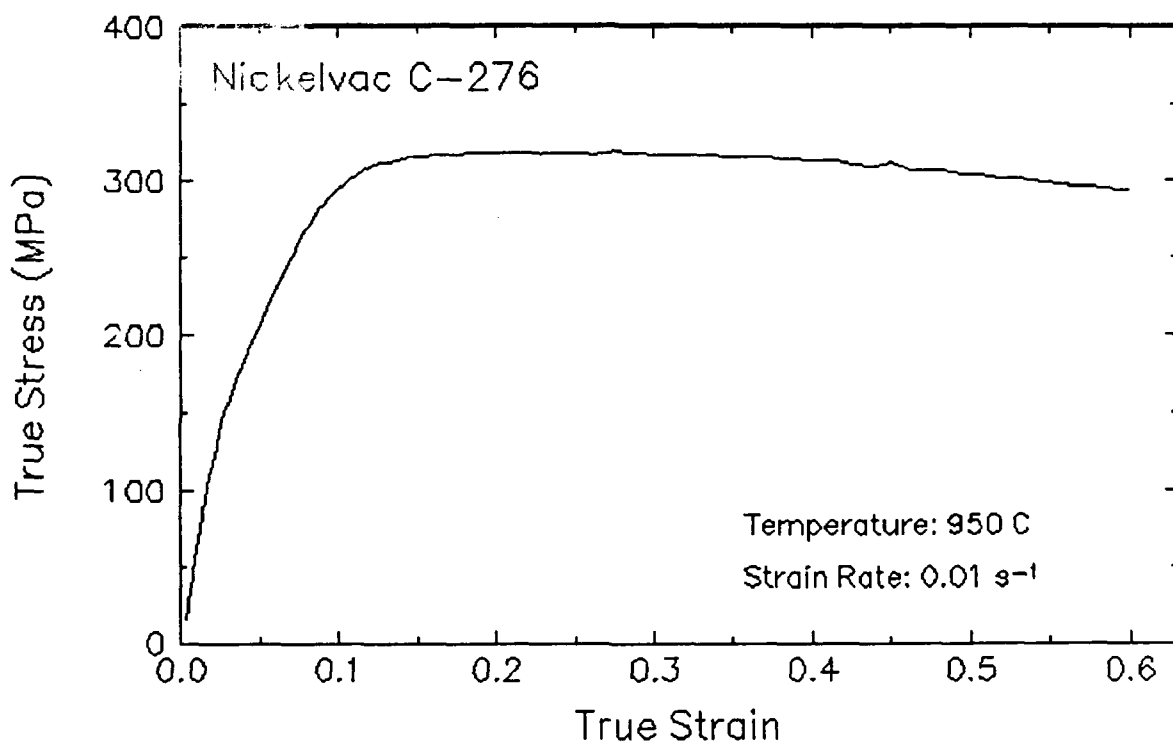


Figure 3. True stress-true strain curve 950 C and 0.01 s<sup>-1</sup>.

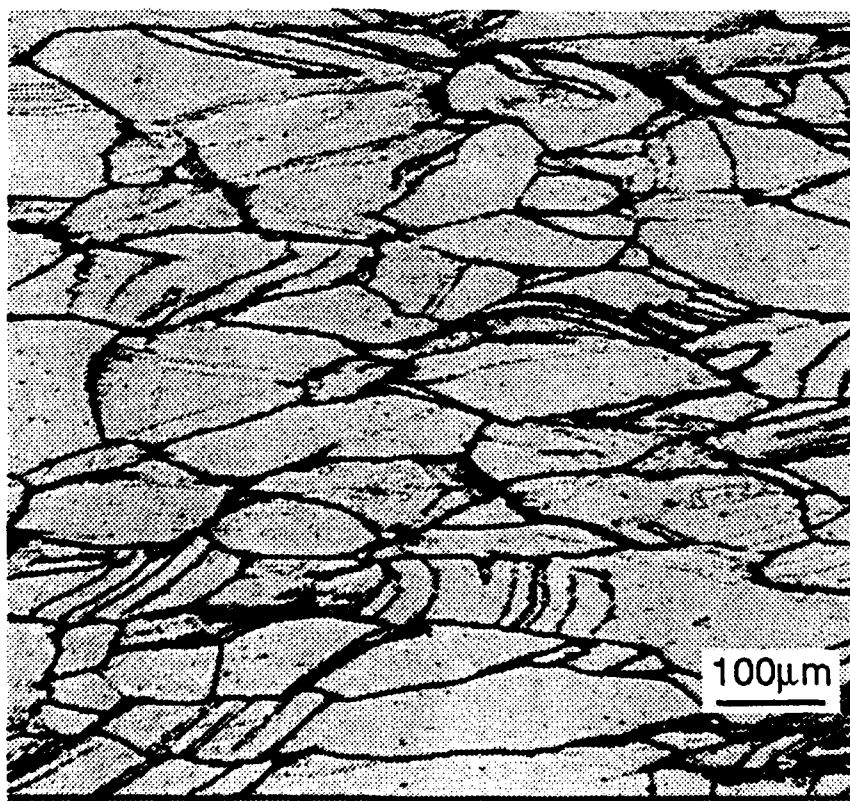
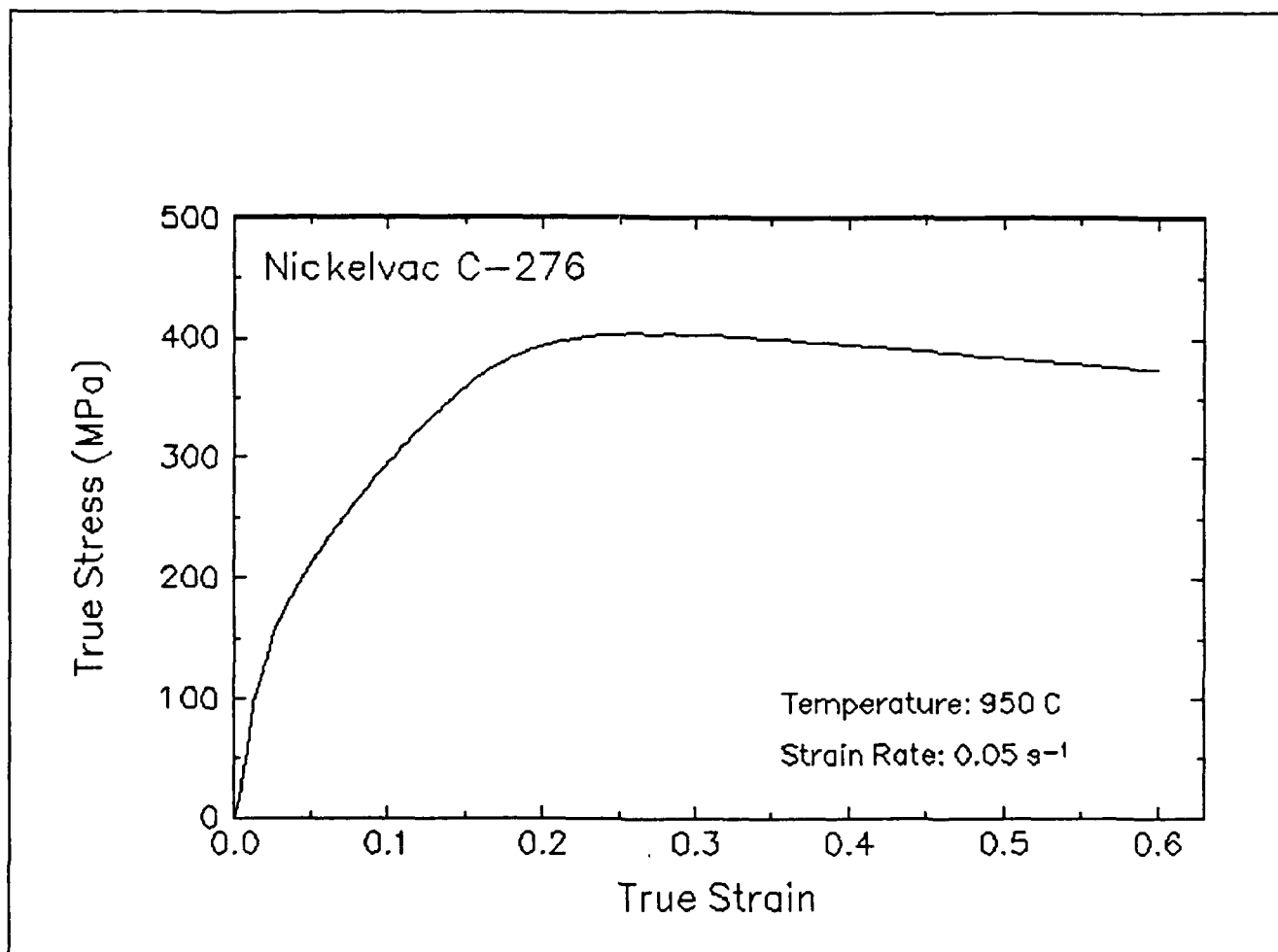


Figure 4. True stress-true strain curve and an optical micrograph from the center of the compressed sample cut through the compression axis, 950 C and 0.05 s<sup>-1</sup>.

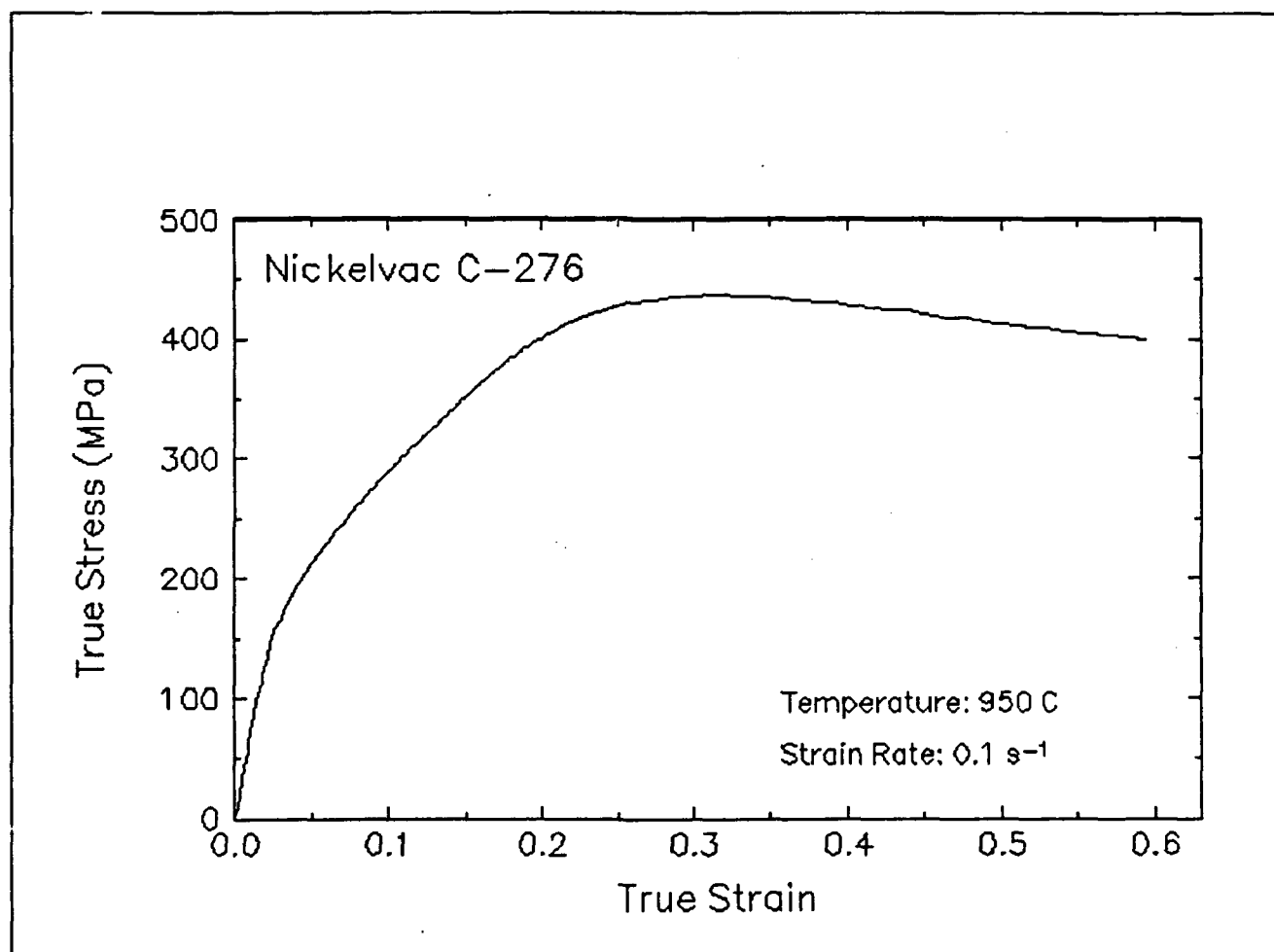


Figure 5. True stress-true strain curve, 950 C and 0.1 s<sup>-1</sup>.

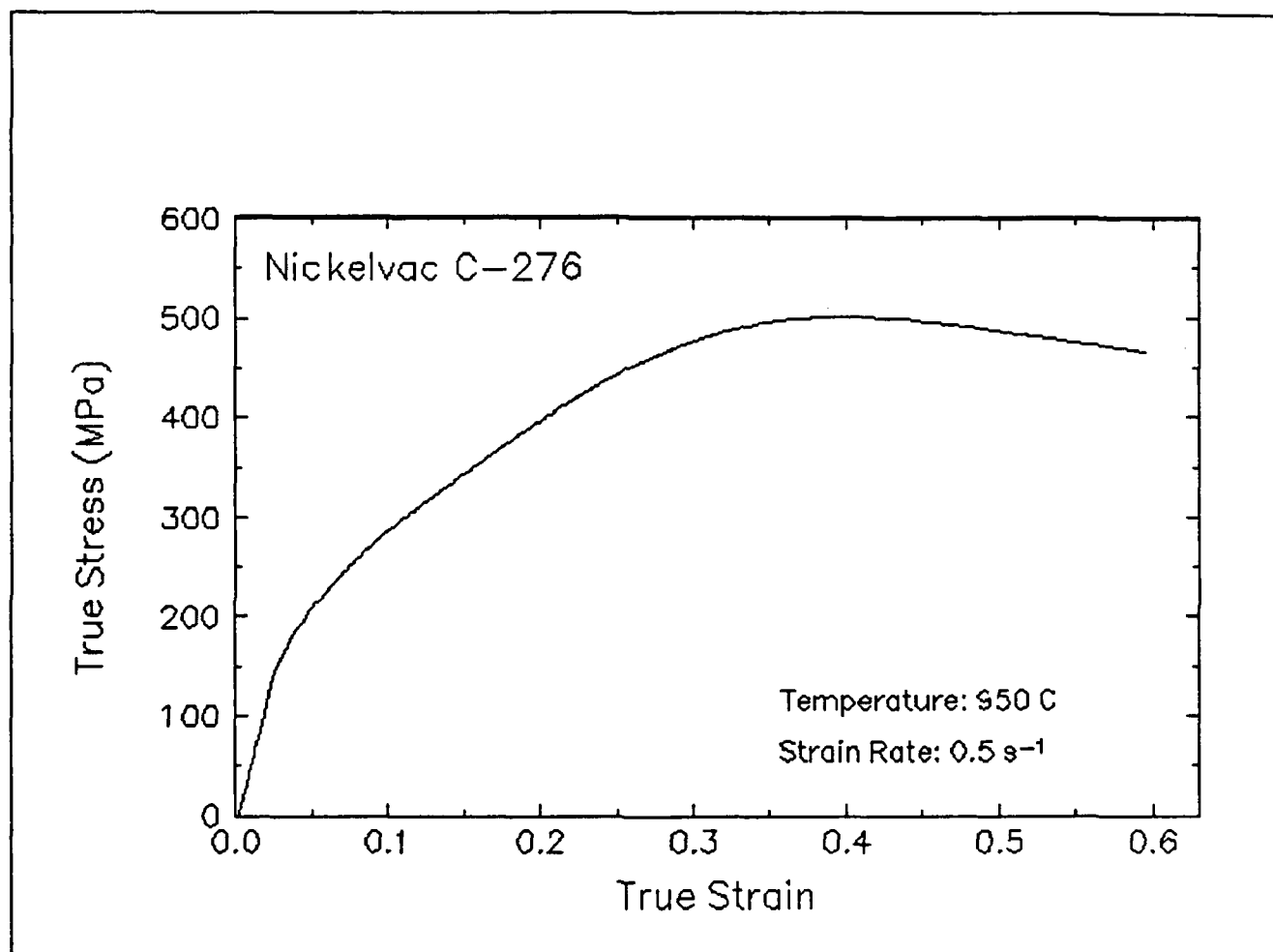


Figure 6. True stress-true strain curve, 950 C and 0.5 s<sup>-1</sup>.

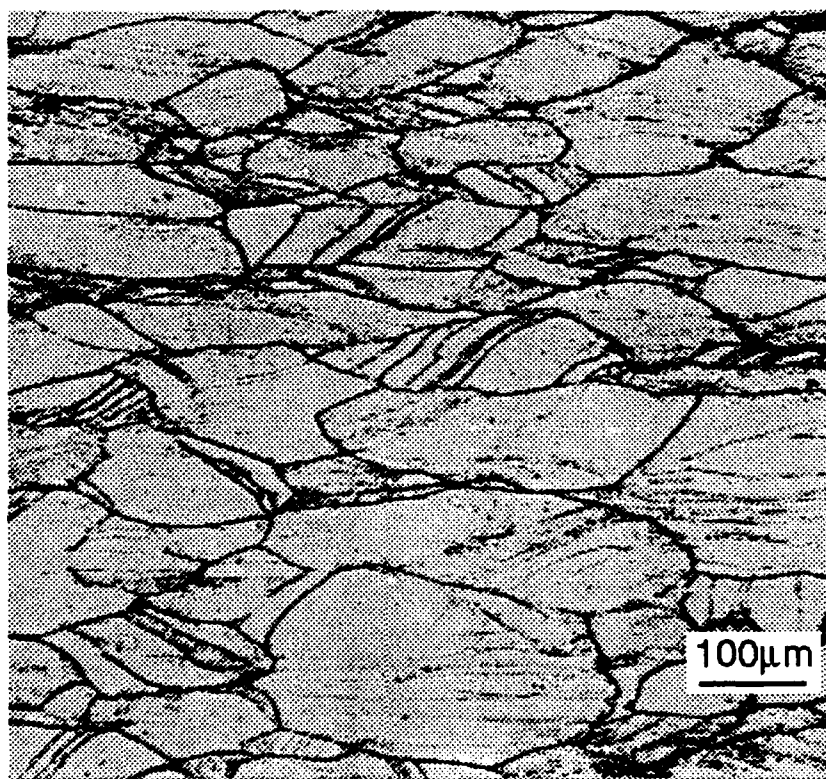
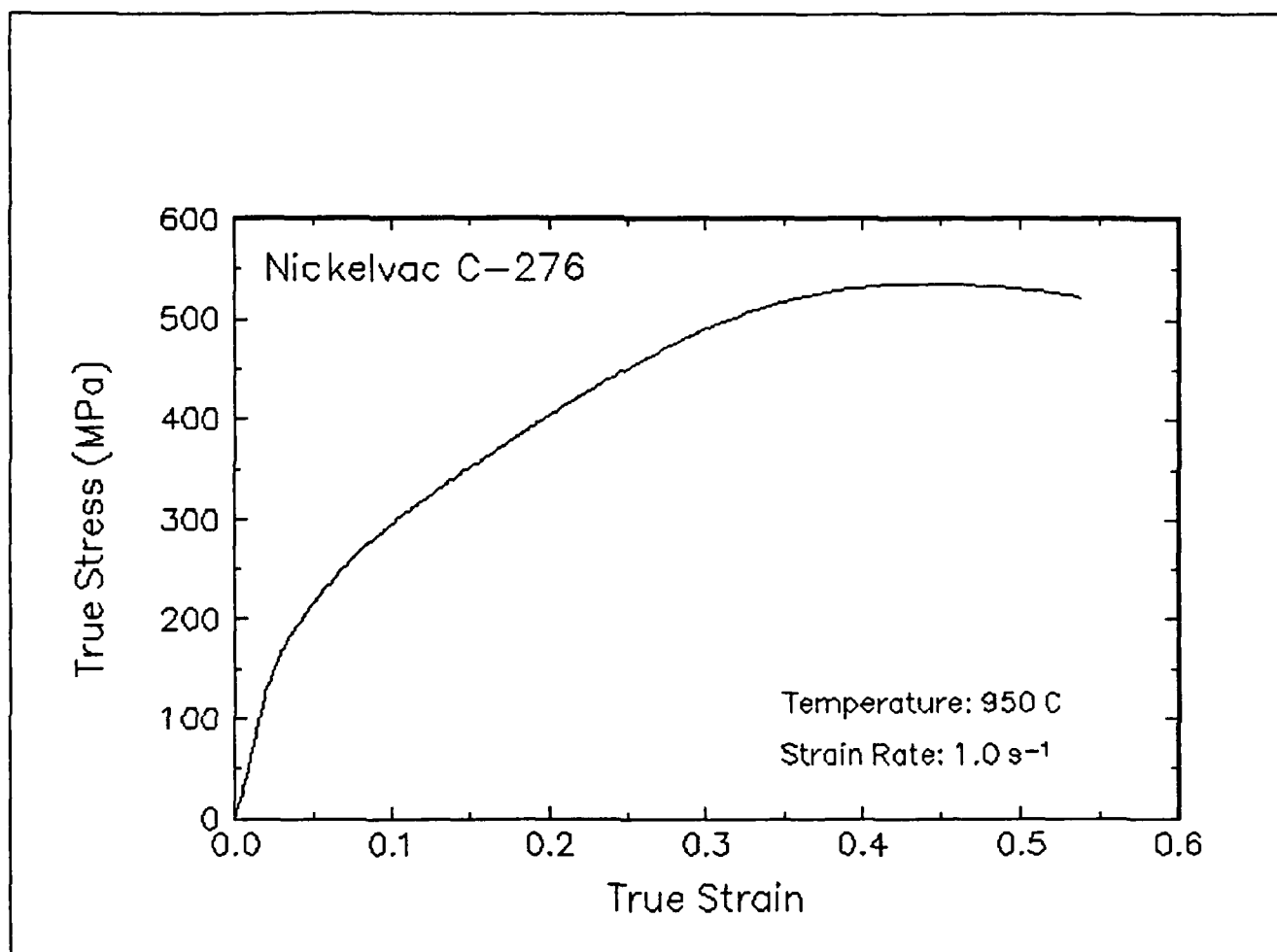


Figure 7. True stress-true strain curve and an optical micrograph from the center of the compressed sample cut through the compression axis, 950 C and 1 s<sup>-1</sup>.



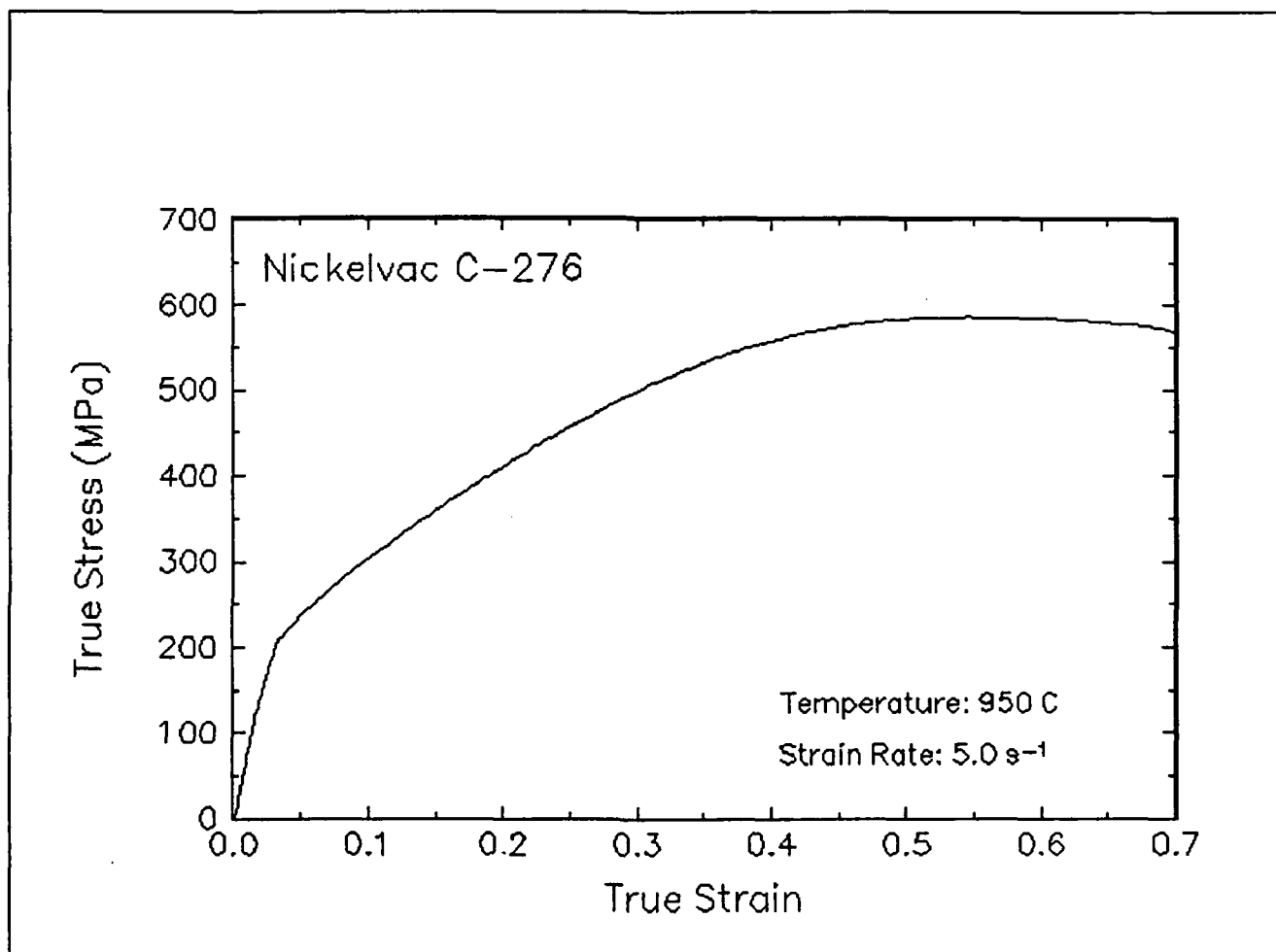


Figure 8. True stress-true strain curve, 950 C and 5 s<sup>-1</sup>.

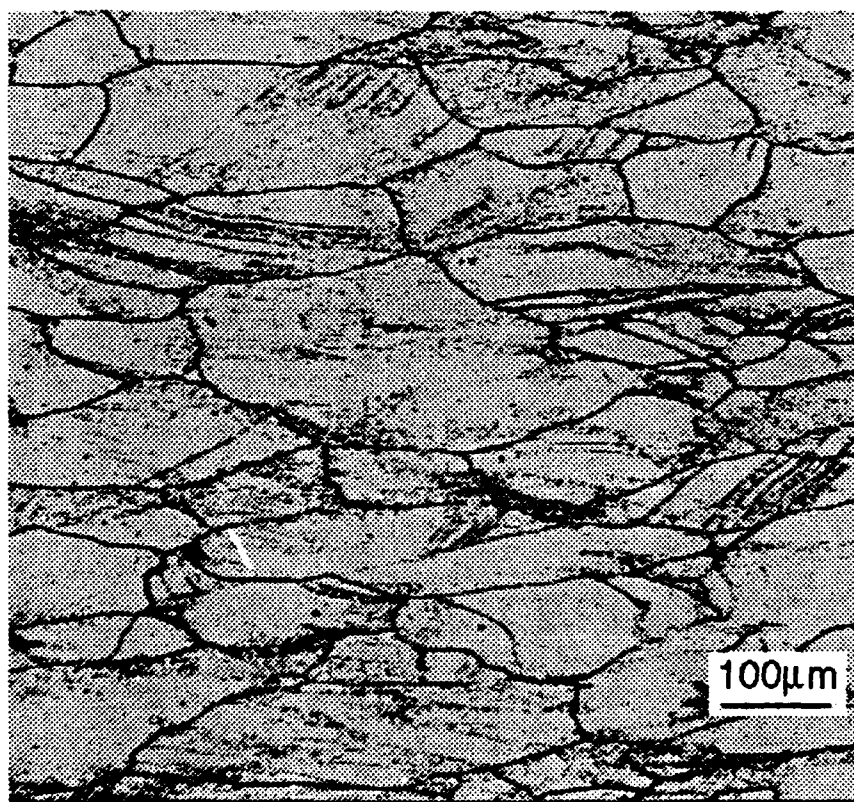
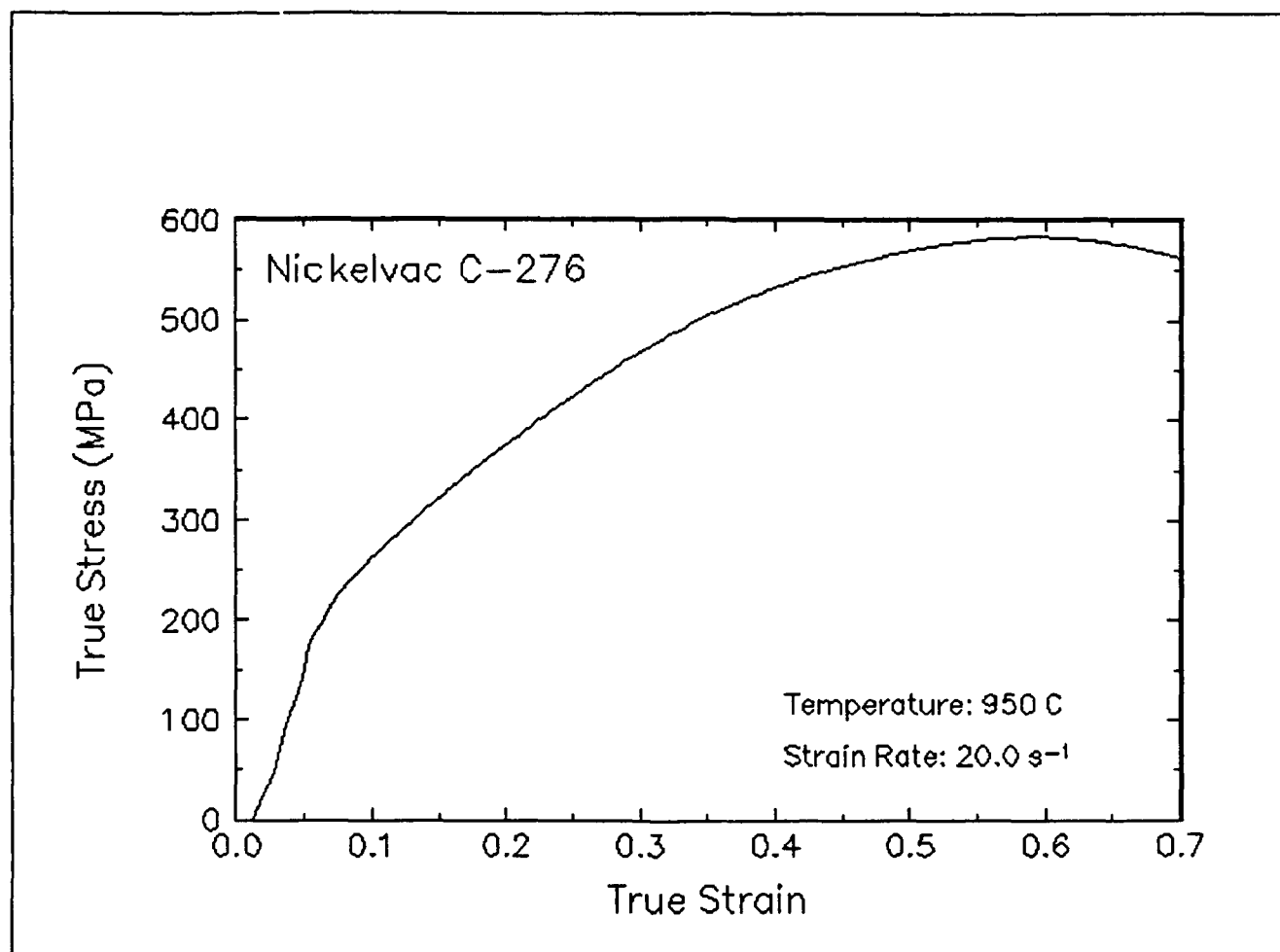


Figure 9. True stress-true strain curve and an optical micrograph from the center of the compressed sample cut through the compression axis, 950 C and 20 s<sup>-1</sup>.

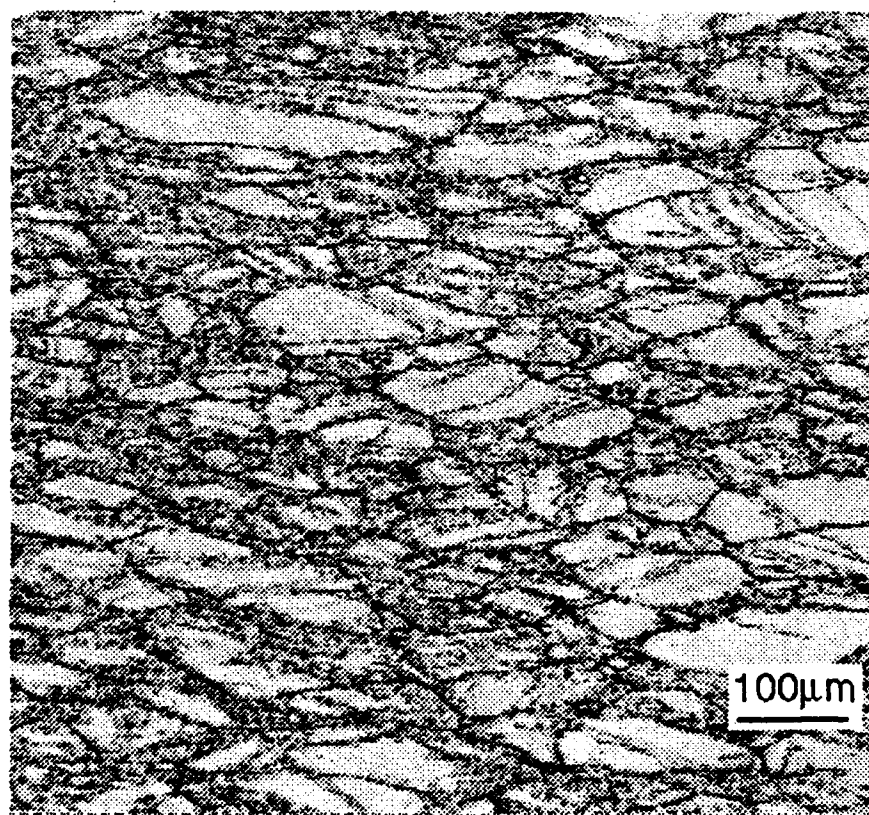
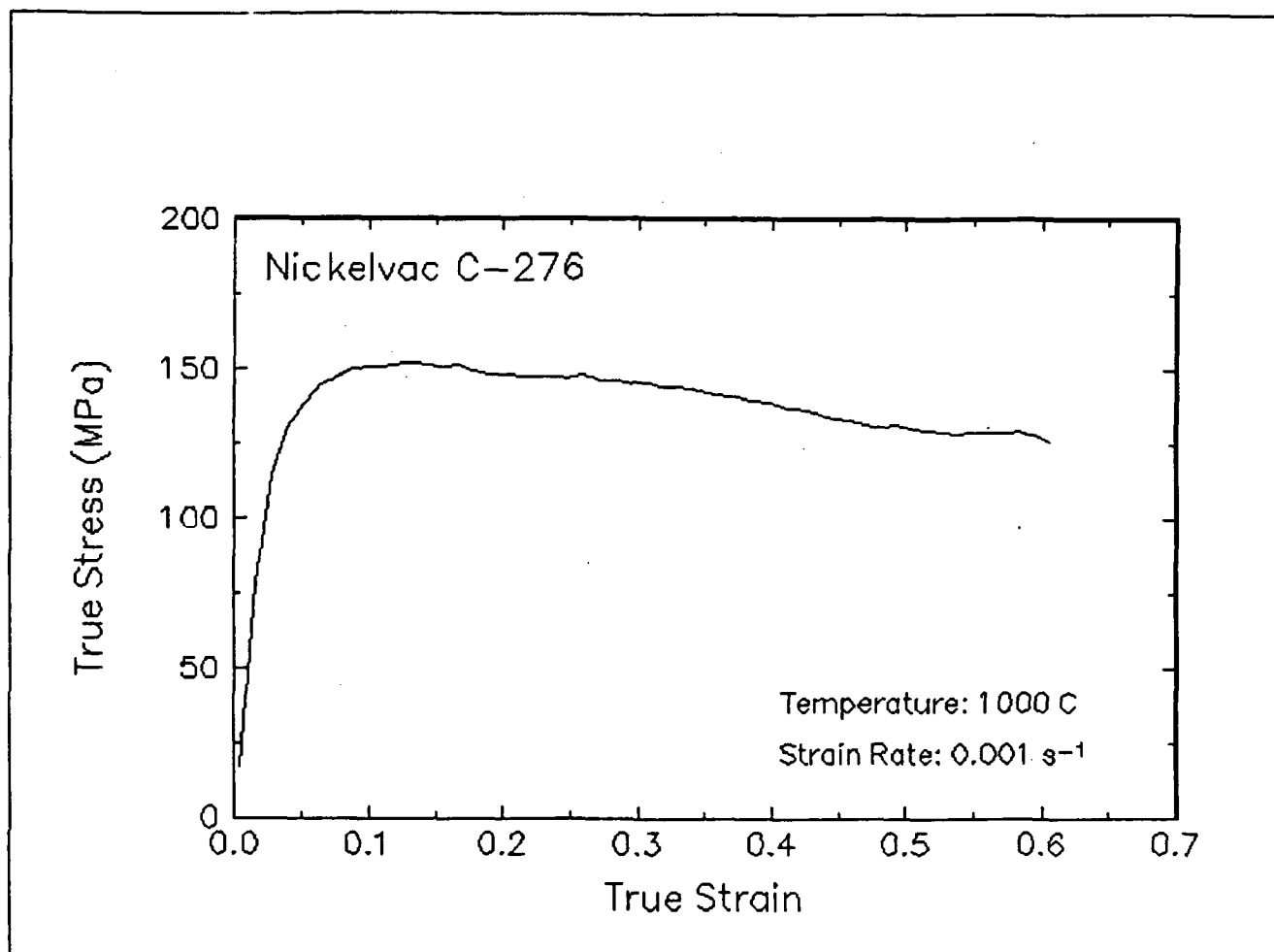


Figure 10. True stress-true strain curve and an optical micrograph from the center of the compressed sample cut through the compression axis, 1000 C and 0.001 s<sup>-1</sup>.

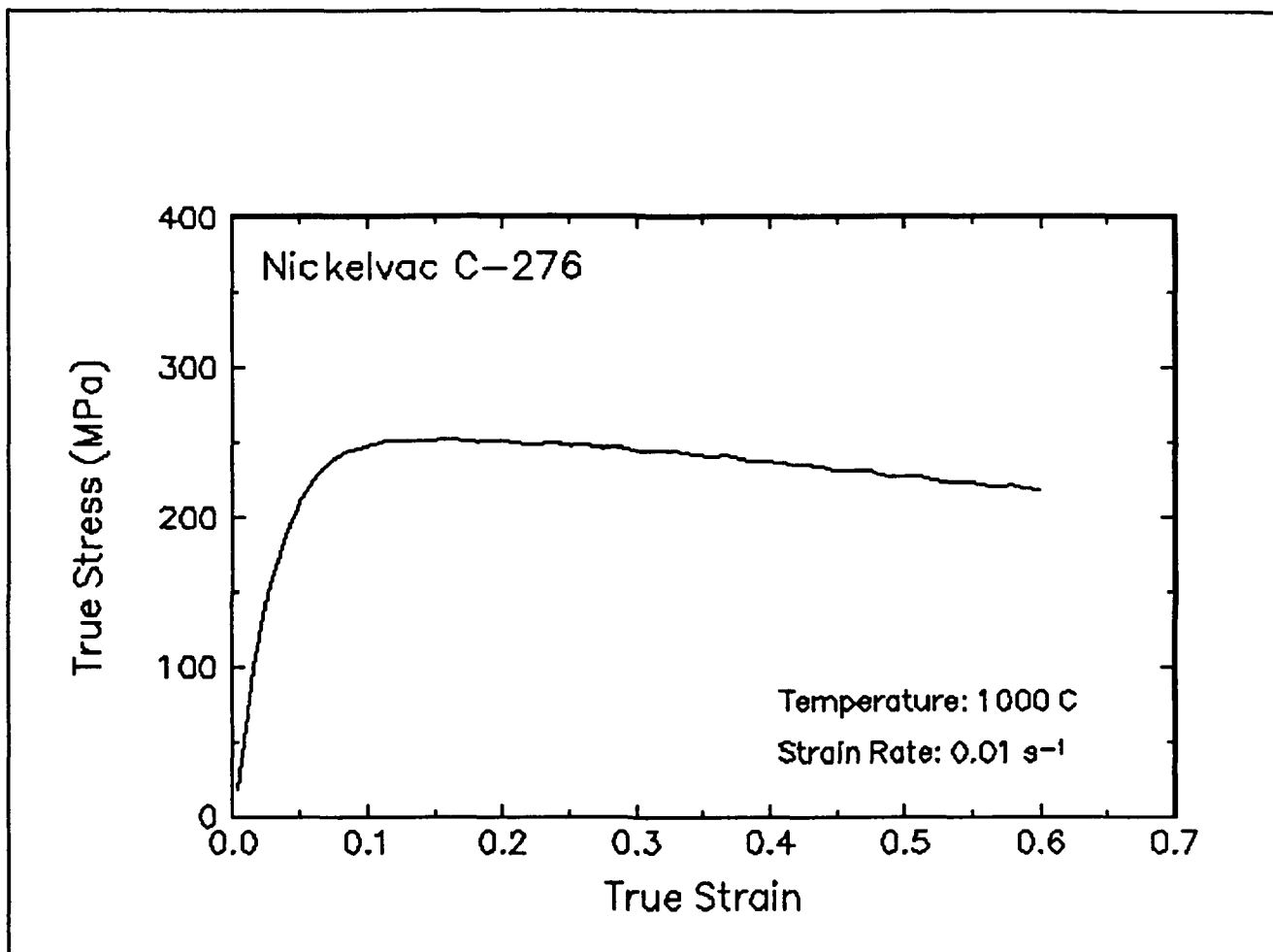


Figure 11. True stress-true strain curve, 1000 C and 0.01 s<sup>-1</sup>.

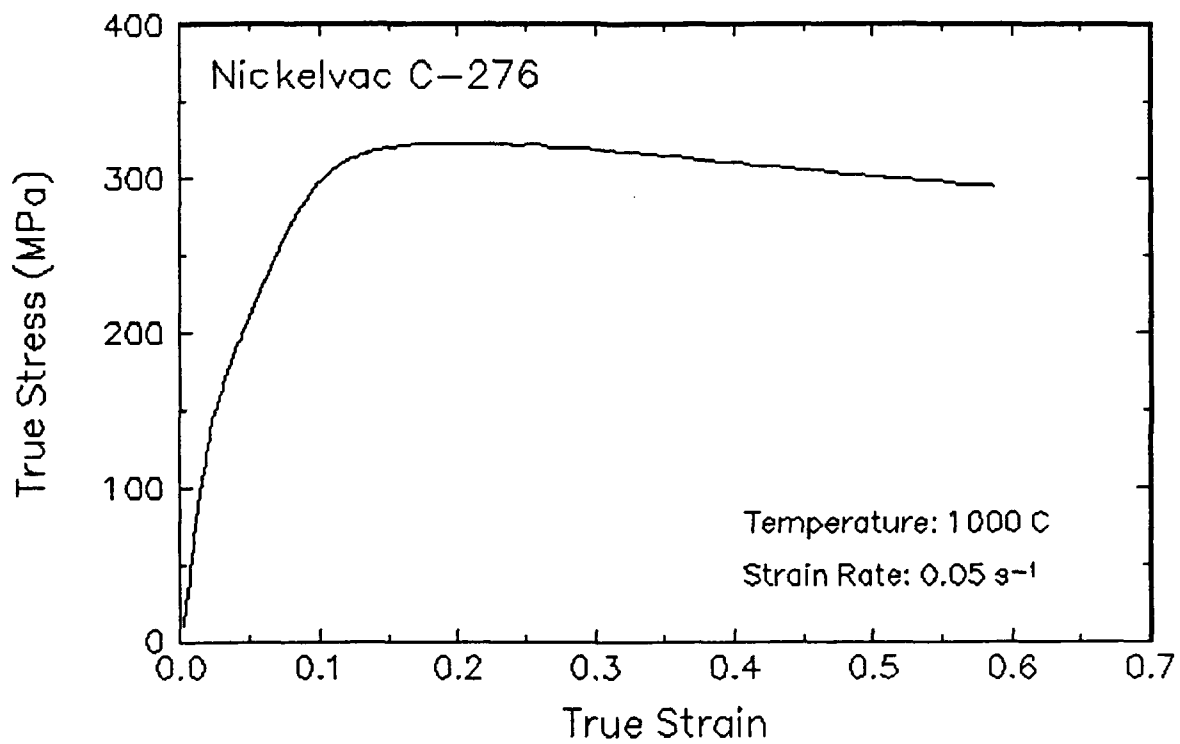


Figure 12. True stress-true strain curve, 1000 C and 0.05 s<sup>-1</sup>.

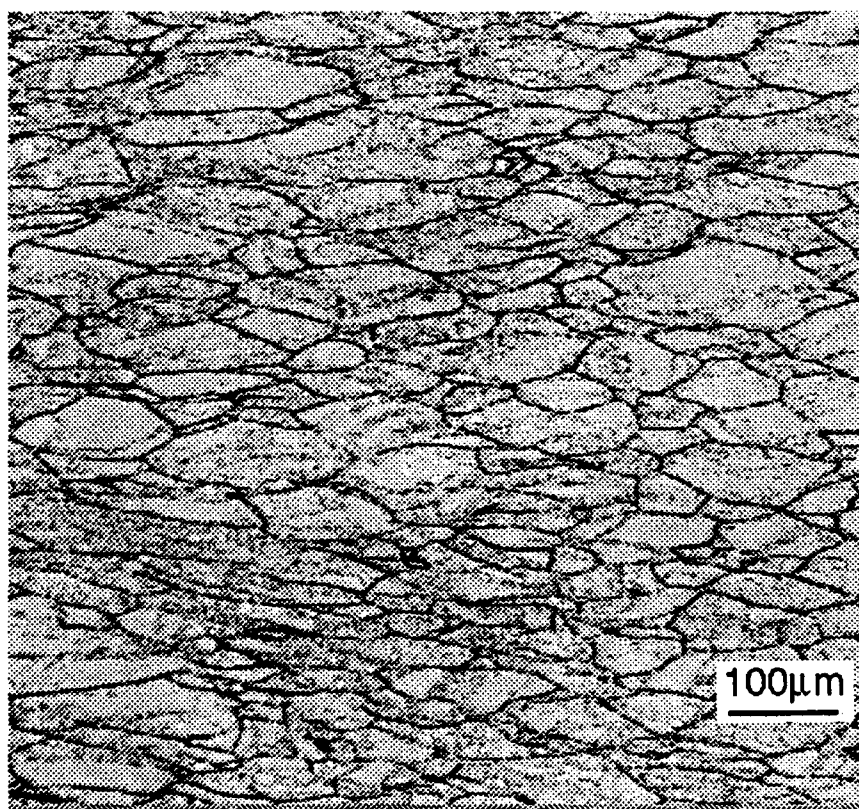
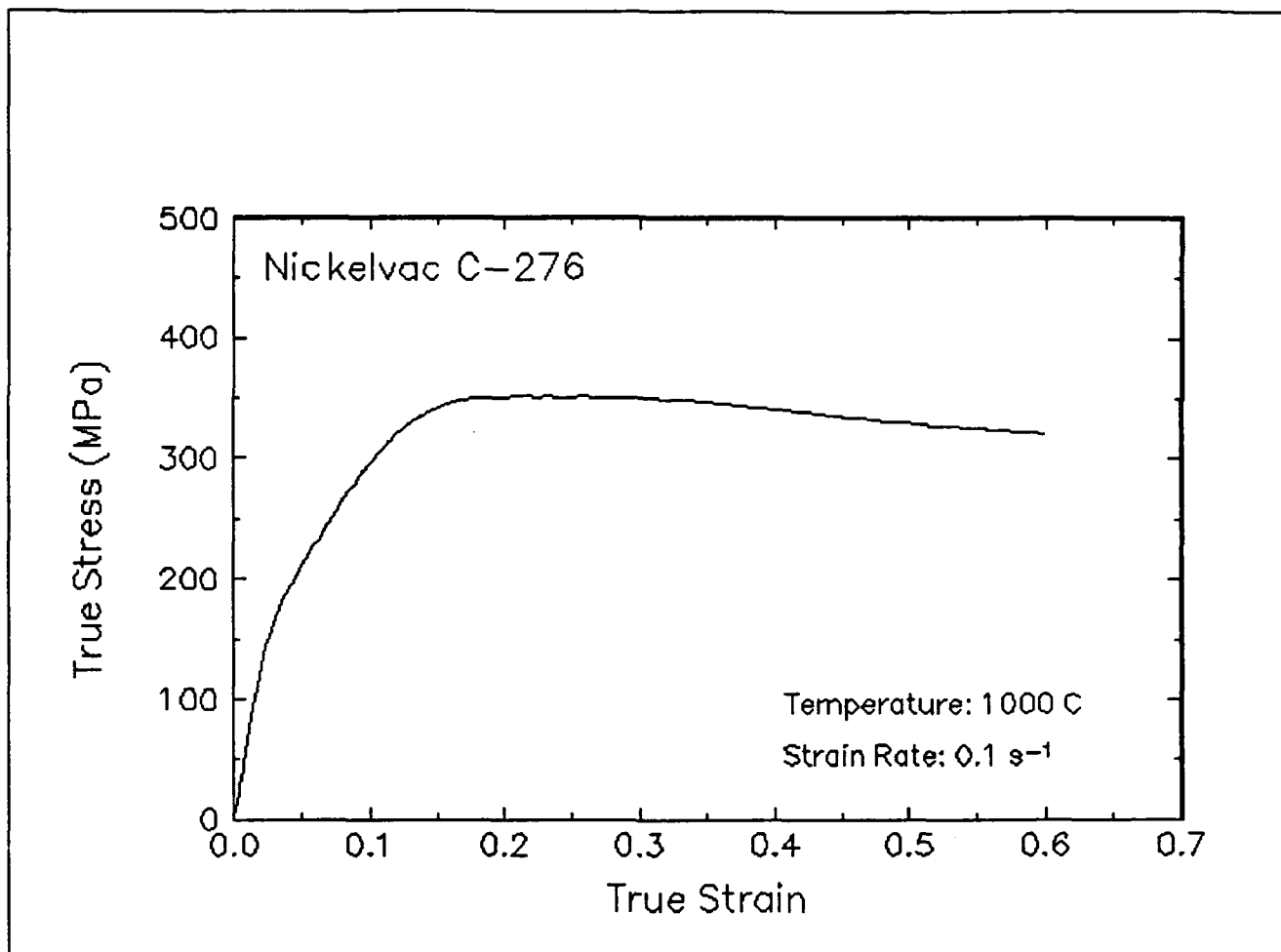


Figure 13. True stress-true strain curve and an optical micrograph from the center of the compressed sample cut through the compression axis, 1000 C and 0.1 s<sup>-1</sup>.

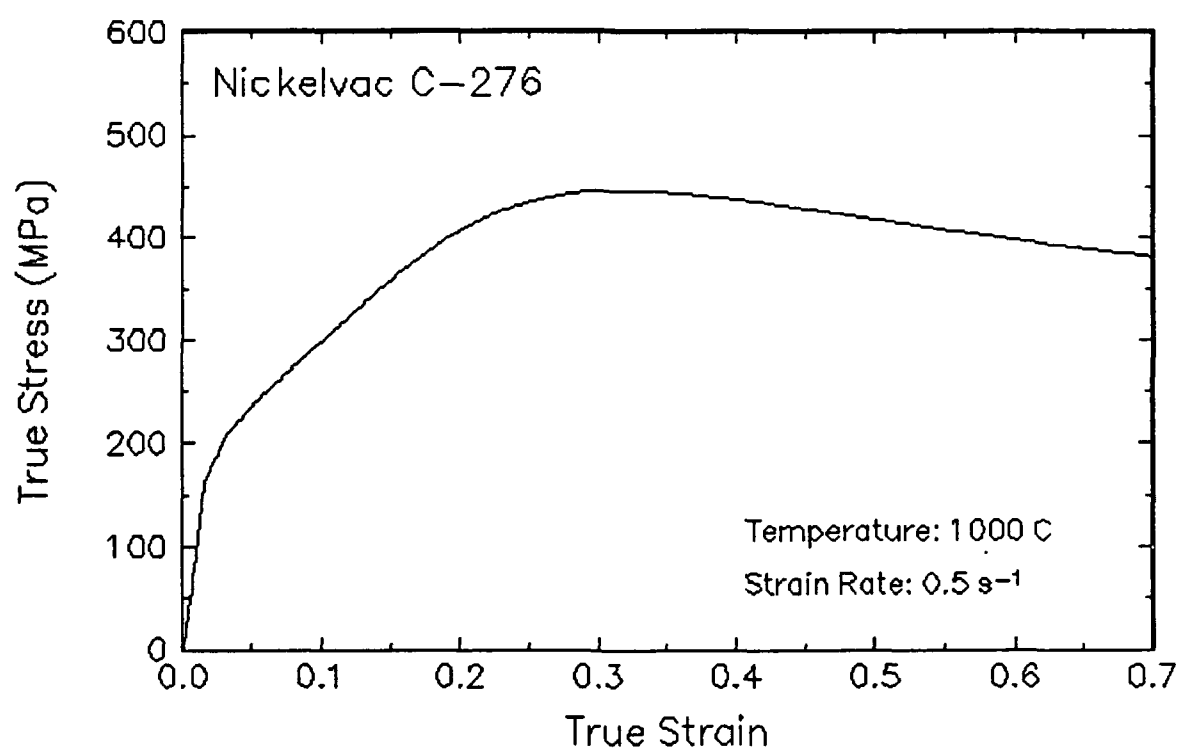


Figure 14. True stress-true strain curve, 1000 C and 0.5 s<sup>-1</sup>.

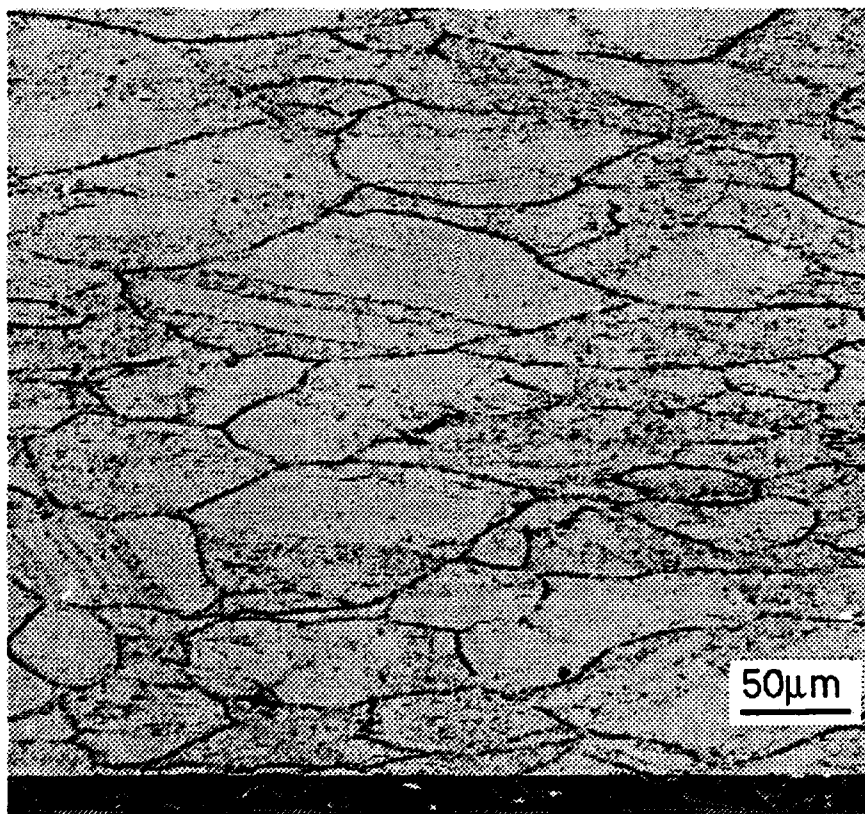
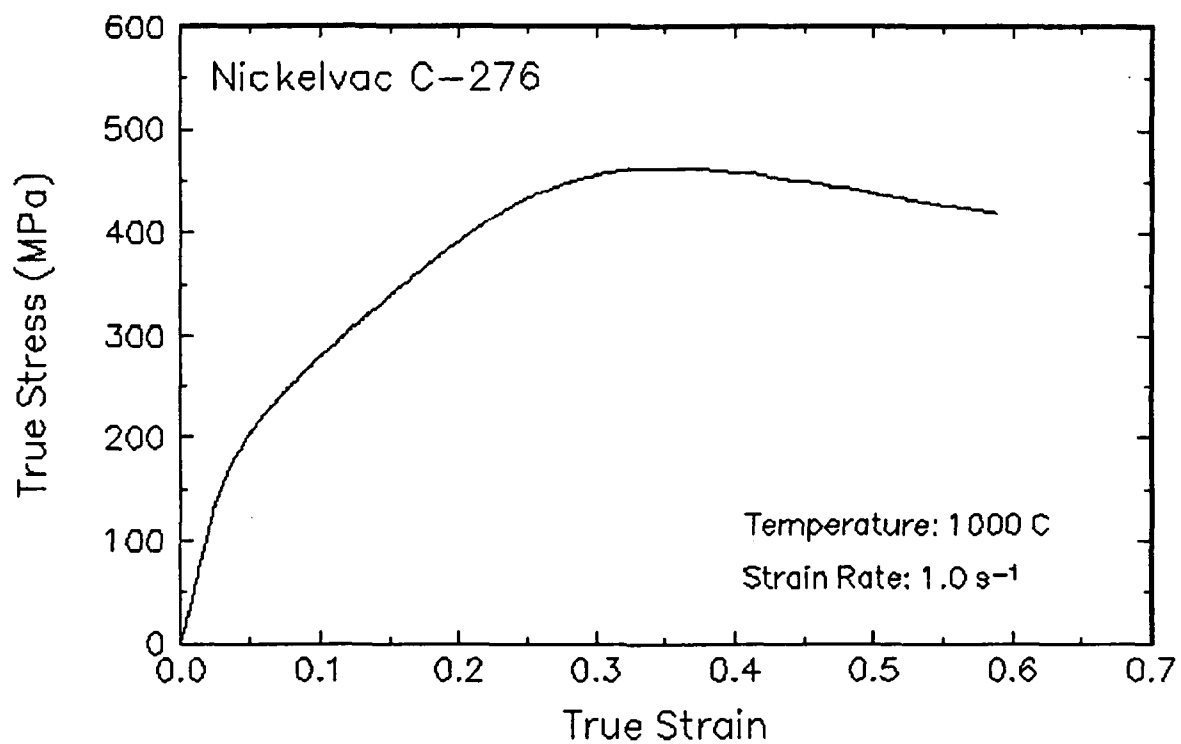


Figure 15. True stress-true strain curve and an optical micrograph from the center of the compressed sample cut through the compression axis, 1000 C and 1 s<sup>-1</sup>.



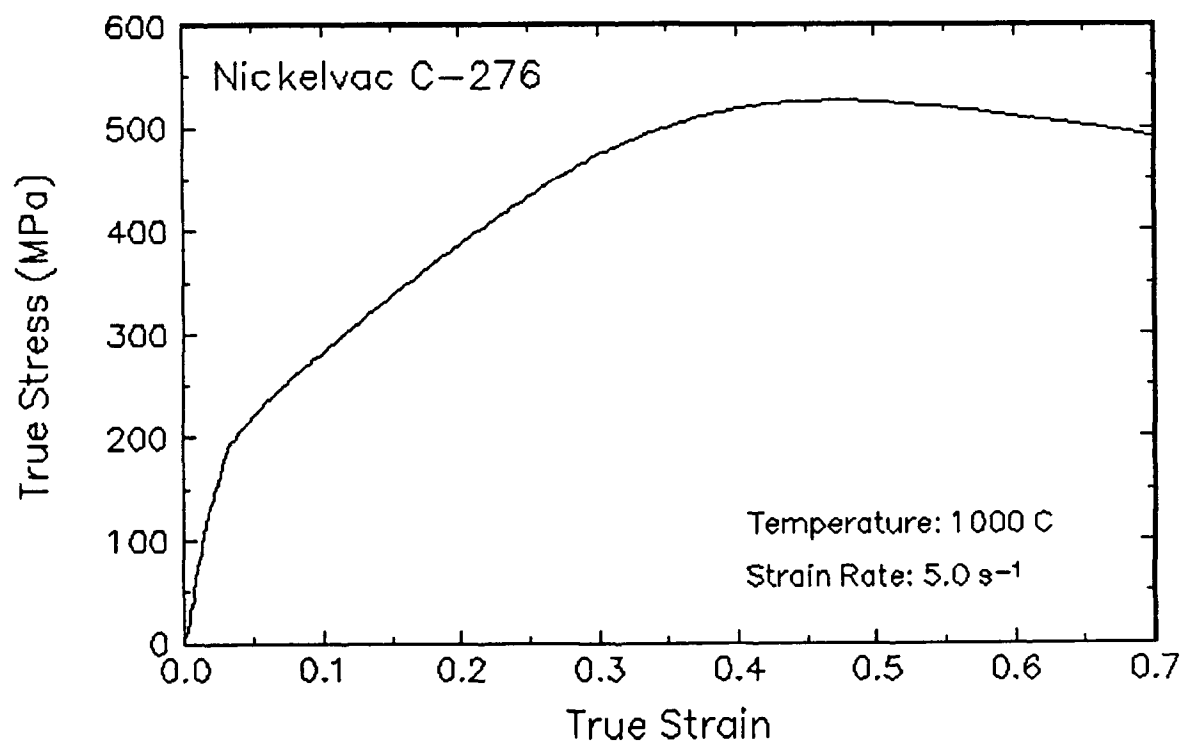


Figure 16. True stress-true strain curve, 1000 C and 5 s<sup>-1</sup>.

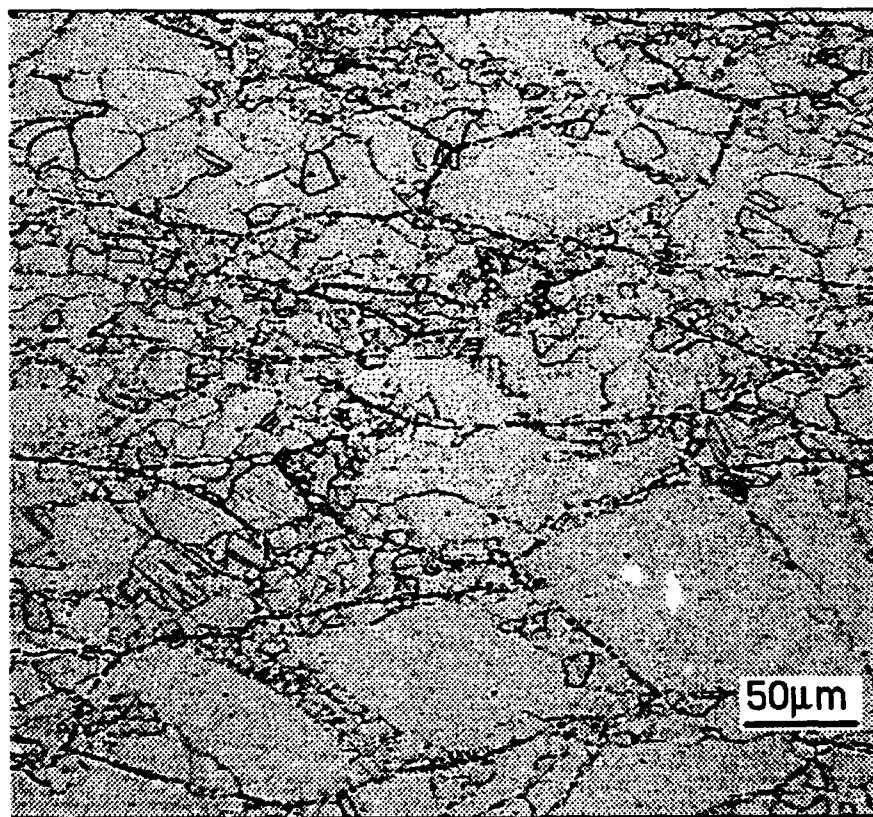
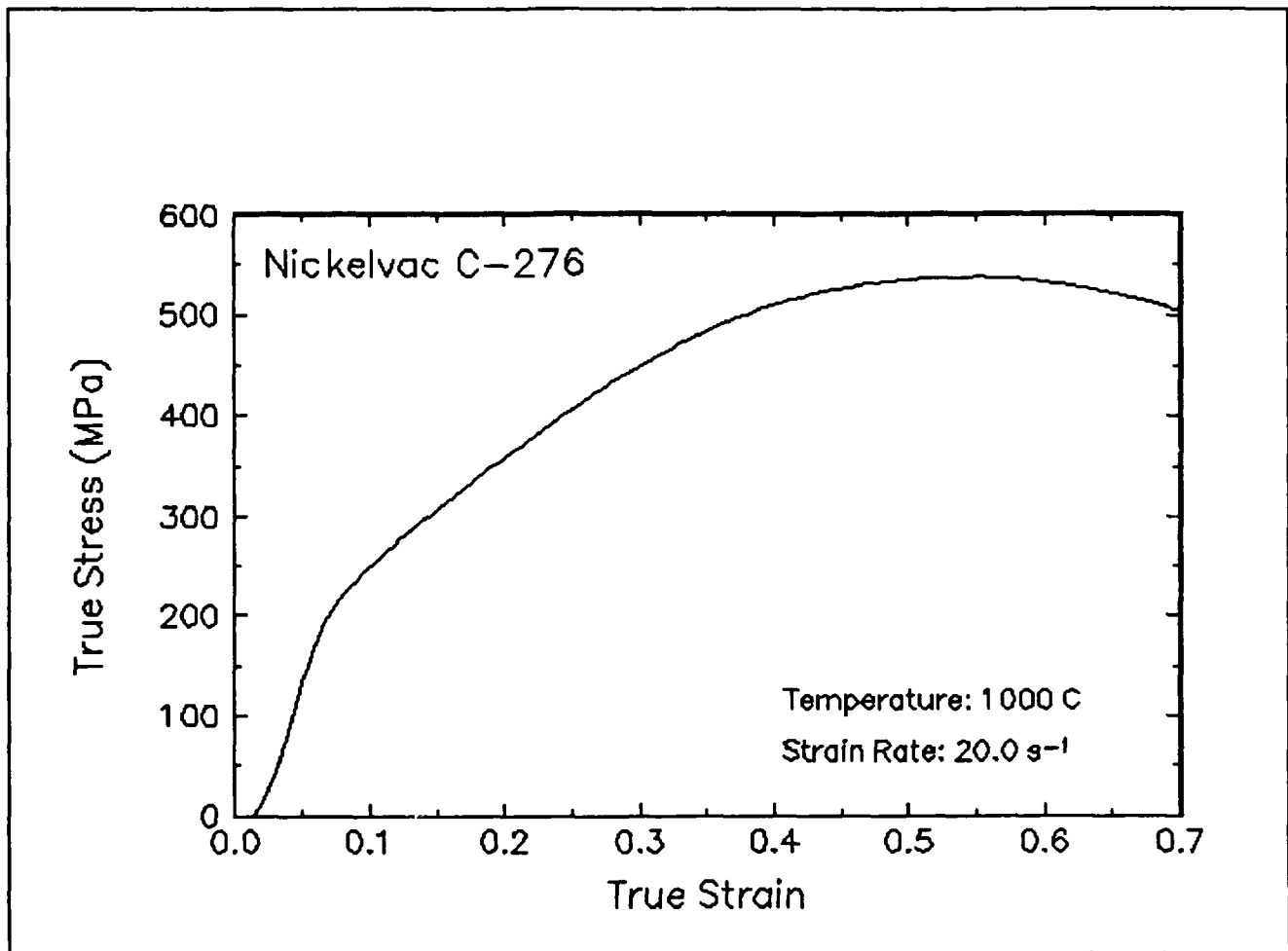
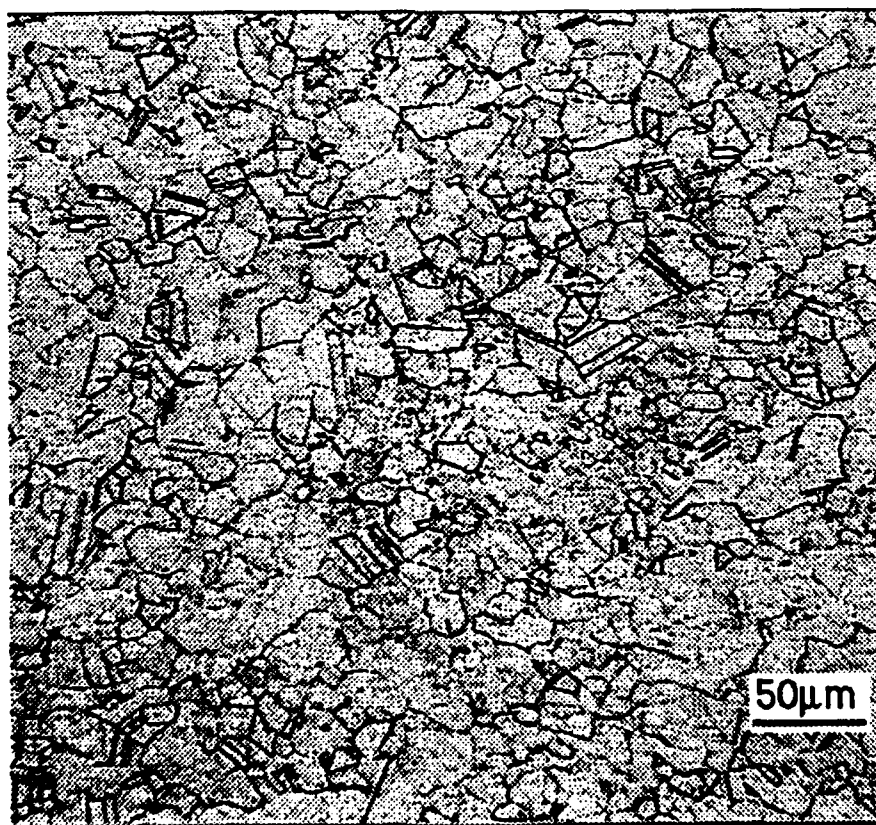
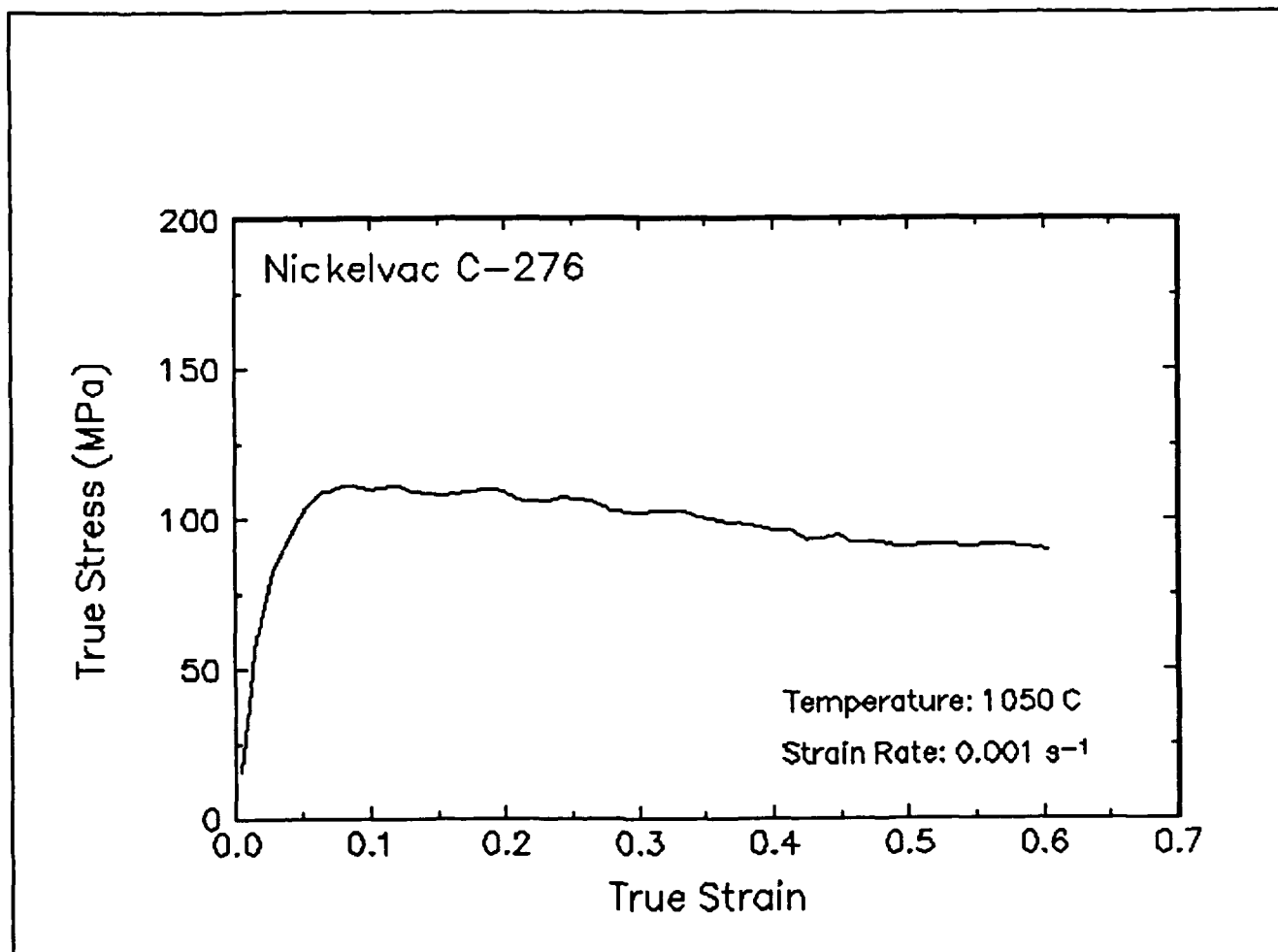


Figure 17. True stress-true strain curve and an optical micrograph from the center of the compressed sample cut through the compression axis, 1000 C and 20 s<sup>-1</sup>.



**Figure 18.** True stress-true strain curve and an optical micrograph from the center of the compressed sample cut through the compression axis, 1050 C and 0.001 s<sup>-1</sup>.

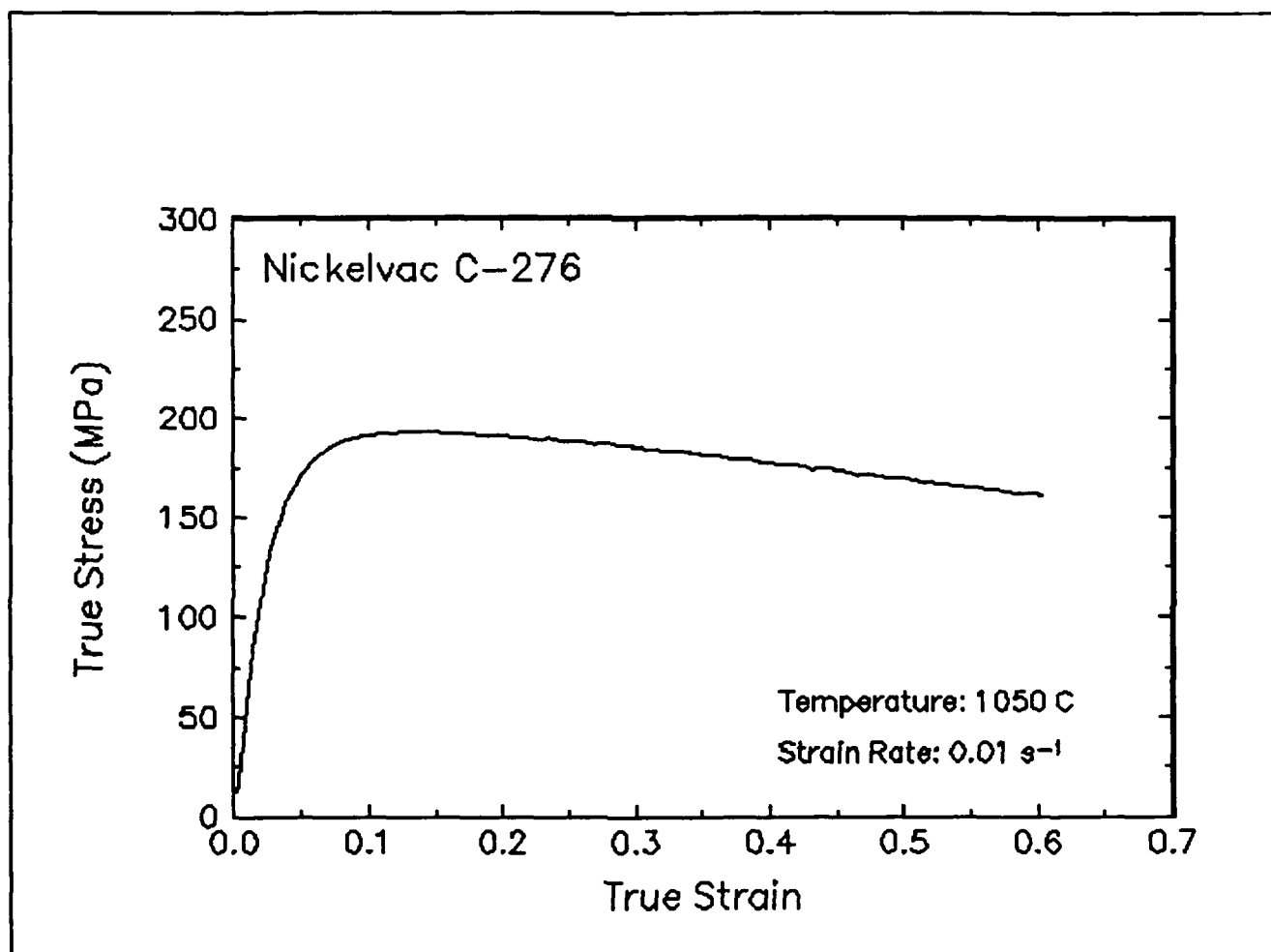


Figure 19. True stress-true strain curve, 1050 C and 0.01 s<sup>-1</sup>.

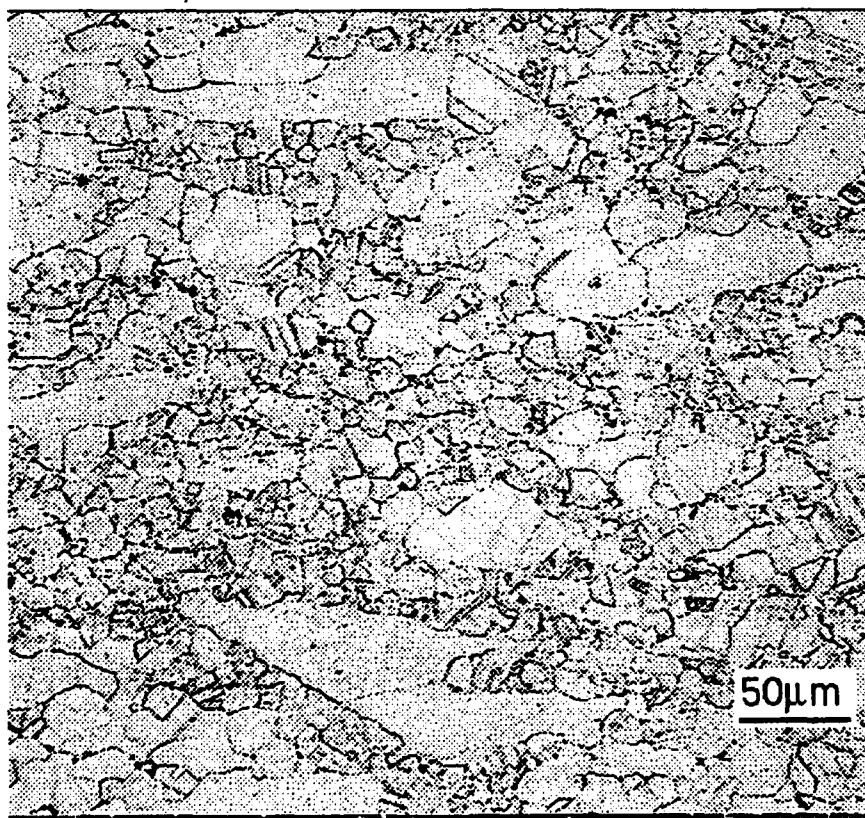
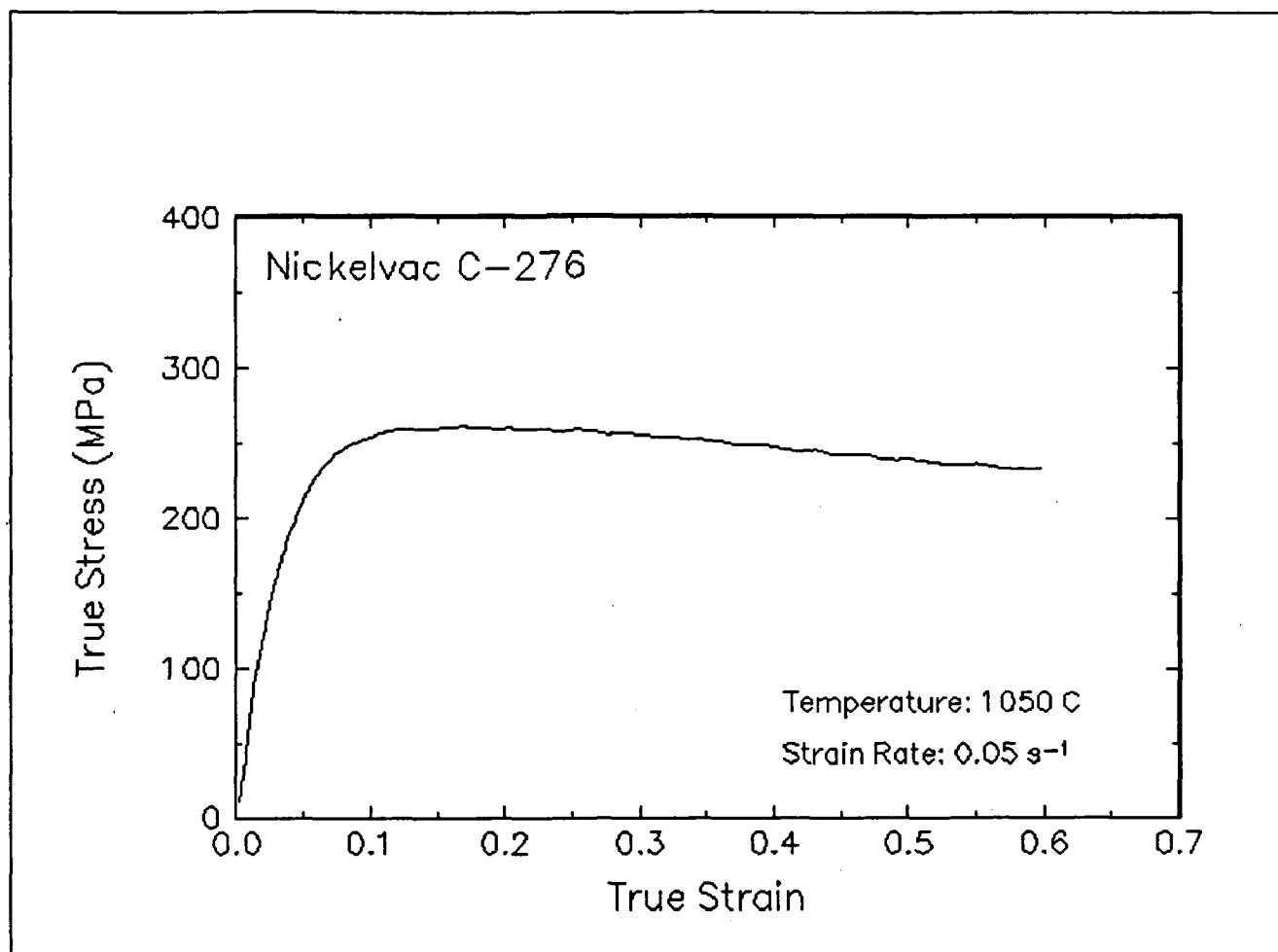


Figure 20. True stress-true strain curve and an optical micrograph from the center of the compressed sample cut through the compression axis, 1050 C and 0.05 s<sup>-1</sup>.

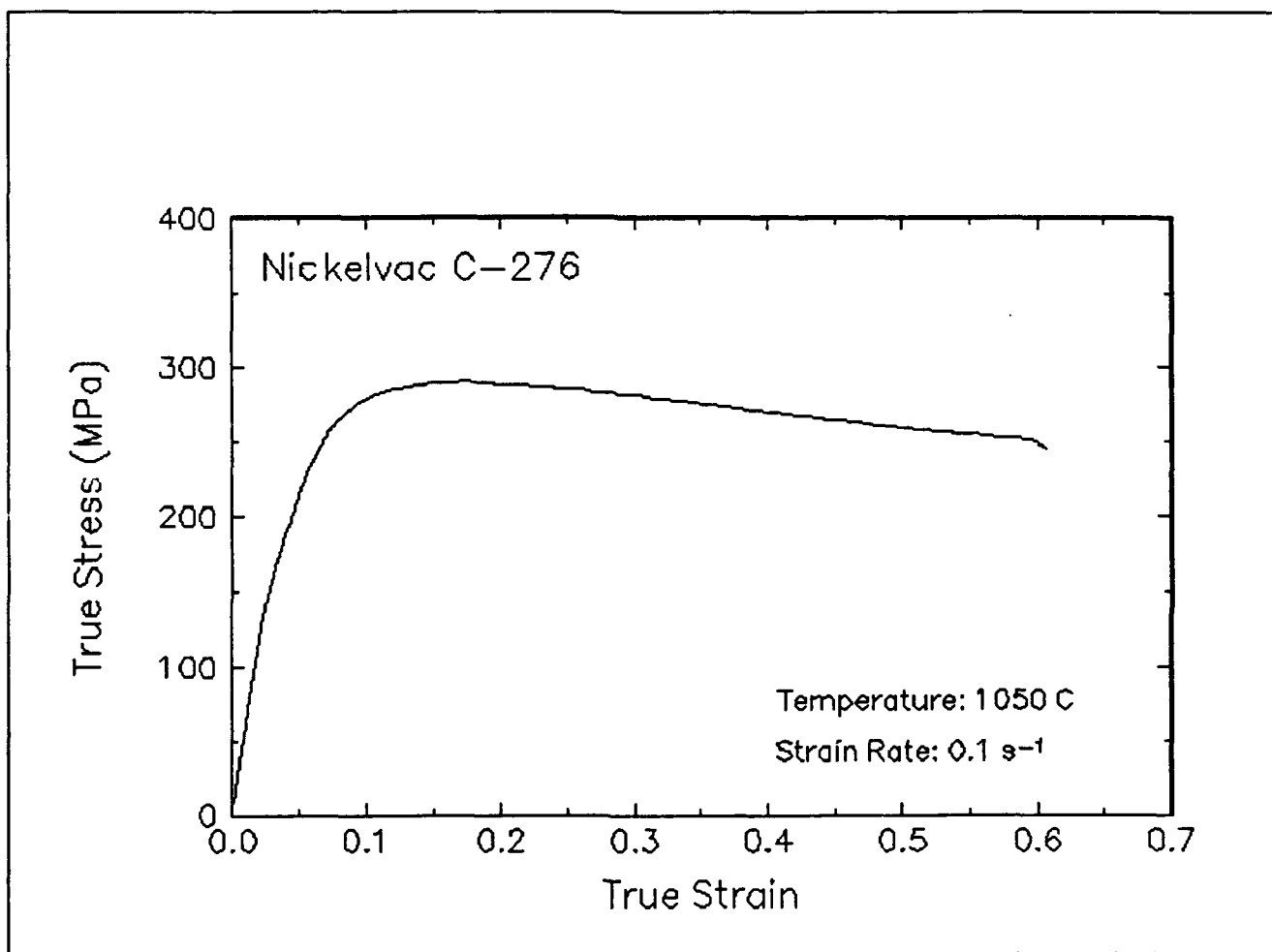


Figure 21. True stress-true strain curve, 1050 C and 0.1 s<sup>-1</sup>.

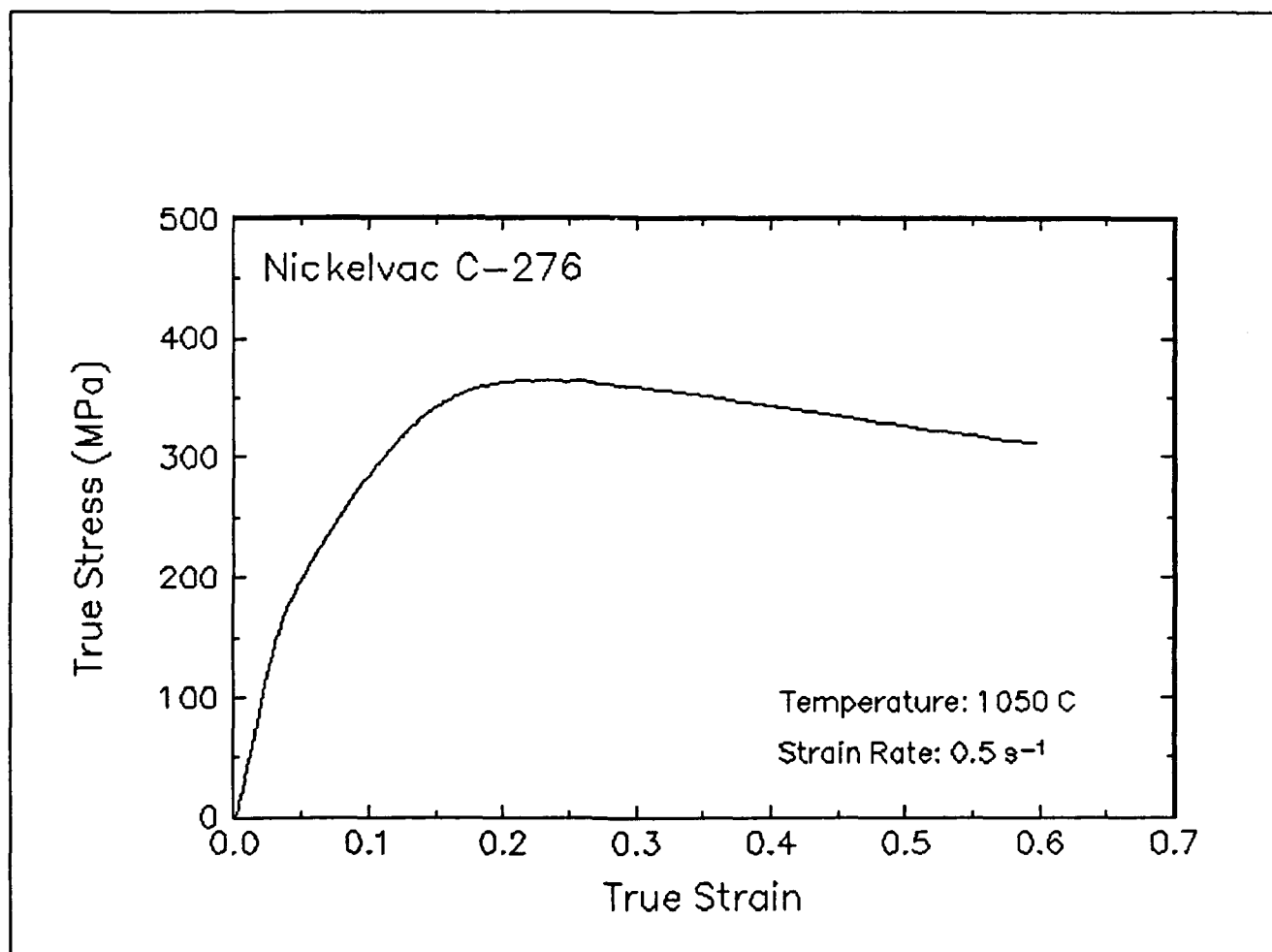


Figure 22. True stress-true strain curve, 1050 C and 0.5 s<sup>-1</sup>.

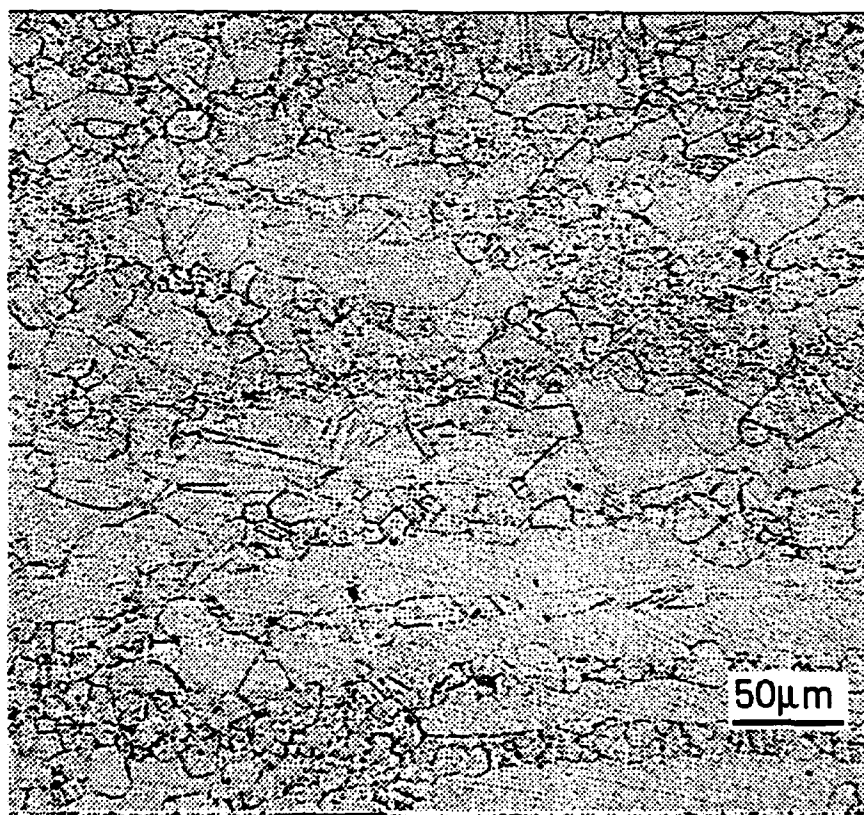
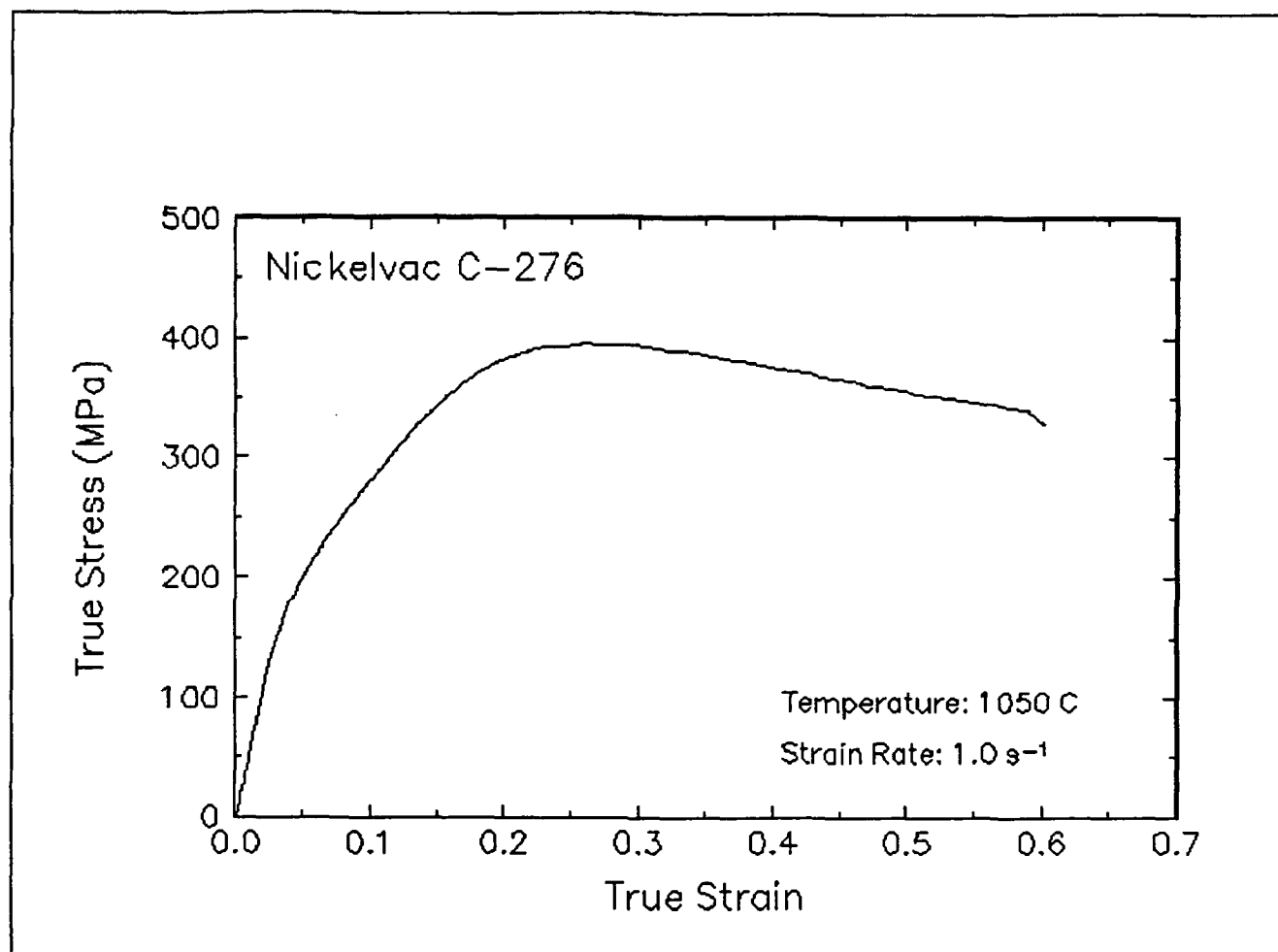


Figure 23. True stress-true strain curve and an optical micrograph from the center of the compressed sample cut through the compression axis, 1050 C and 1 s<sup>-1</sup>



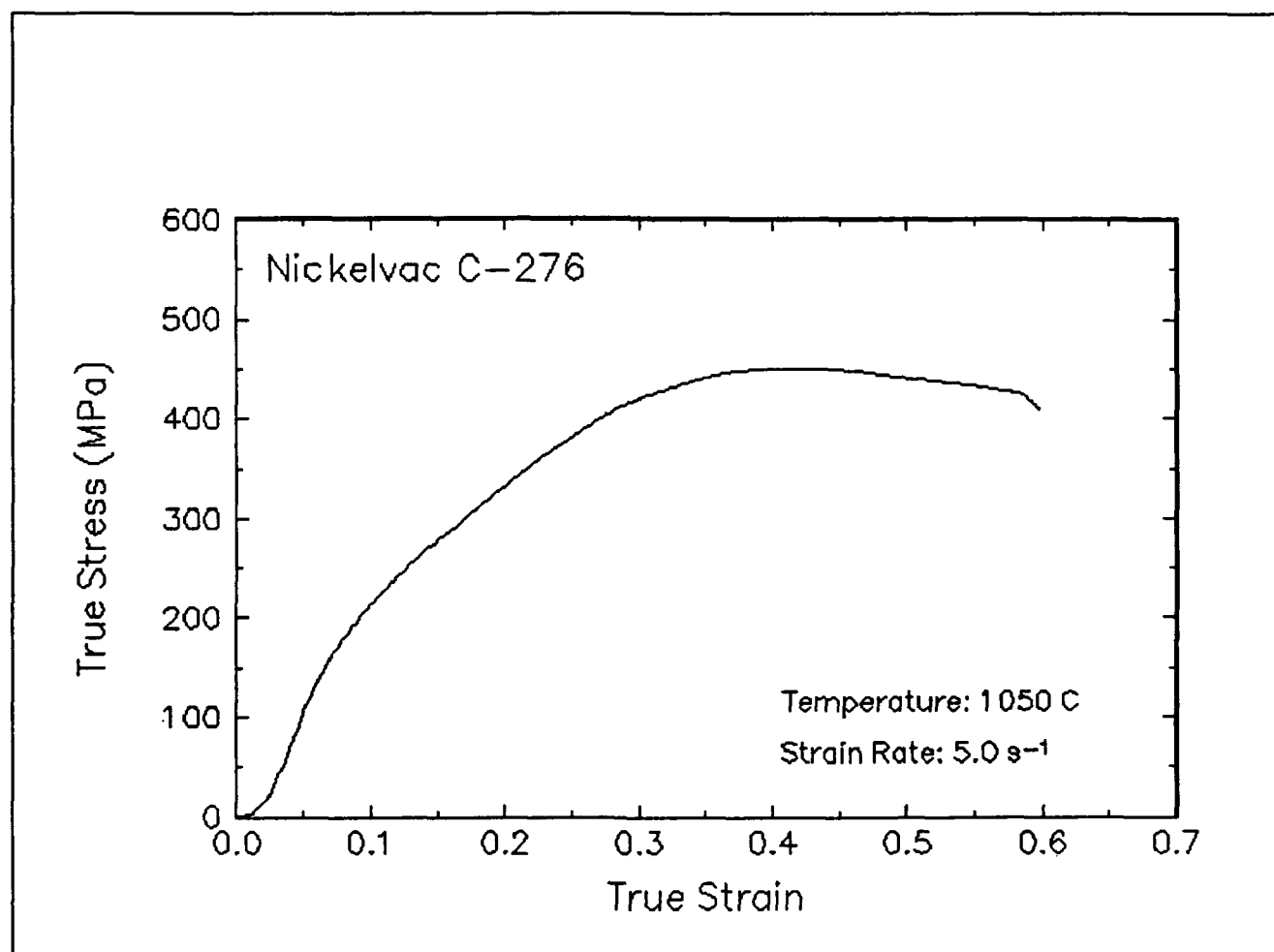


Figure 24. True stress-true strain curve, 1050 C and 5 s<sup>-1</sup>.

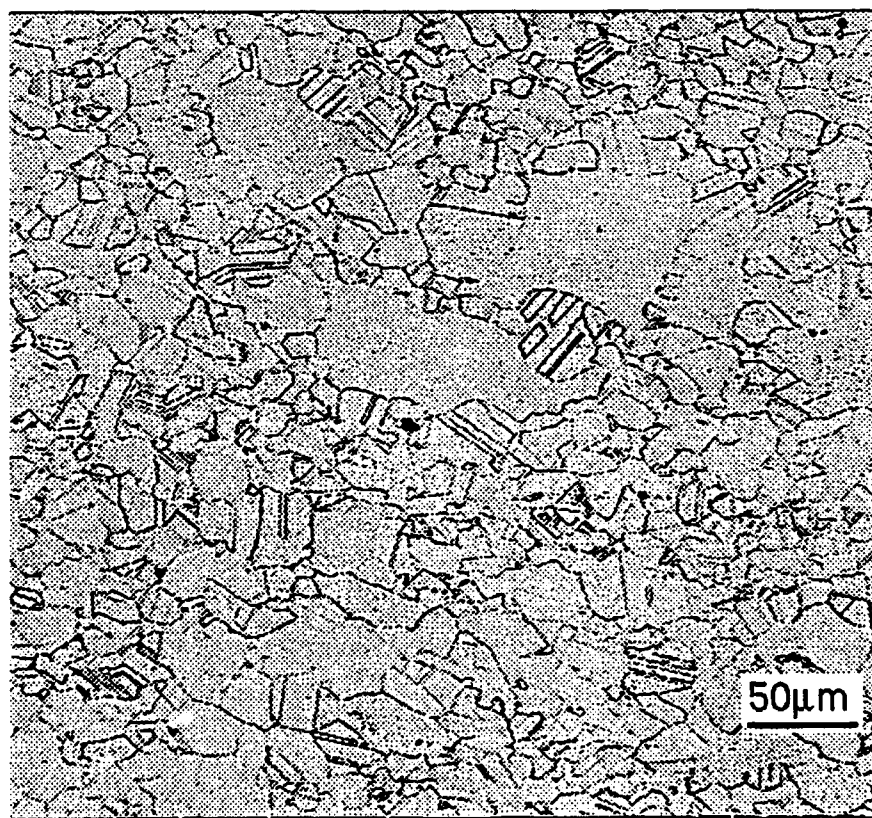
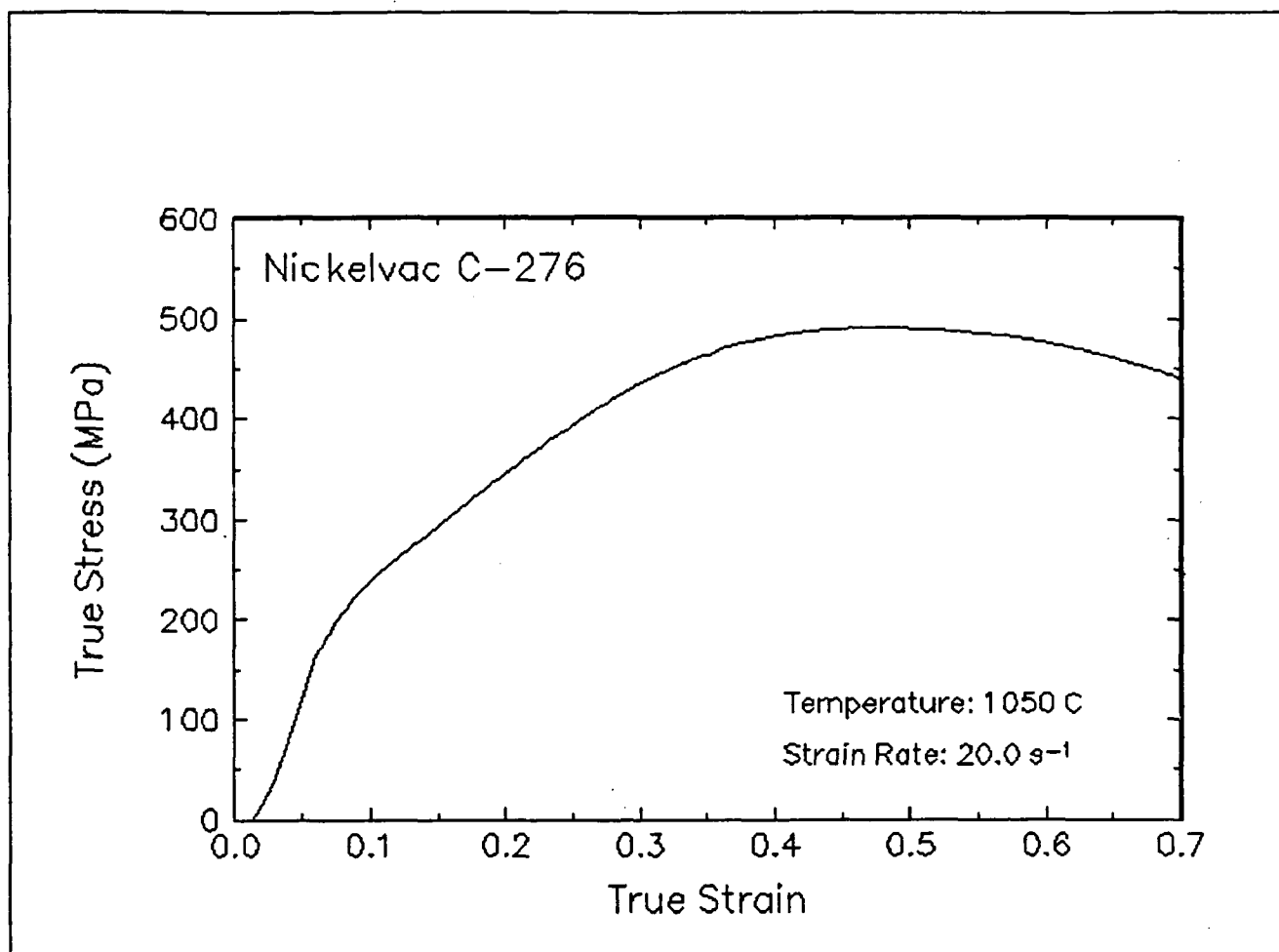


Figure 25. True stress-true strain curve and an optical micrograph from the center of the compressed sample cut through the compression axis, 1050 C and 20 s<sup>-1</sup>.

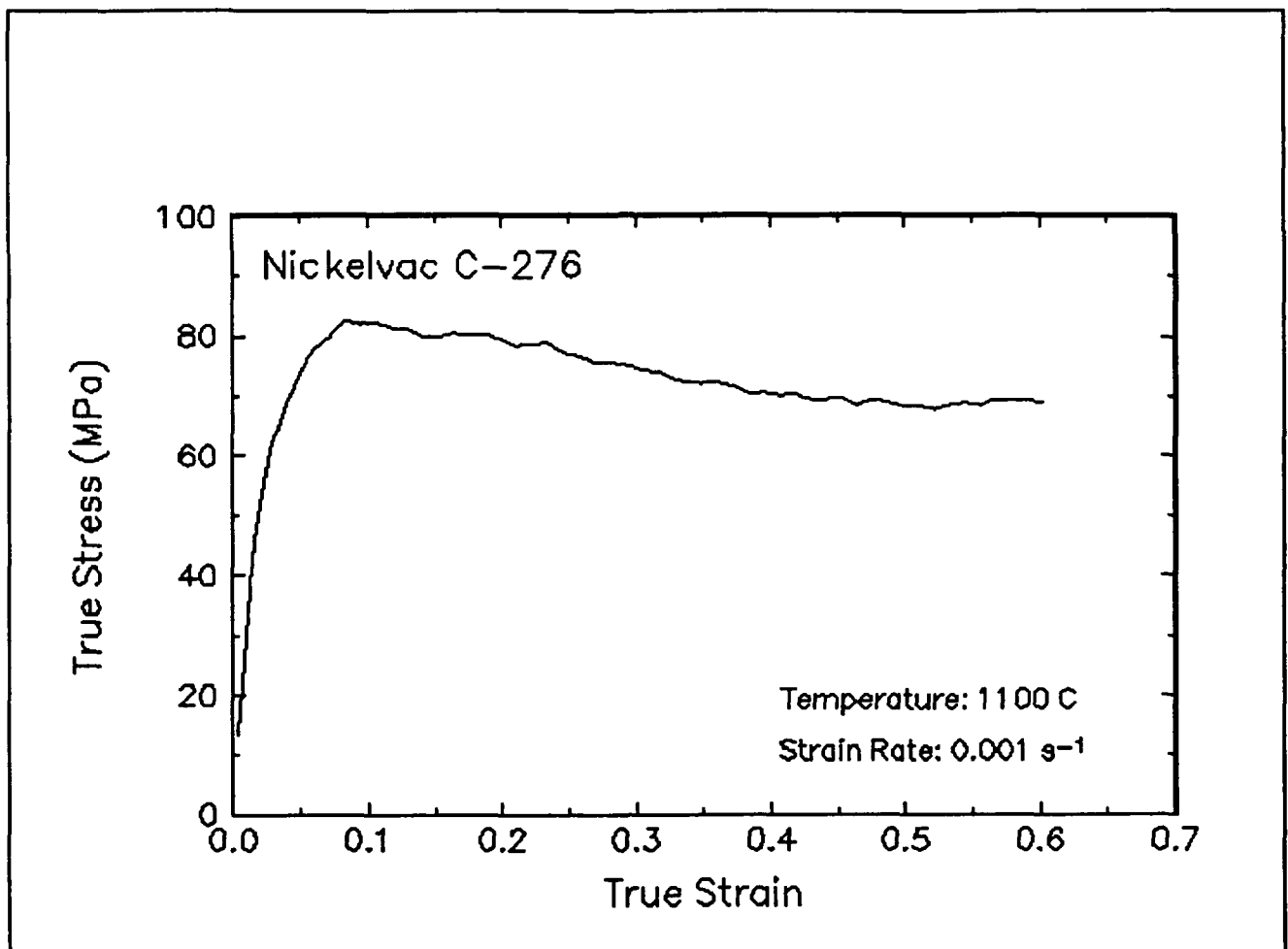


Figure 26. True stress-true strain curve and an optical micrograph from the center of the compressed sample cut through the compression axis, 1100 C and 0.001 s<sup>-1</sup>.

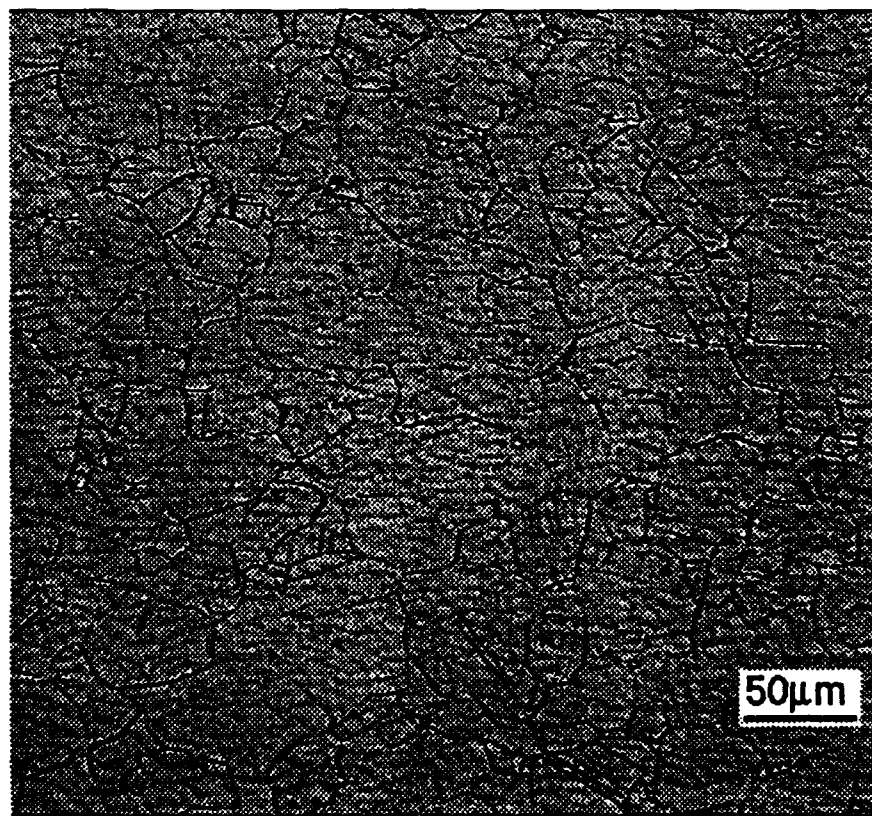
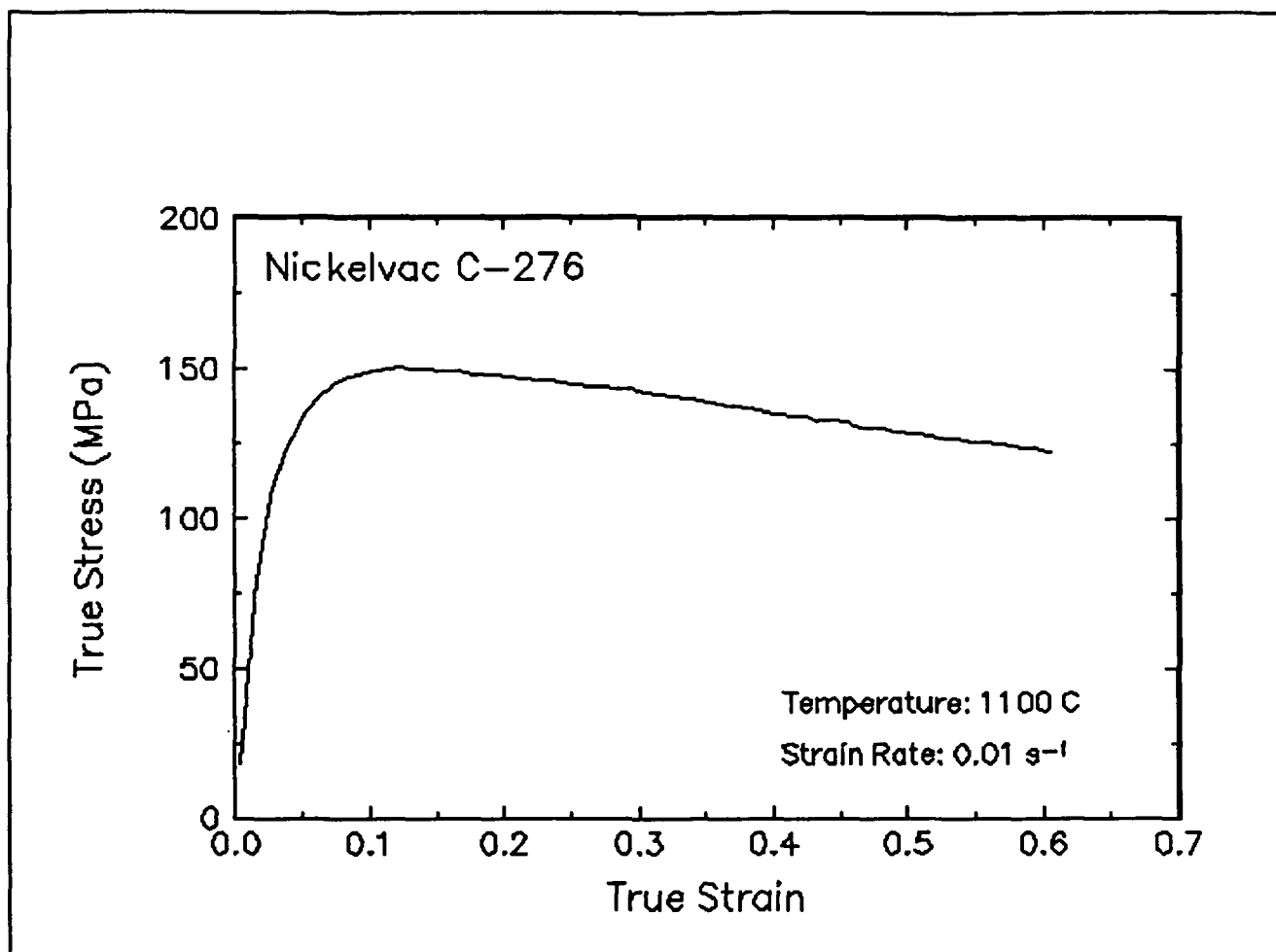


Figure 27. True stress-true strain curve and an optical micrograph from the center of the compressed sample cut through the compression axis, 1100 C and 0.01 s<sup>-1</sup>.

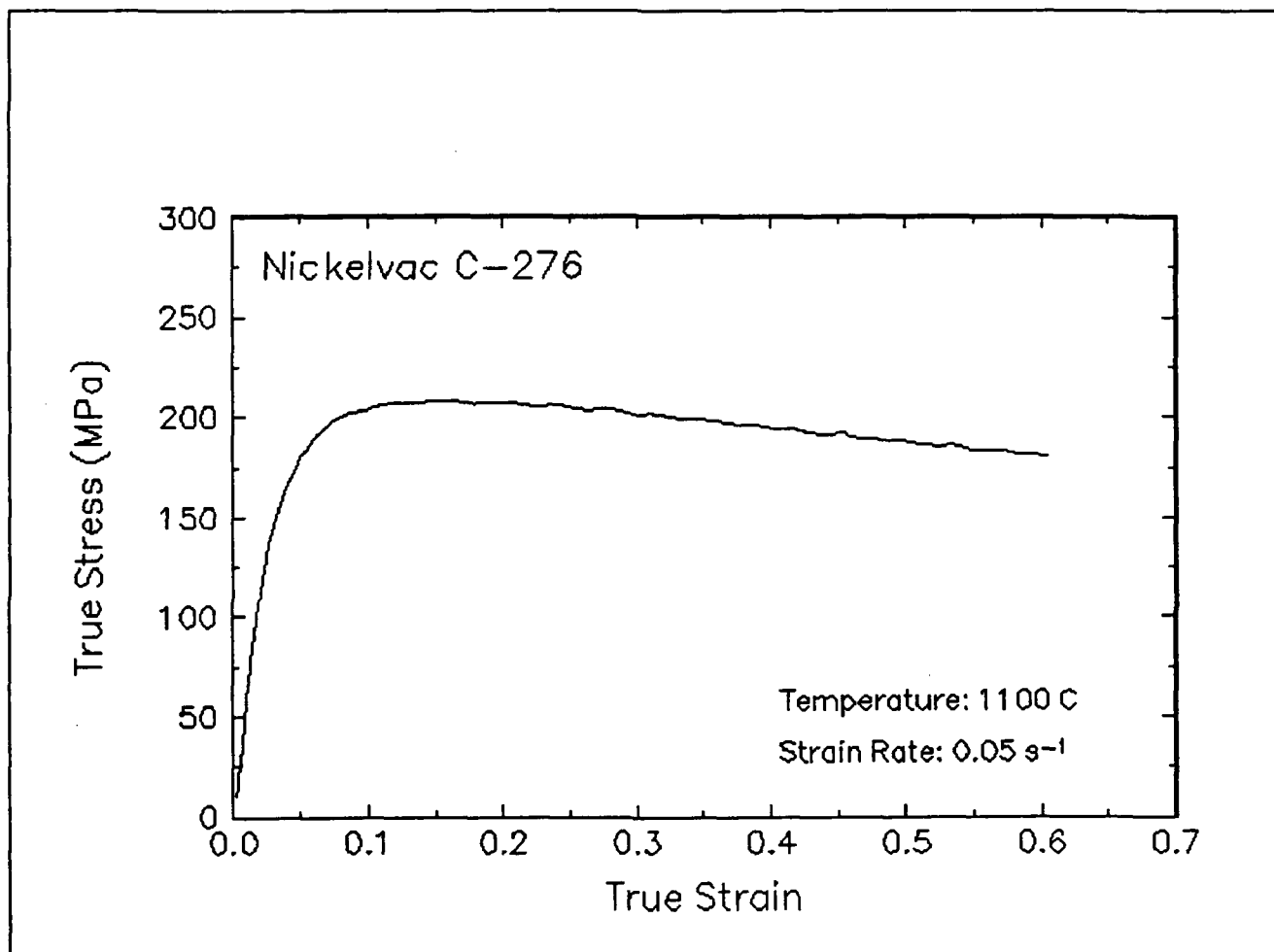


Figure 28. True stress-true strain curve, 1100 C and 0.05 s<sup>-1</sup>.

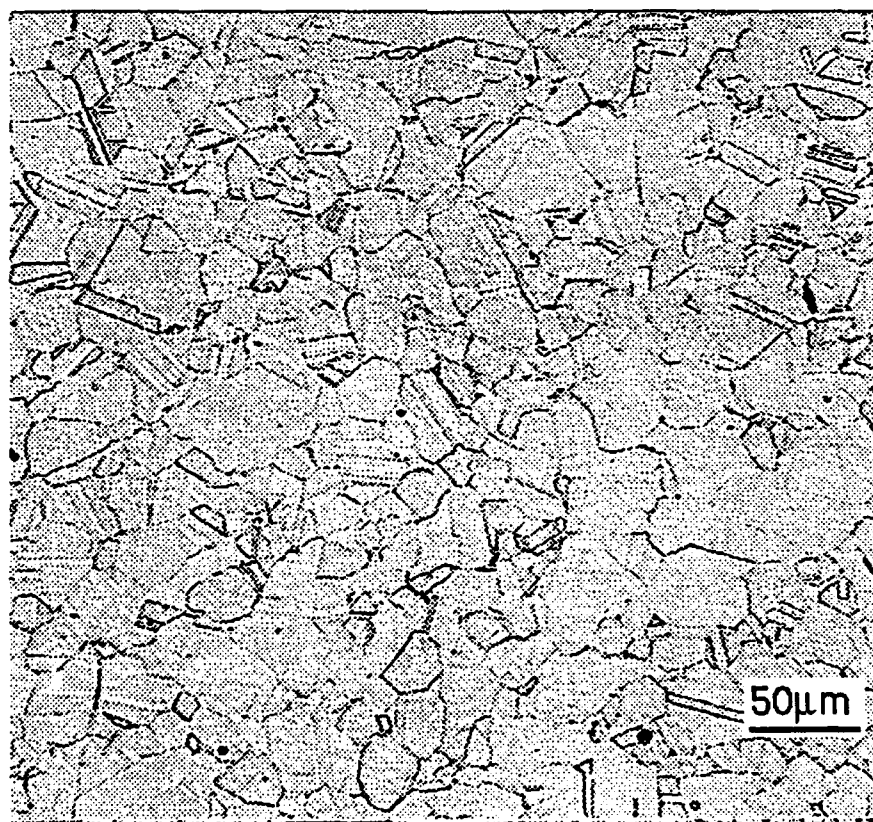
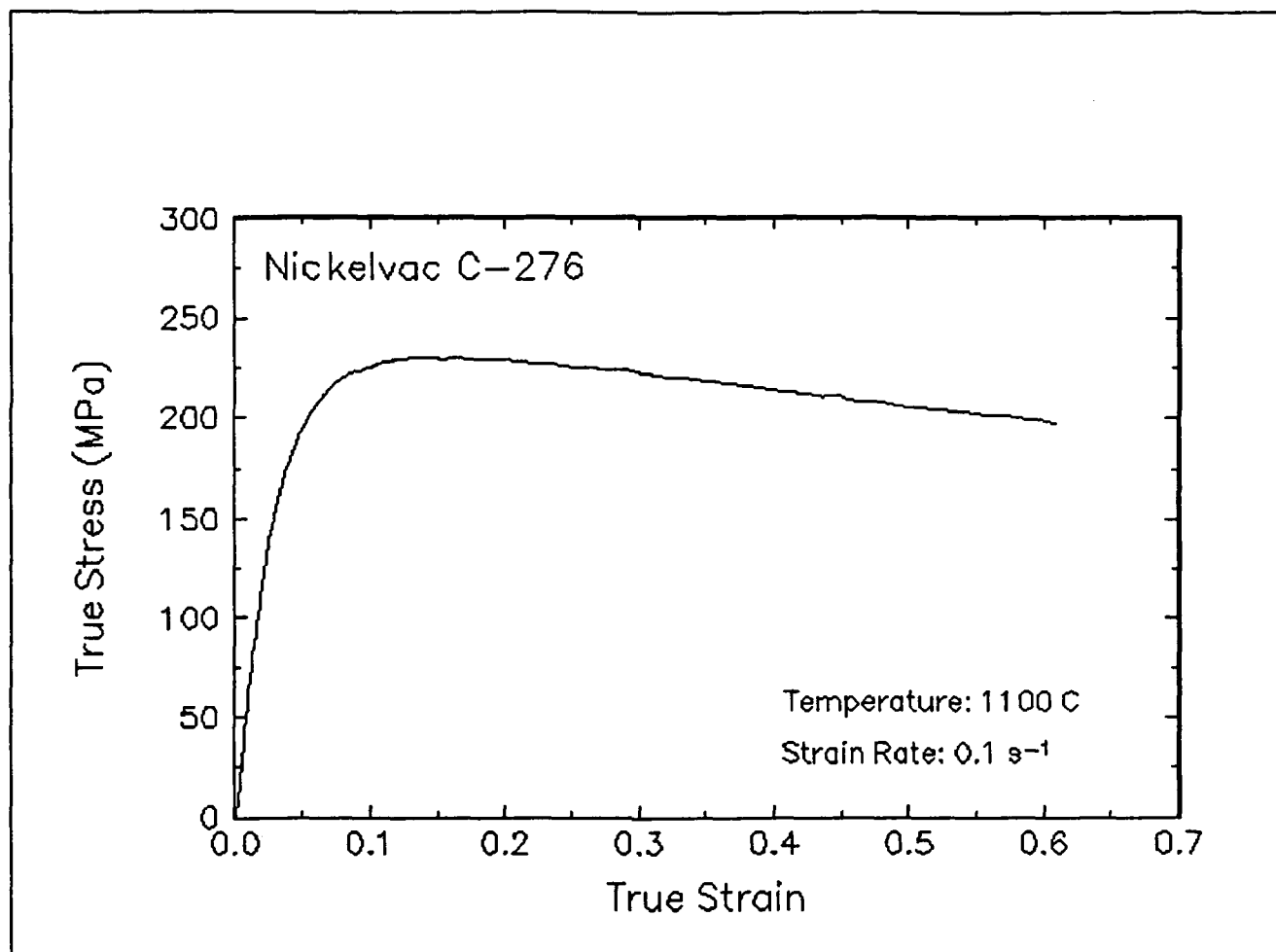


Figure 29. True stress-true strain curve and an optical micrograph from the center of the compressed sample cut through the compression axis, 1100 C and 0.1 s<sup>-1</sup>.

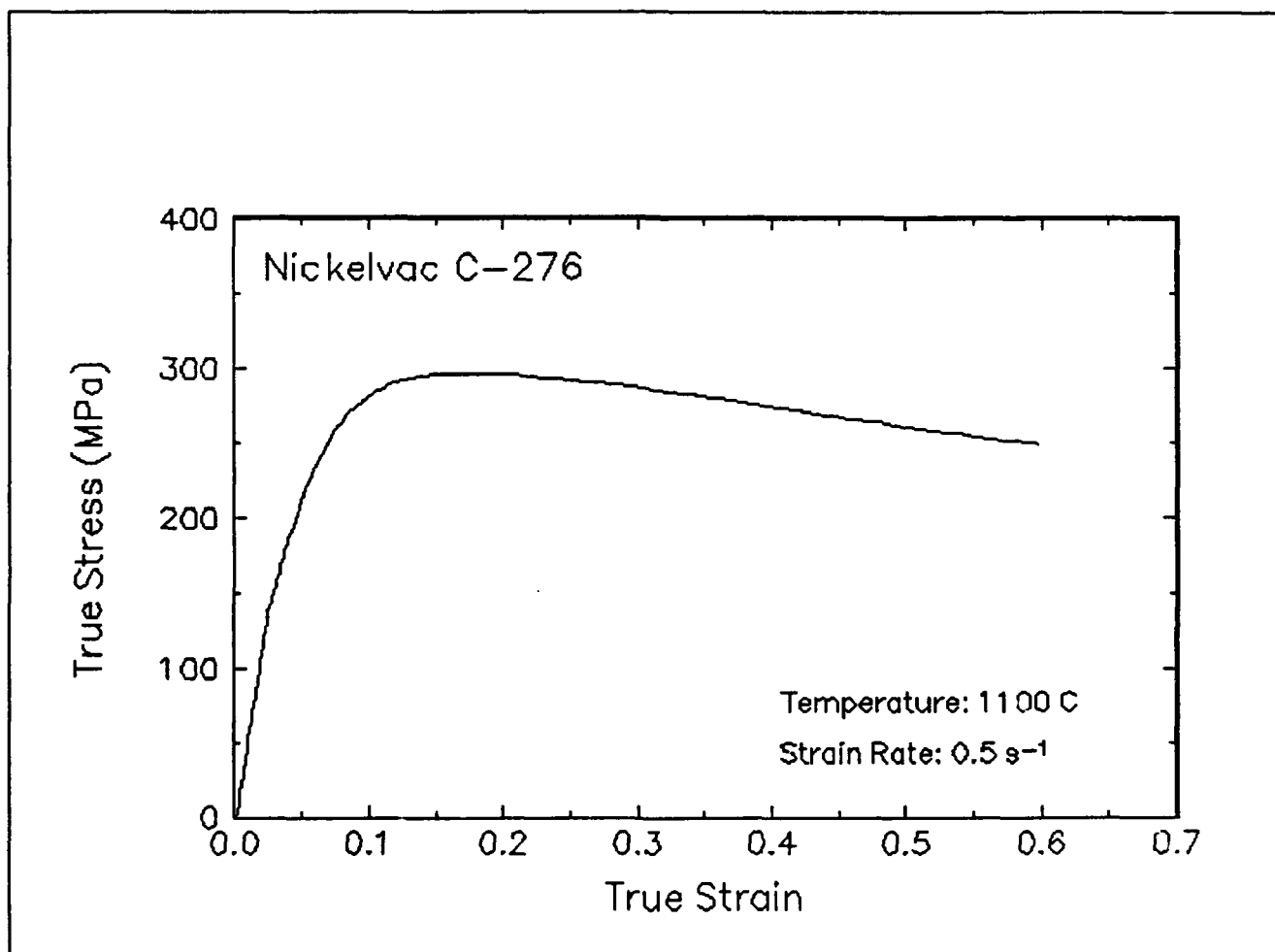


Figure 30. True stress-true strain curve, 1100 C and 0.5 s<sup>-1</sup>.

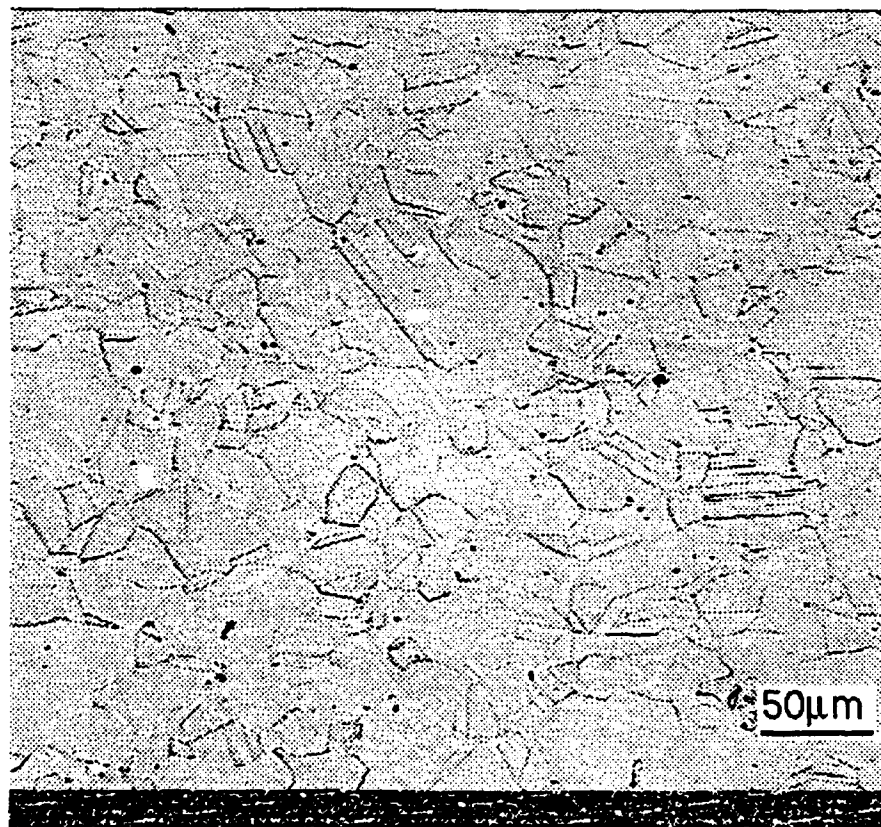
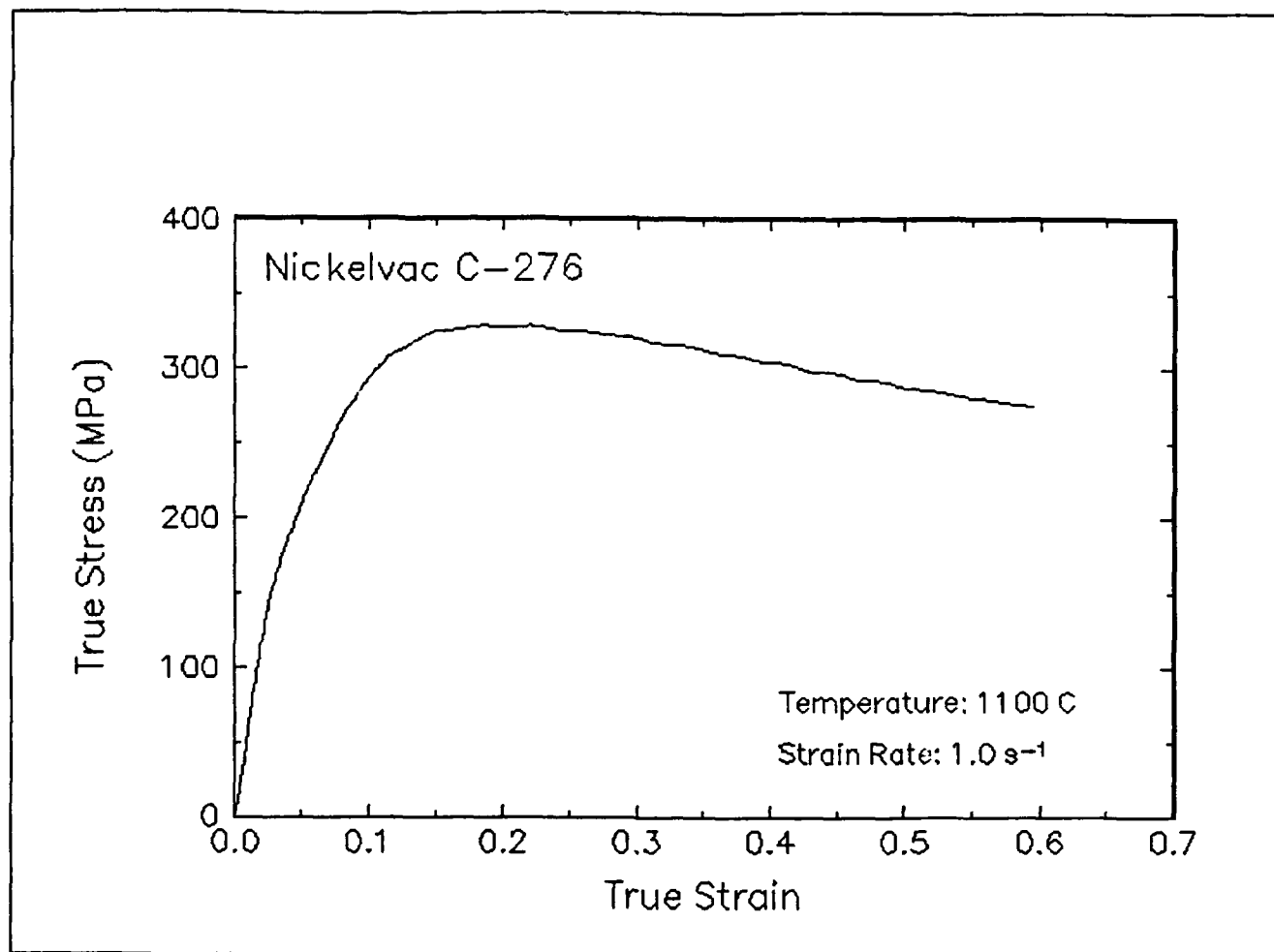


Figure 31. True stress-true strain curve and an optical micrograph from the center of the compressed sample cut through the compression axis, 1100 C and 1 s<sup>-1</sup>.



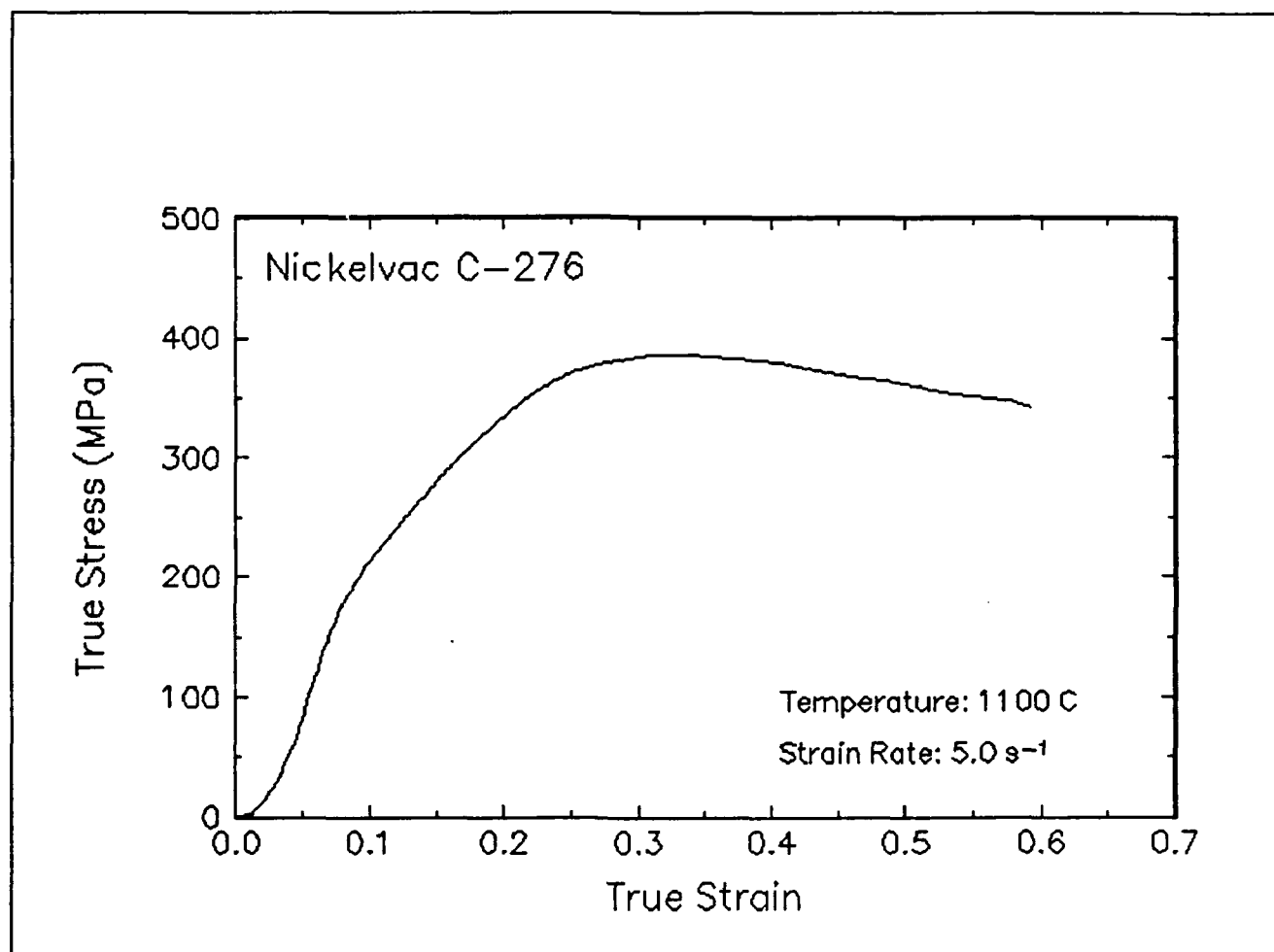


Figure 32. True stress-true strain curve, 1100 C and 5 s<sup>-1</sup>.

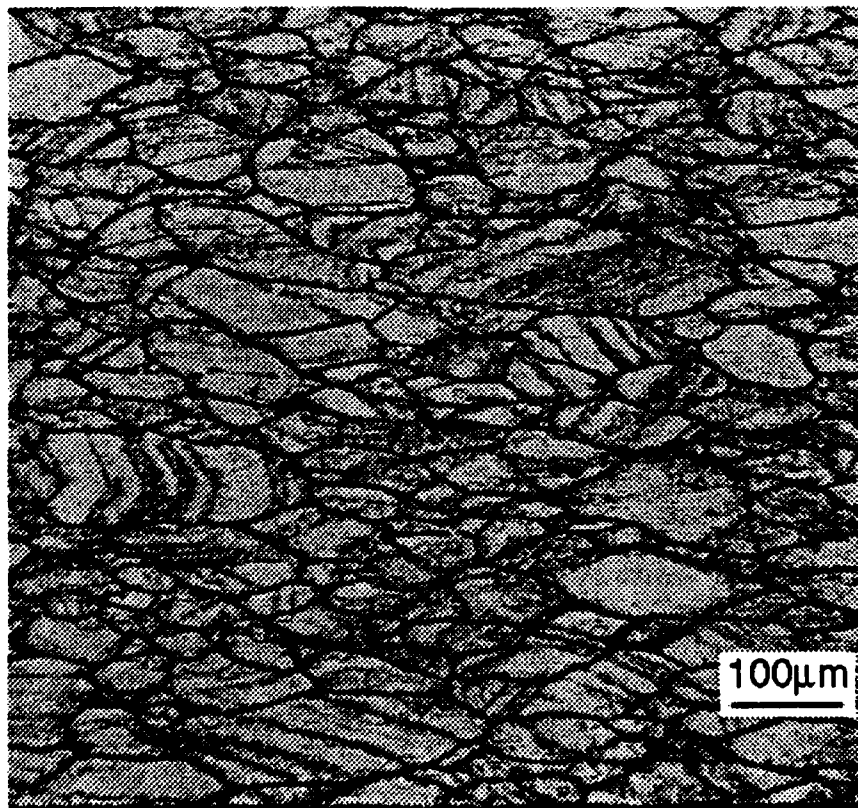
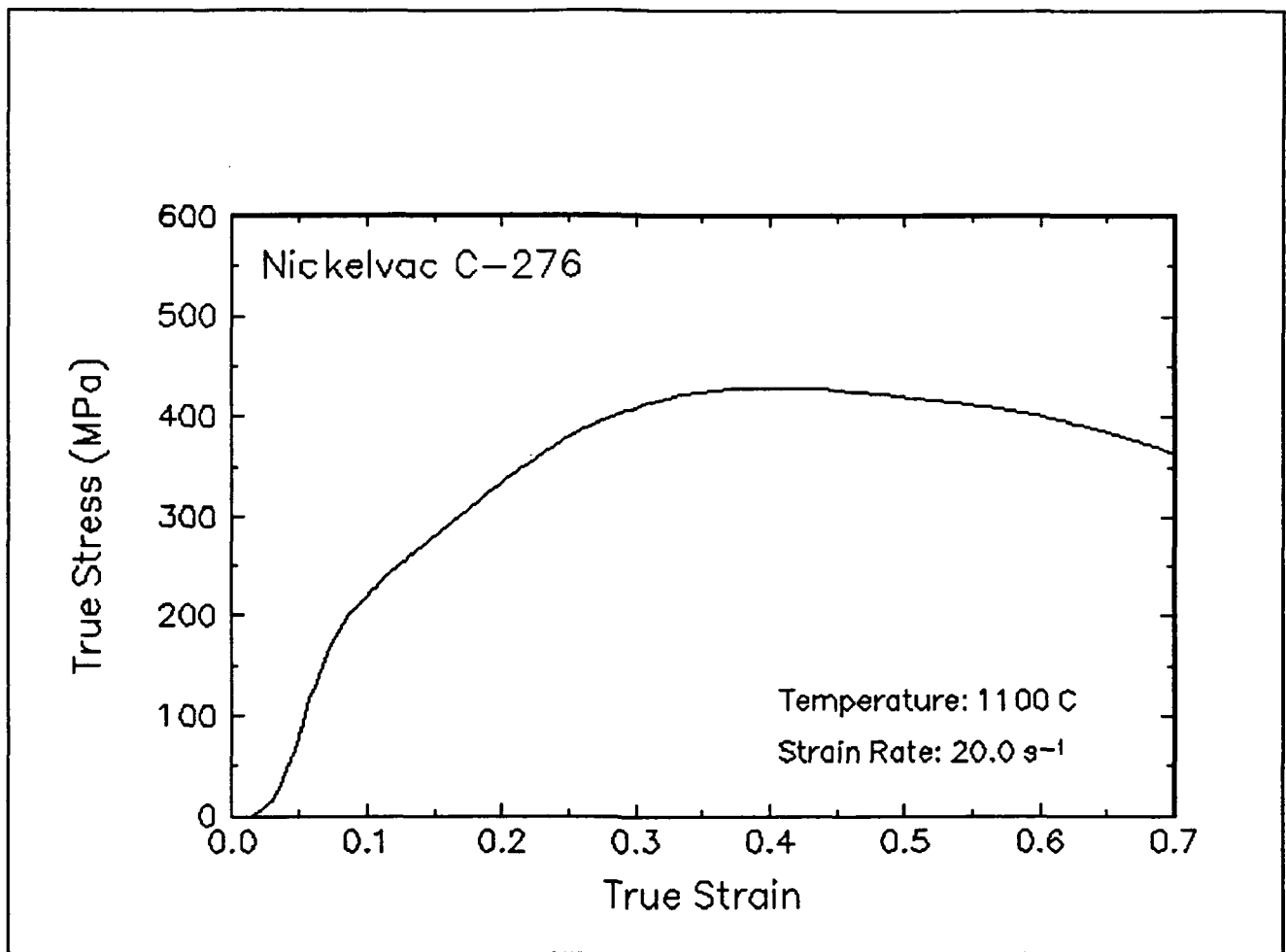


Figure 33. True stress-true strain curve and an optical micrograph from the center of the compressed sample cut through the compression axis, 1100 C and 20 s<sup>-1</sup>.

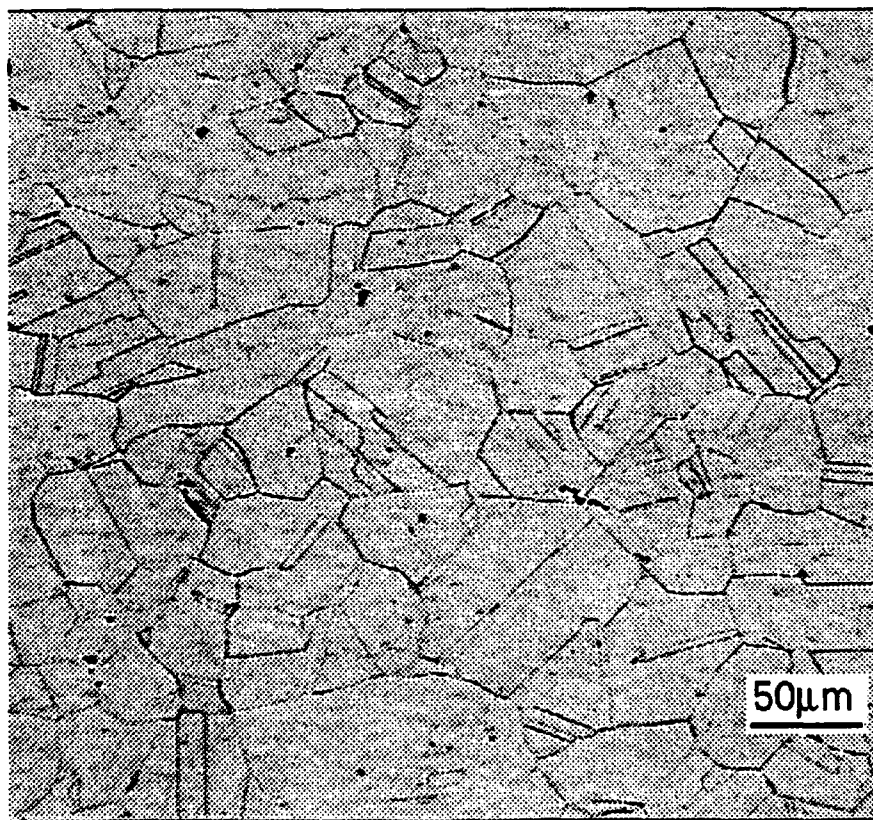
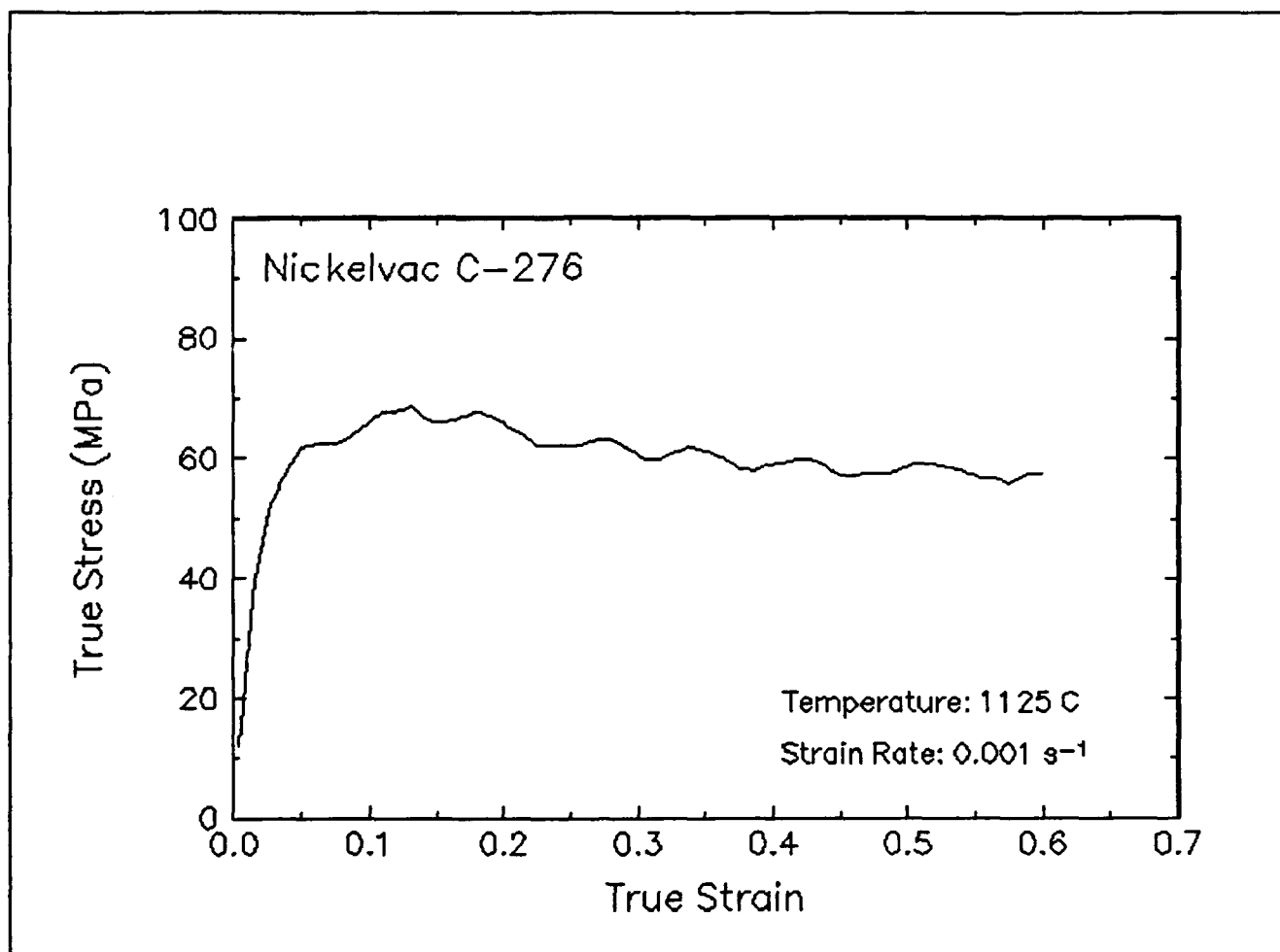


Figure 34. True stress-true strain curve and an optical micrograph from the center of the compressed sample cut through the compression axis, 1125 C and 0.001 s<sup>-1</sup>.

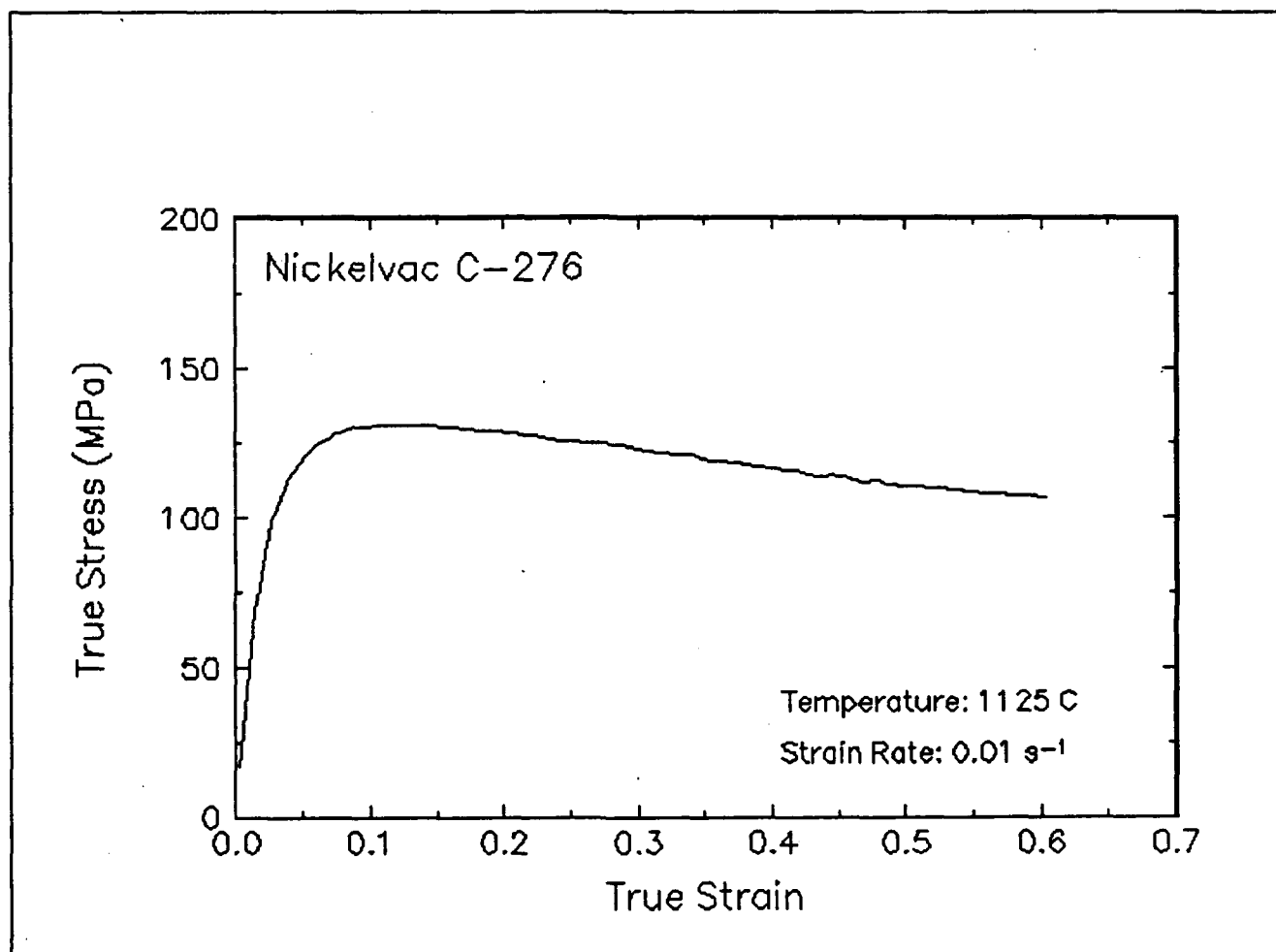


Figure 35. True stress-true strain curve, 1125 C and 0.01 s<sup>-1</sup>.

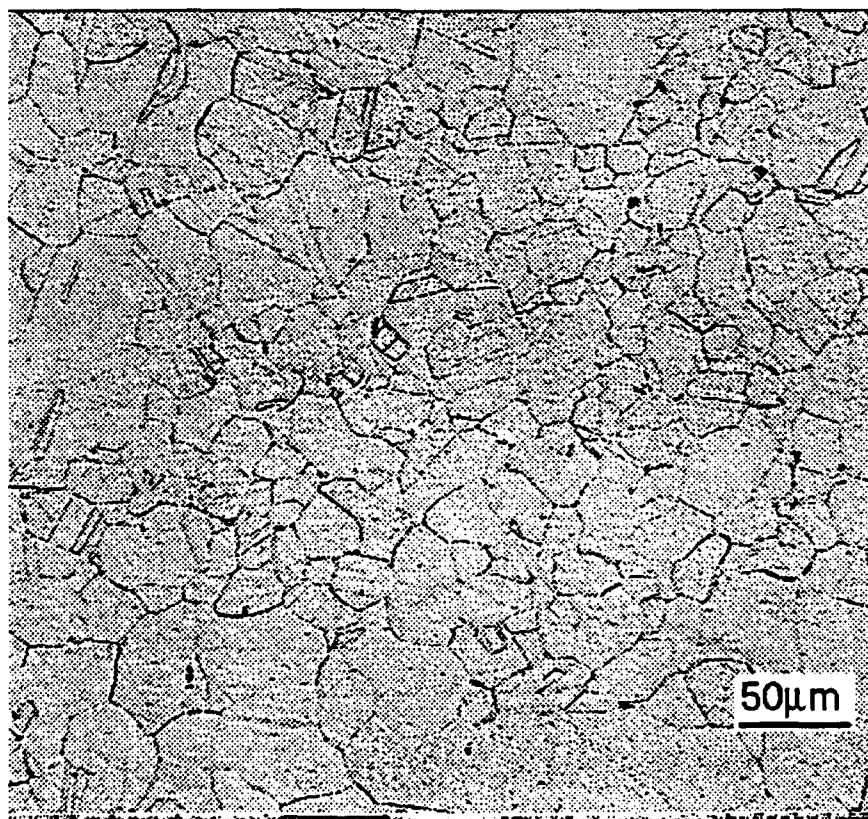
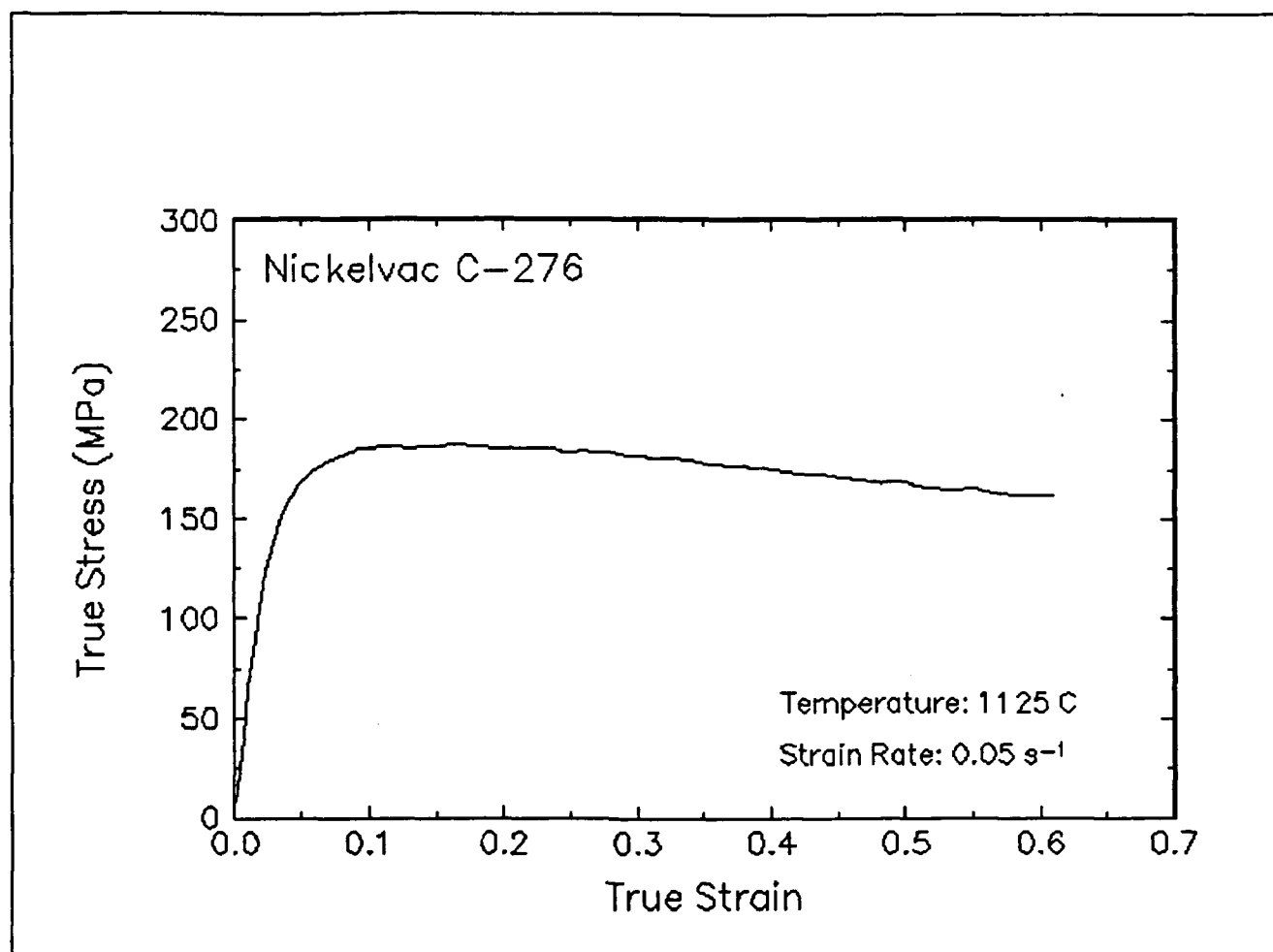


Figure 36. True stress-true strain curve and an optical micrograph from the center of the compressed sample cut through the compression axis, 1125 C and 0.05 s<sup>-1</sup>.

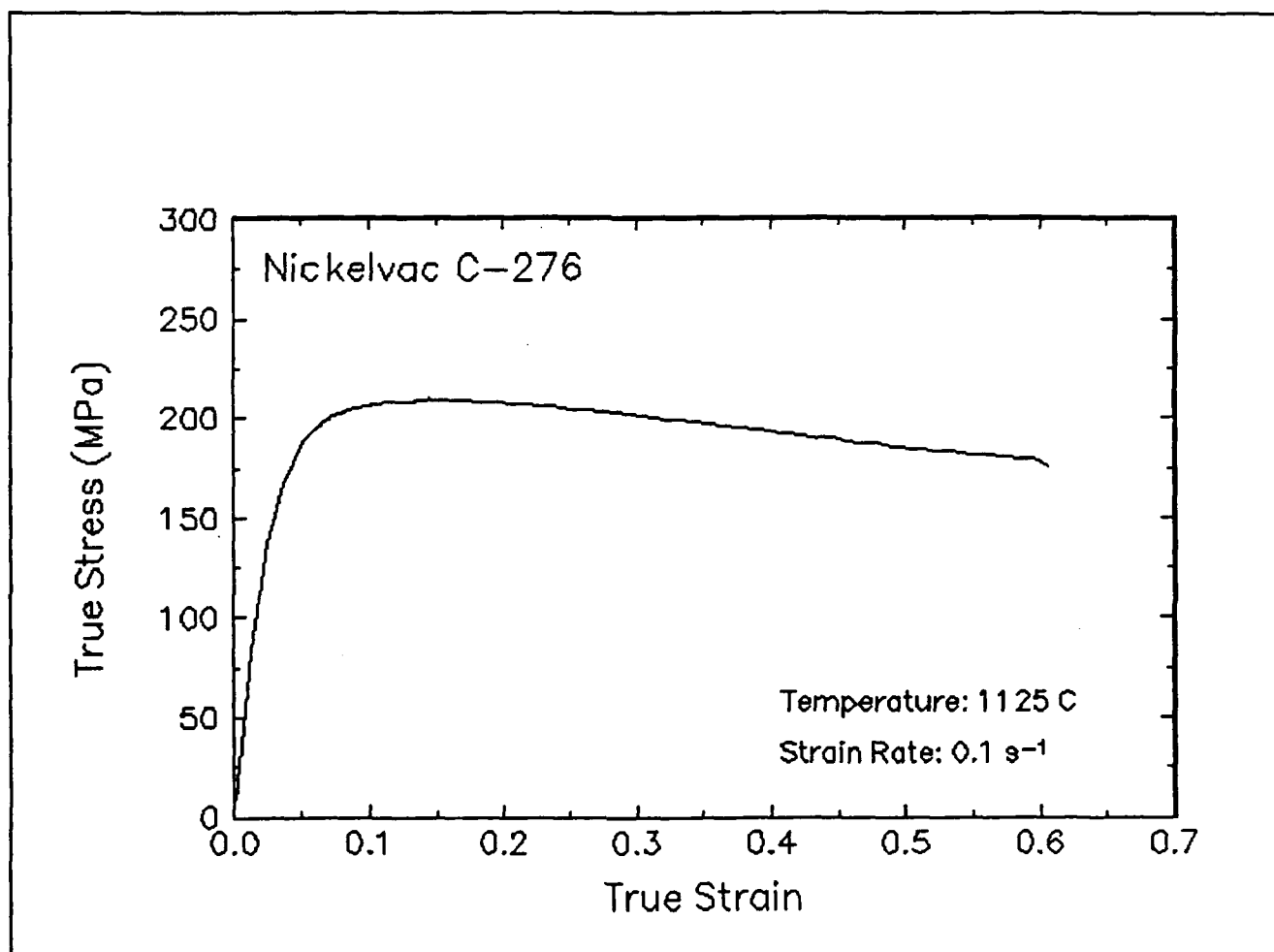


Figure 37. True stress-true strain curve, 1125 C and 0.1 s<sup>-1</sup>.

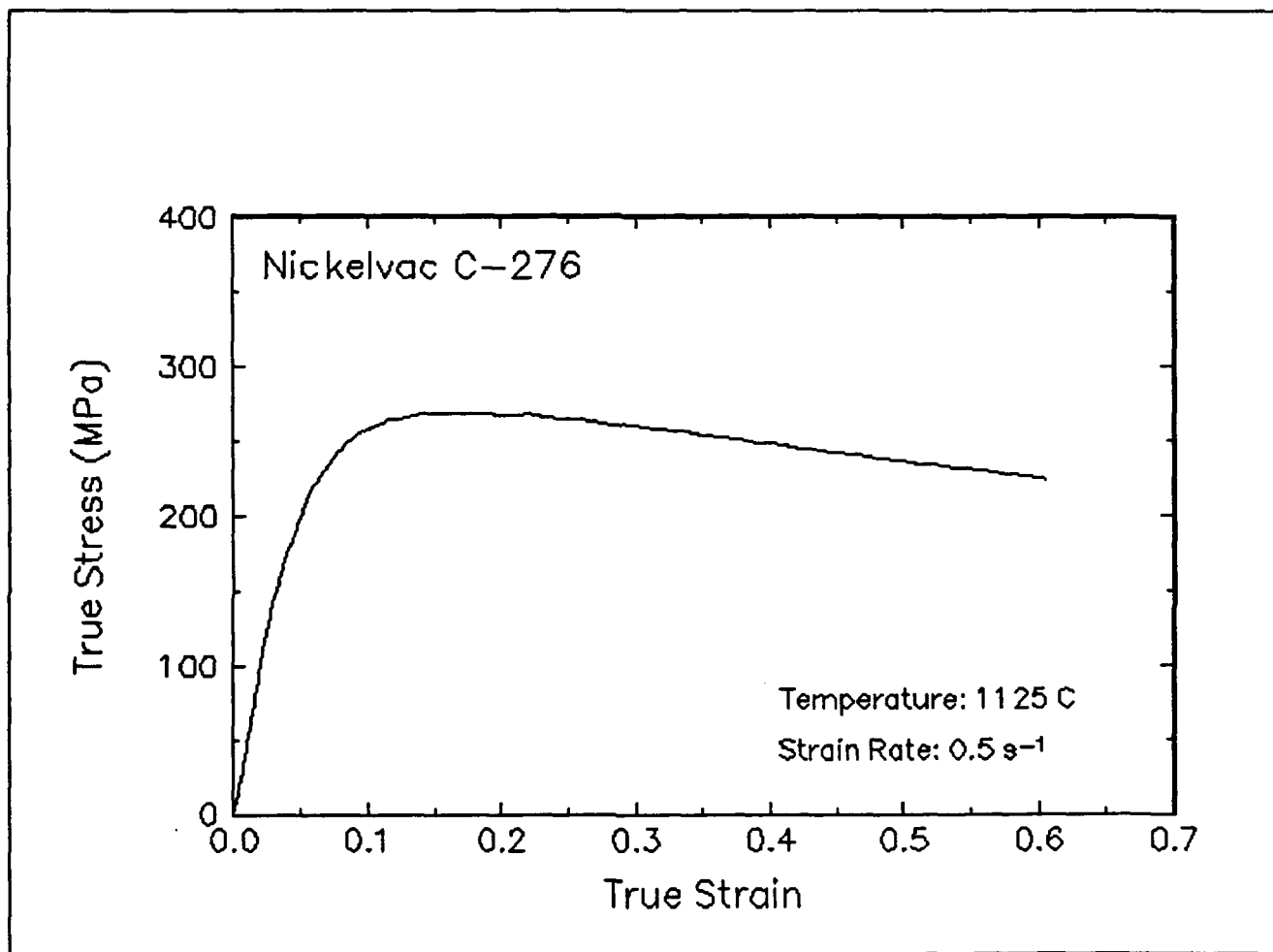


Figure 38. True stress-true strain curve, 1125 C and 0.5 s<sup>-1</sup>.

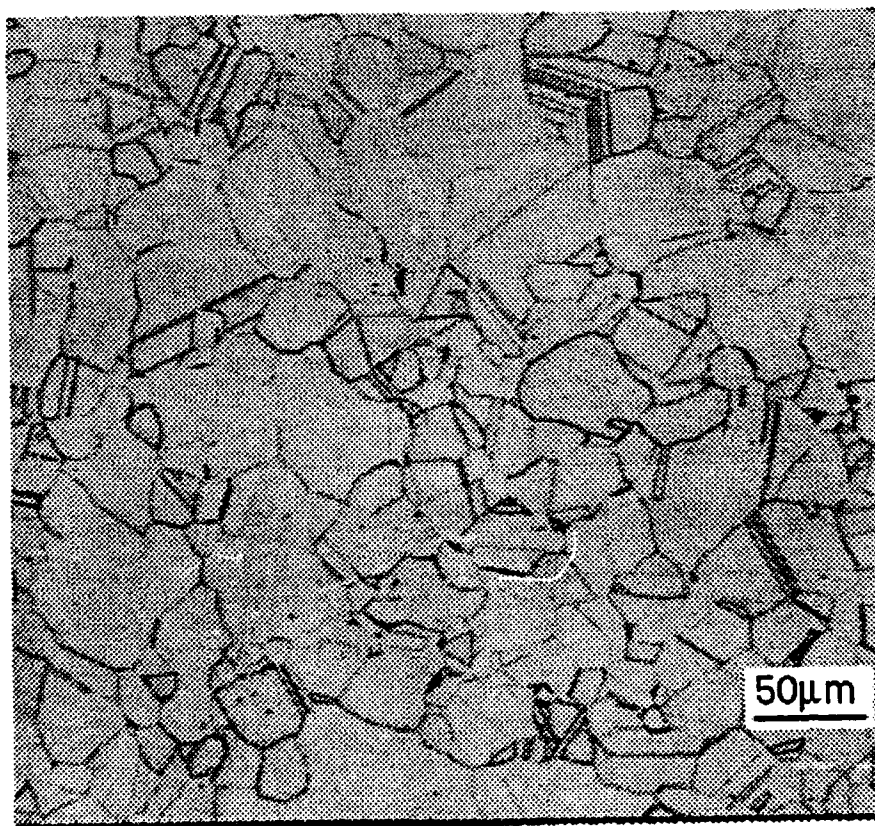
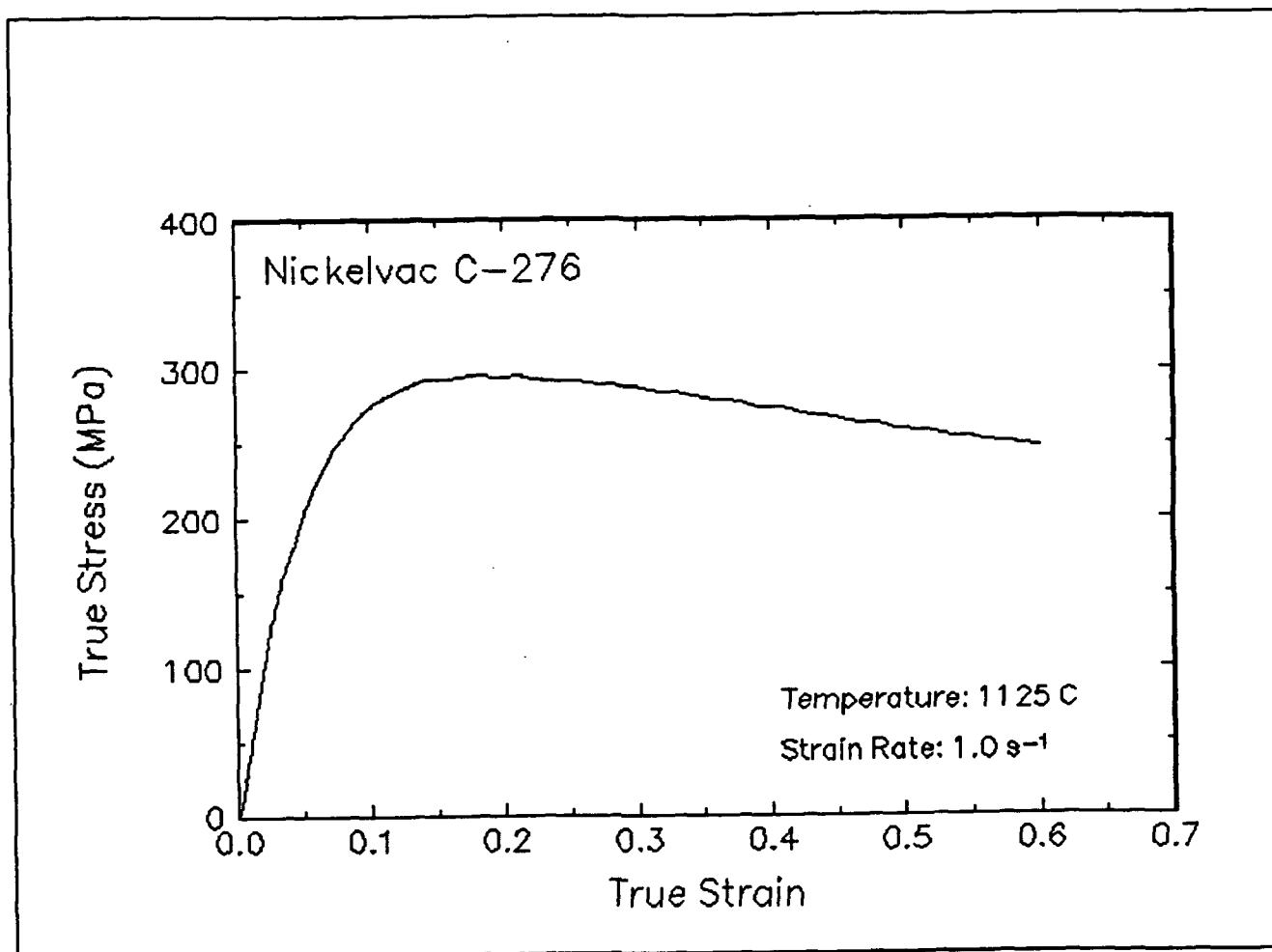


Figure 39. True stress-true strain curve and an optical micrograph from the center of the compressed sample cut through the compression axis, 1125 C and 1 s<sup>-1</sup>.



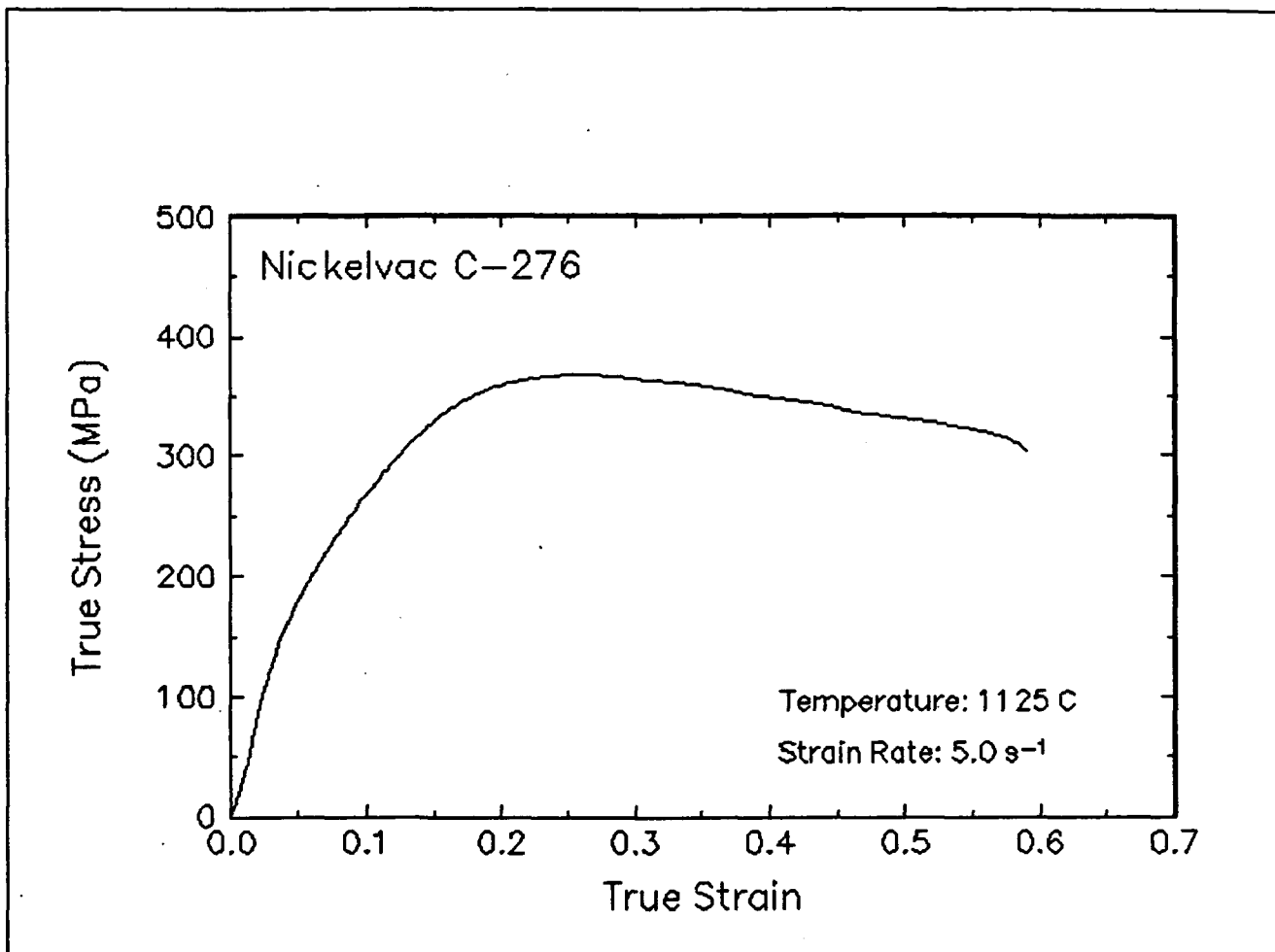


Figure 40. True stress-true strain curve, 1125 C and 5 s<sup>-1</sup>.

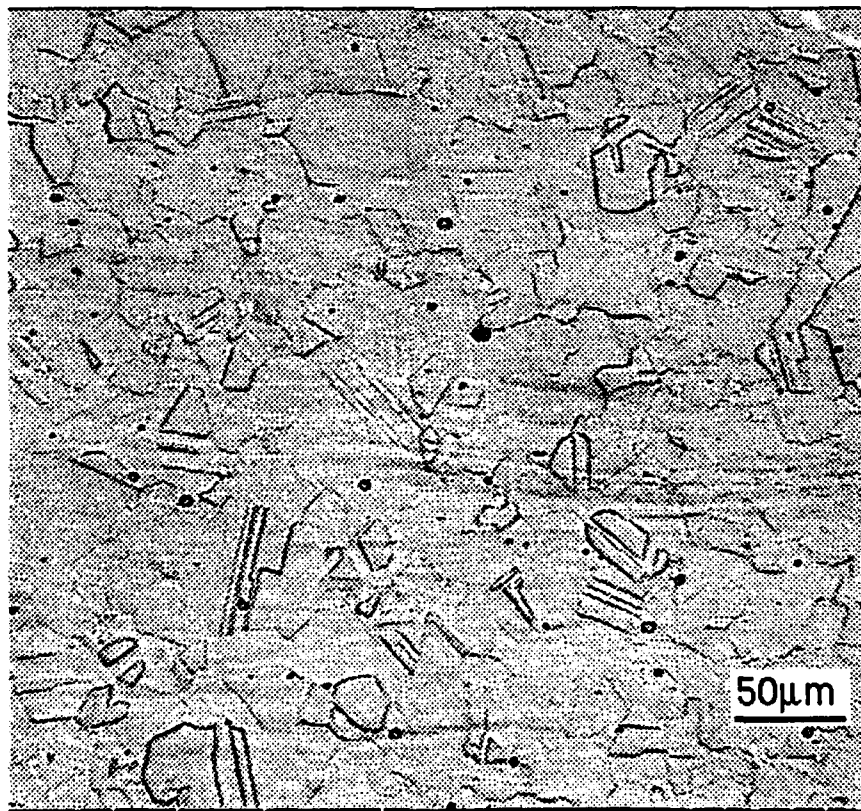
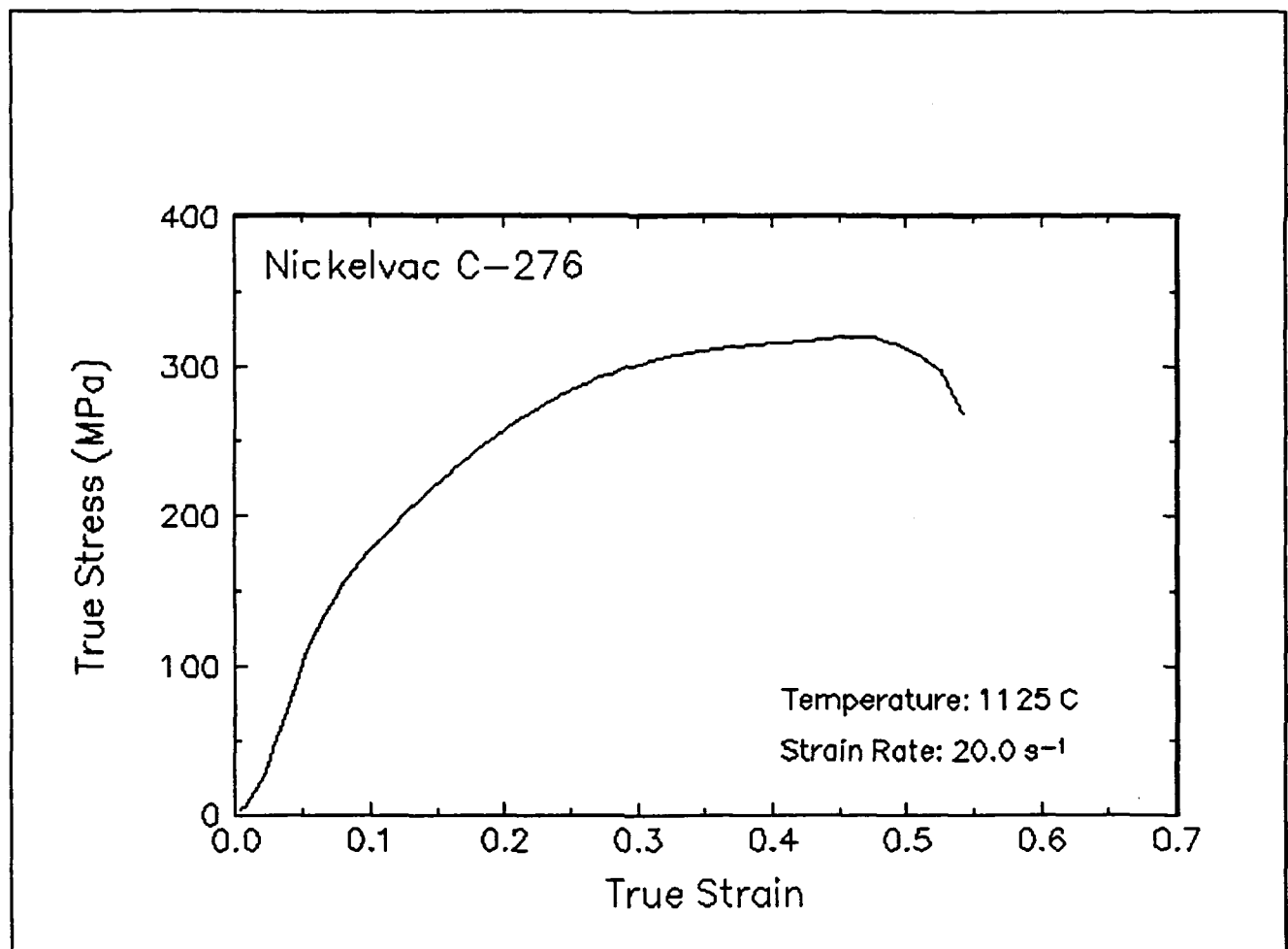


Figure 41. True stress-true strain curve and an optical micrograph from the center of the compressed sample cut through the compression axis, 1125 C and 20 s<sup>-1</sup>.

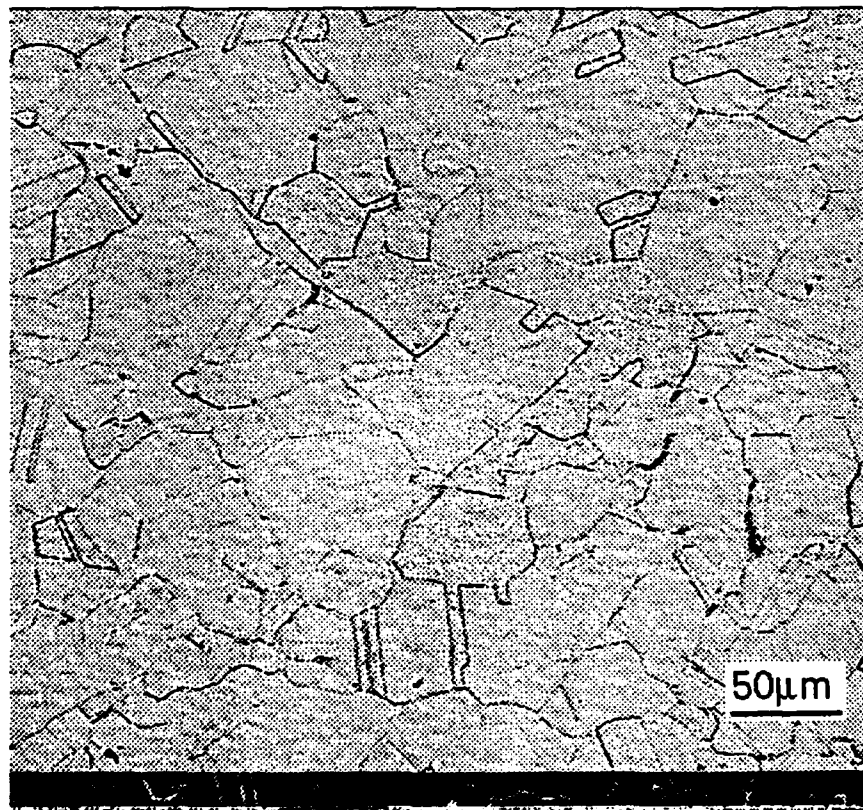
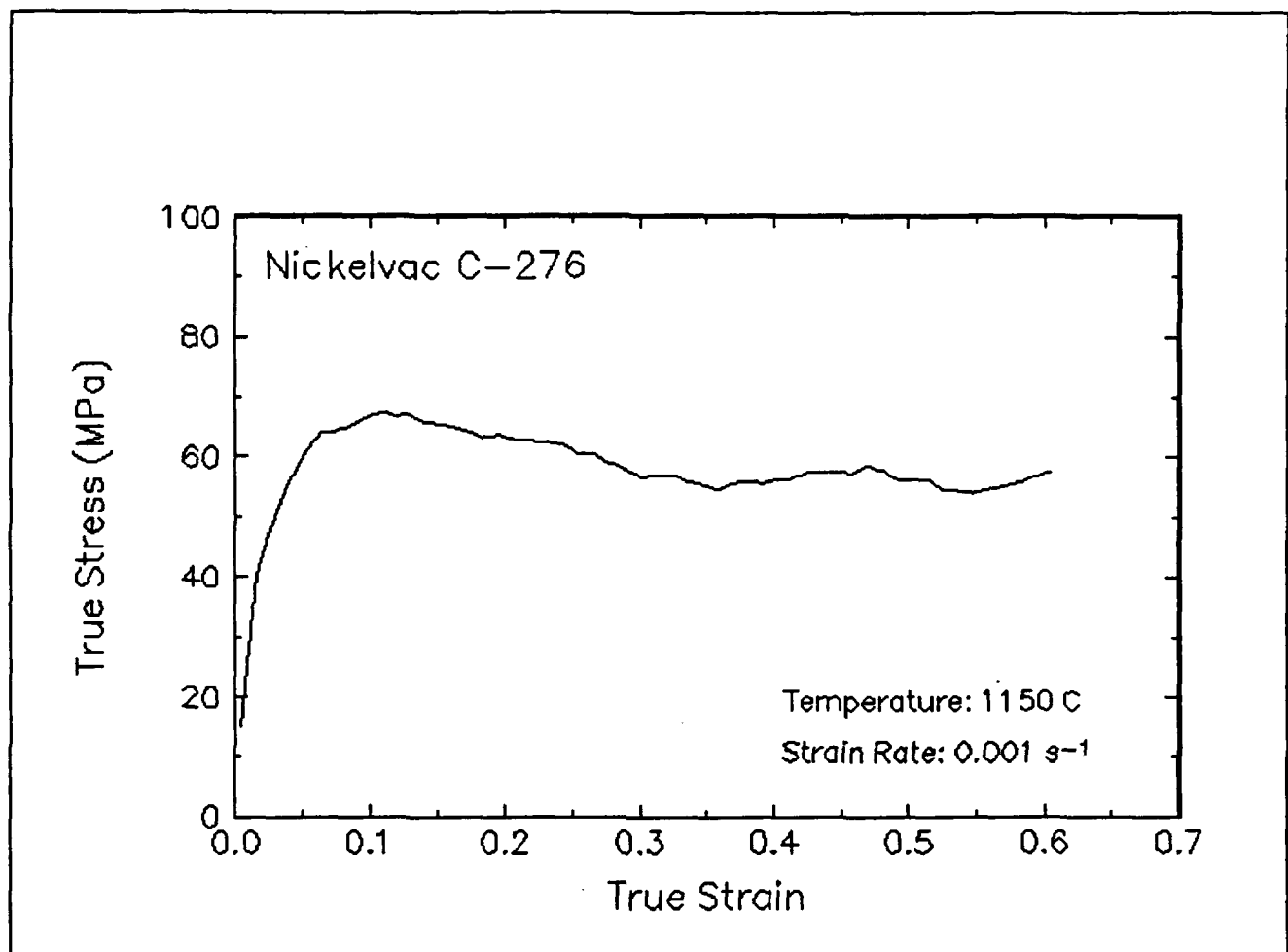


Figure 42. True stress-true strain curve and an optical micrograph from the center of the compressed sample cut through the compression axis, 1150 C and 0.001 s<sup>-1</sup>.

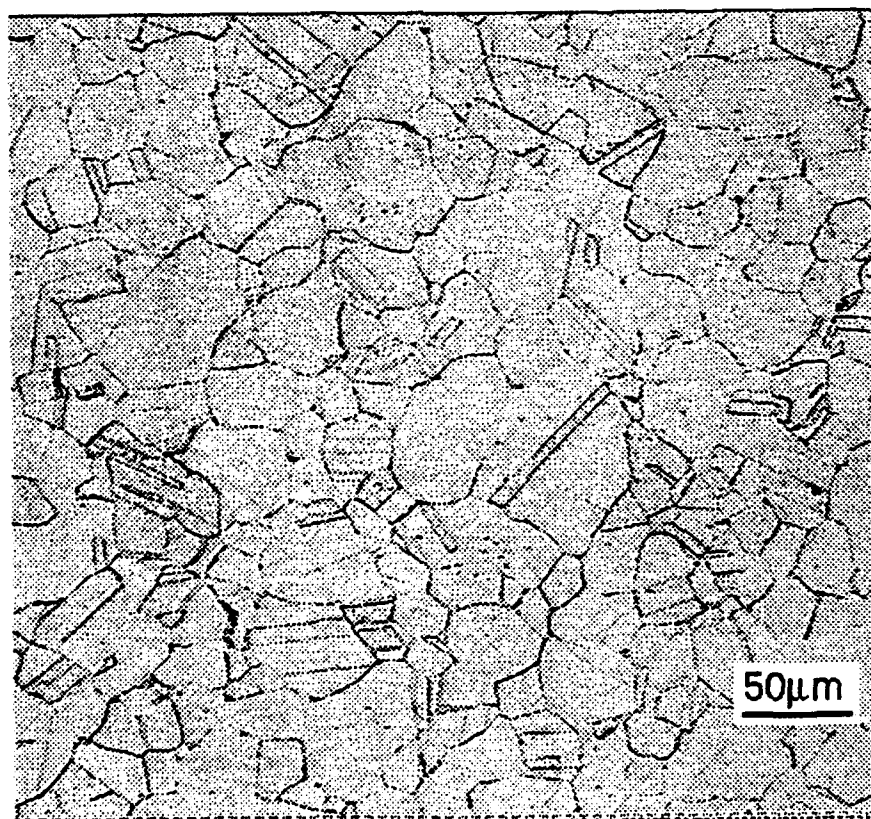
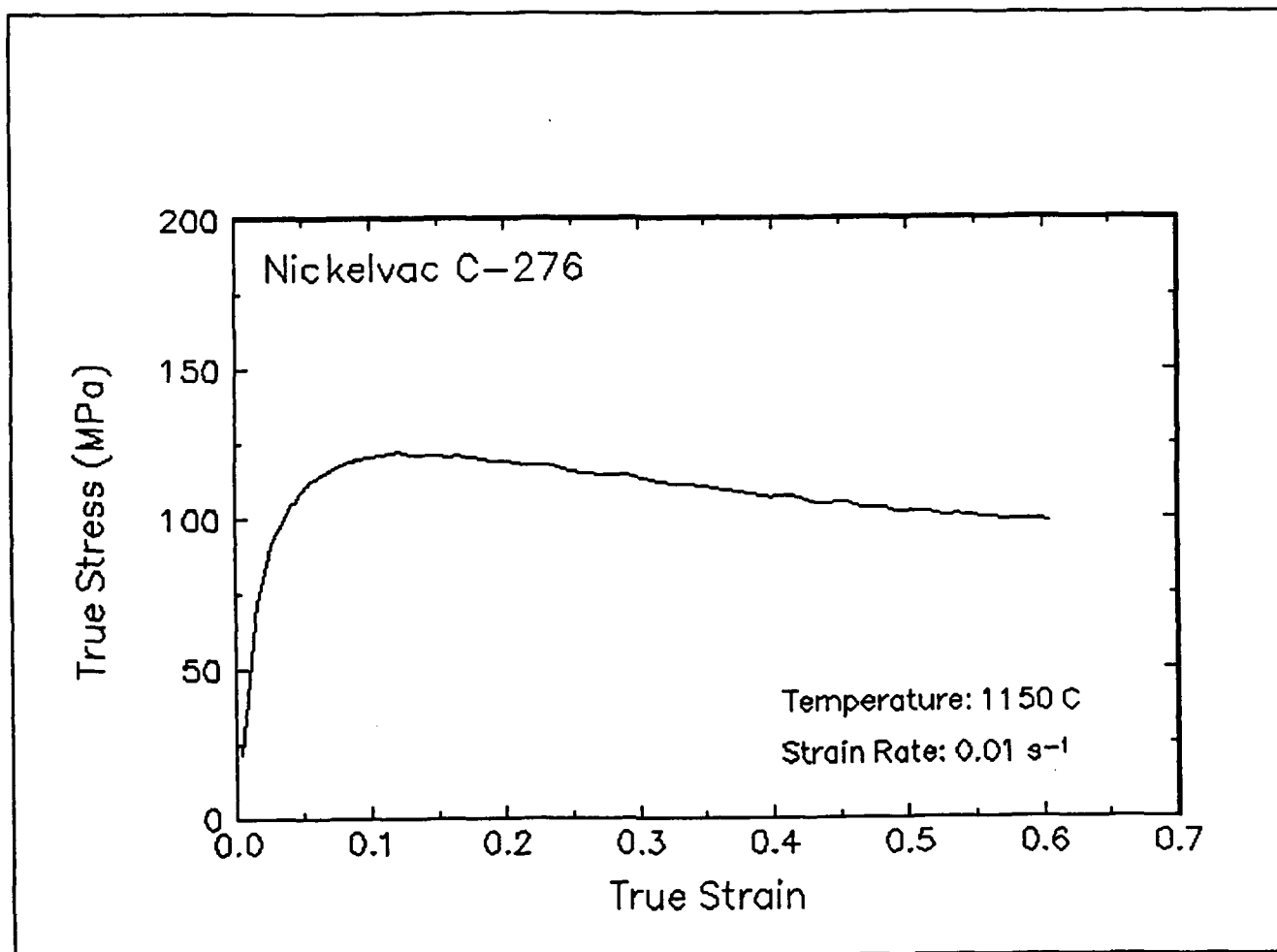


Figure 43. True stress-true strain curve and an optical micrograph from the center of the compressed sample cut through the compression axis, 1150 C and 0.01 s<sup>-1</sup>.

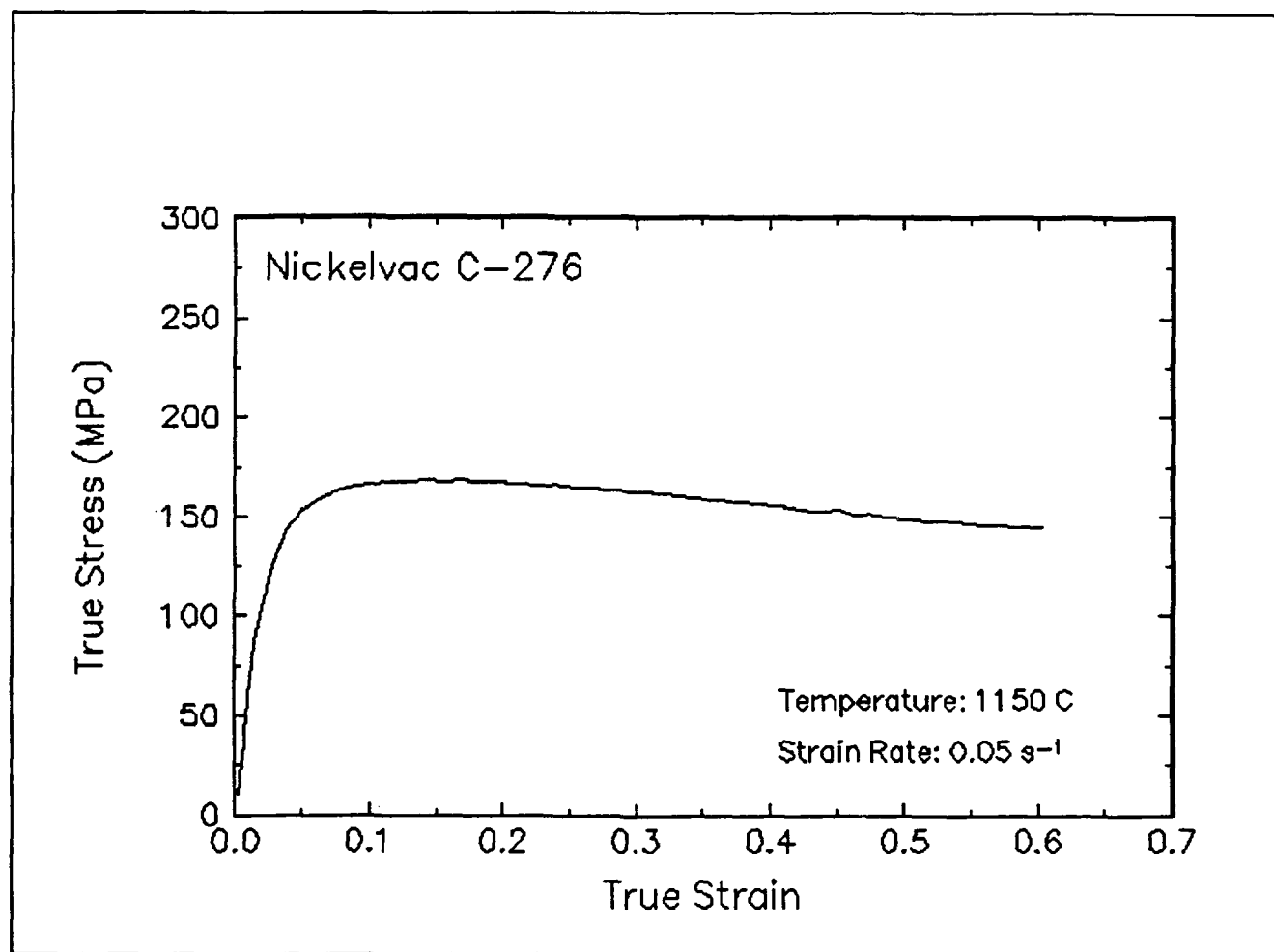


Figure 44. True stress-true strain curve, 1150 C and 0.05 s<sup>-1</sup>.

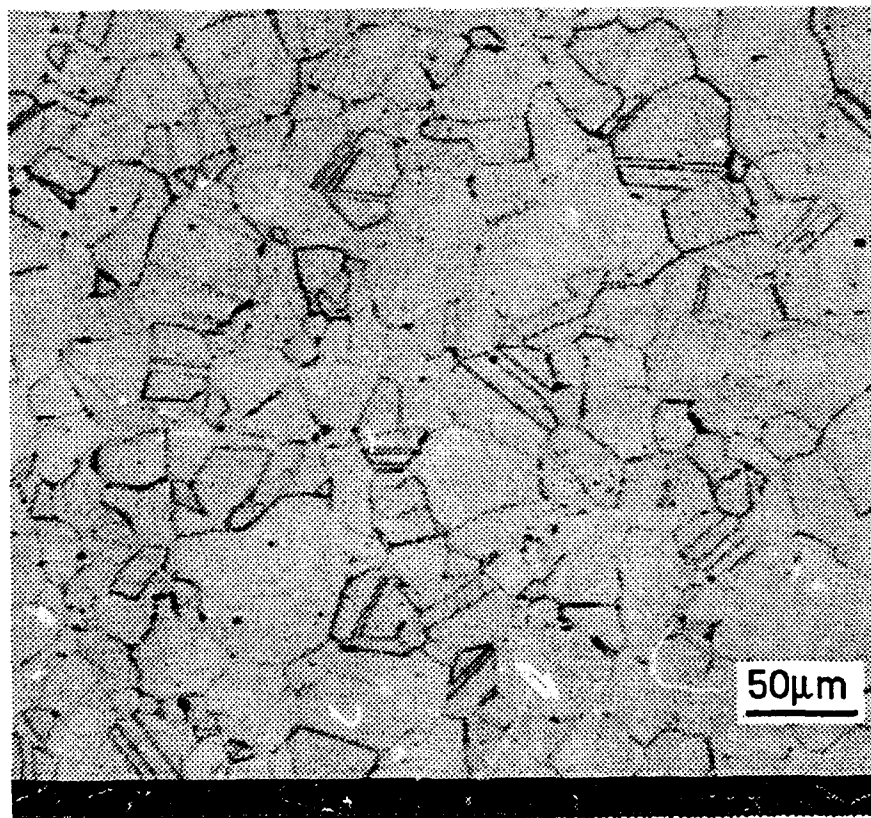
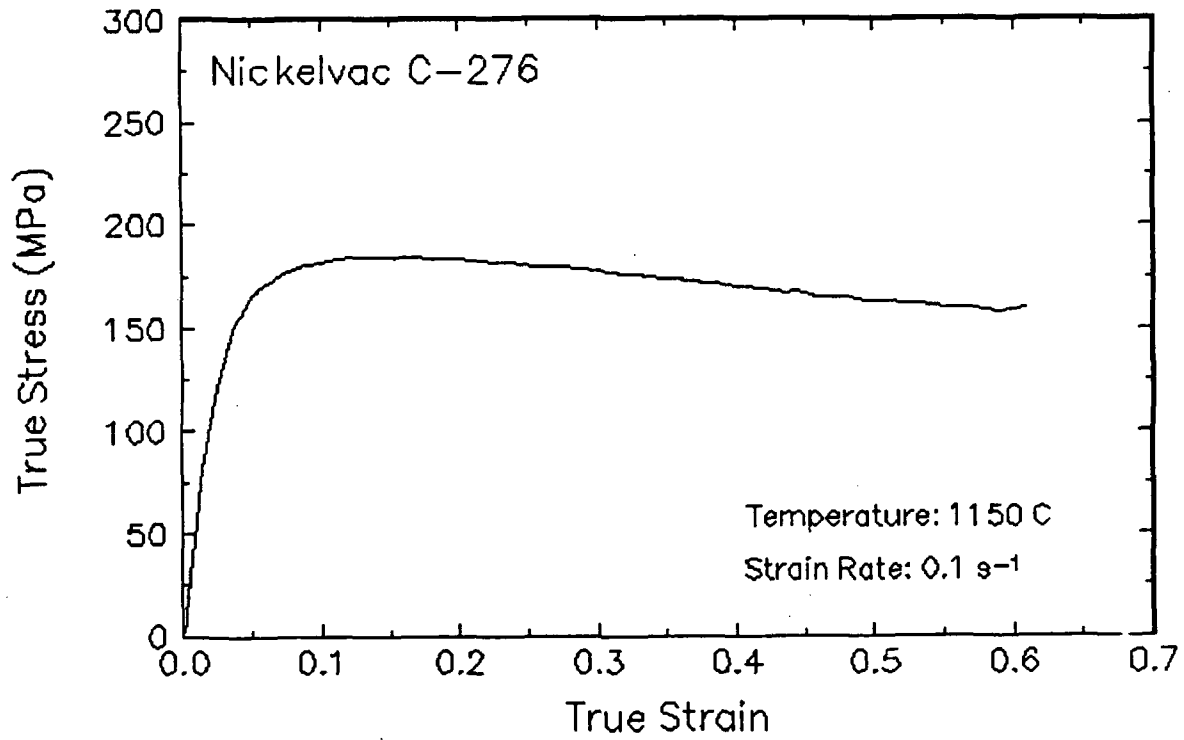


Figure 45. True stress-true strain curve and an optical micrograph from the center of the compressed sample cut through the compression axis, 1150 C and 0.1 s<sup>-1</sup>.

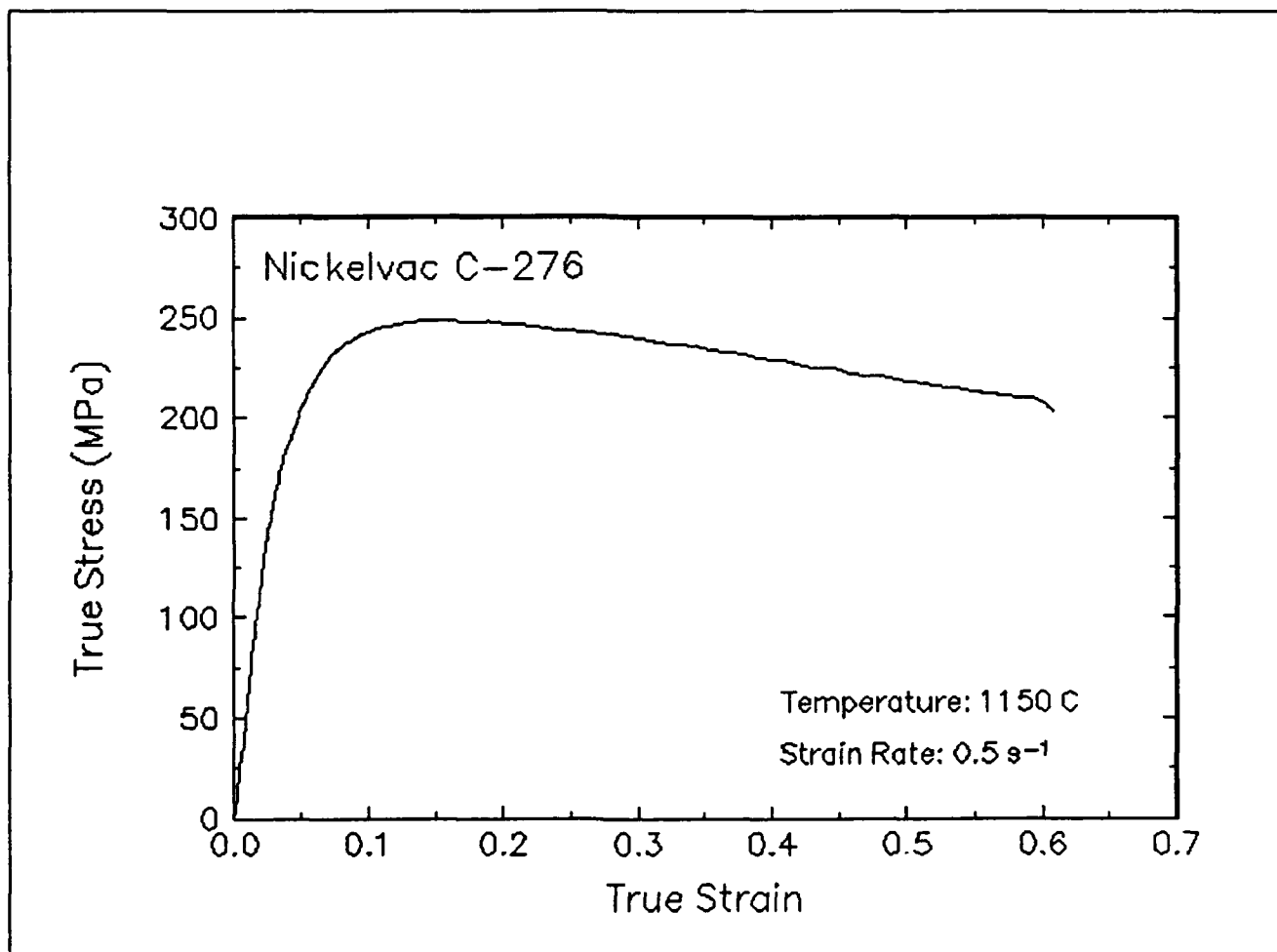


Figure 46. True stress-true strain curve, 1150 C and 0.5 s<sup>-1</sup>.

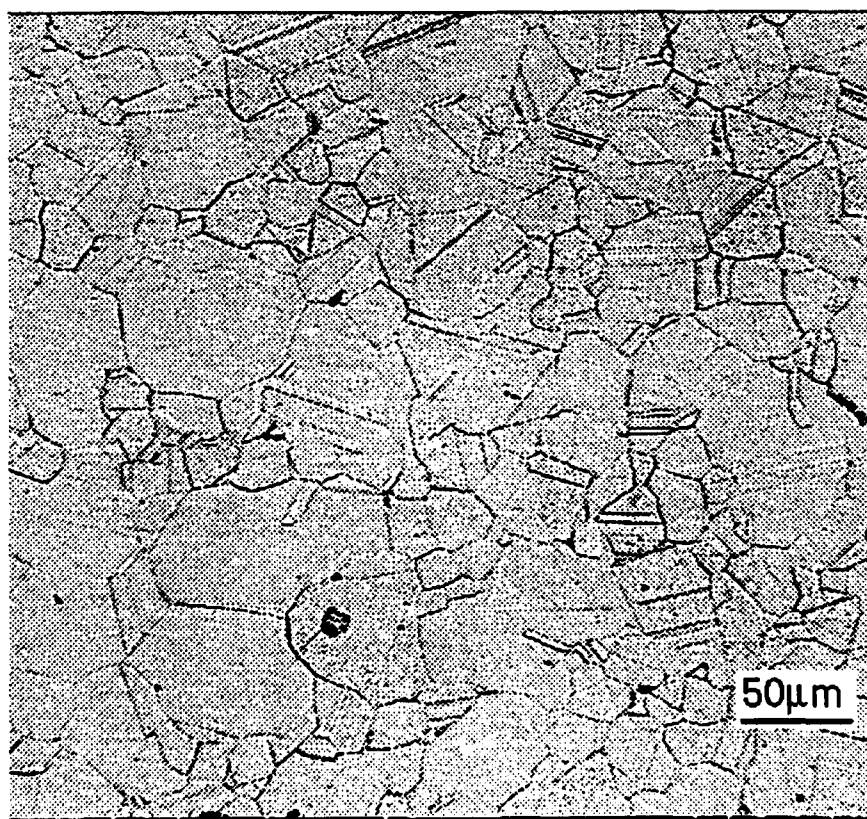
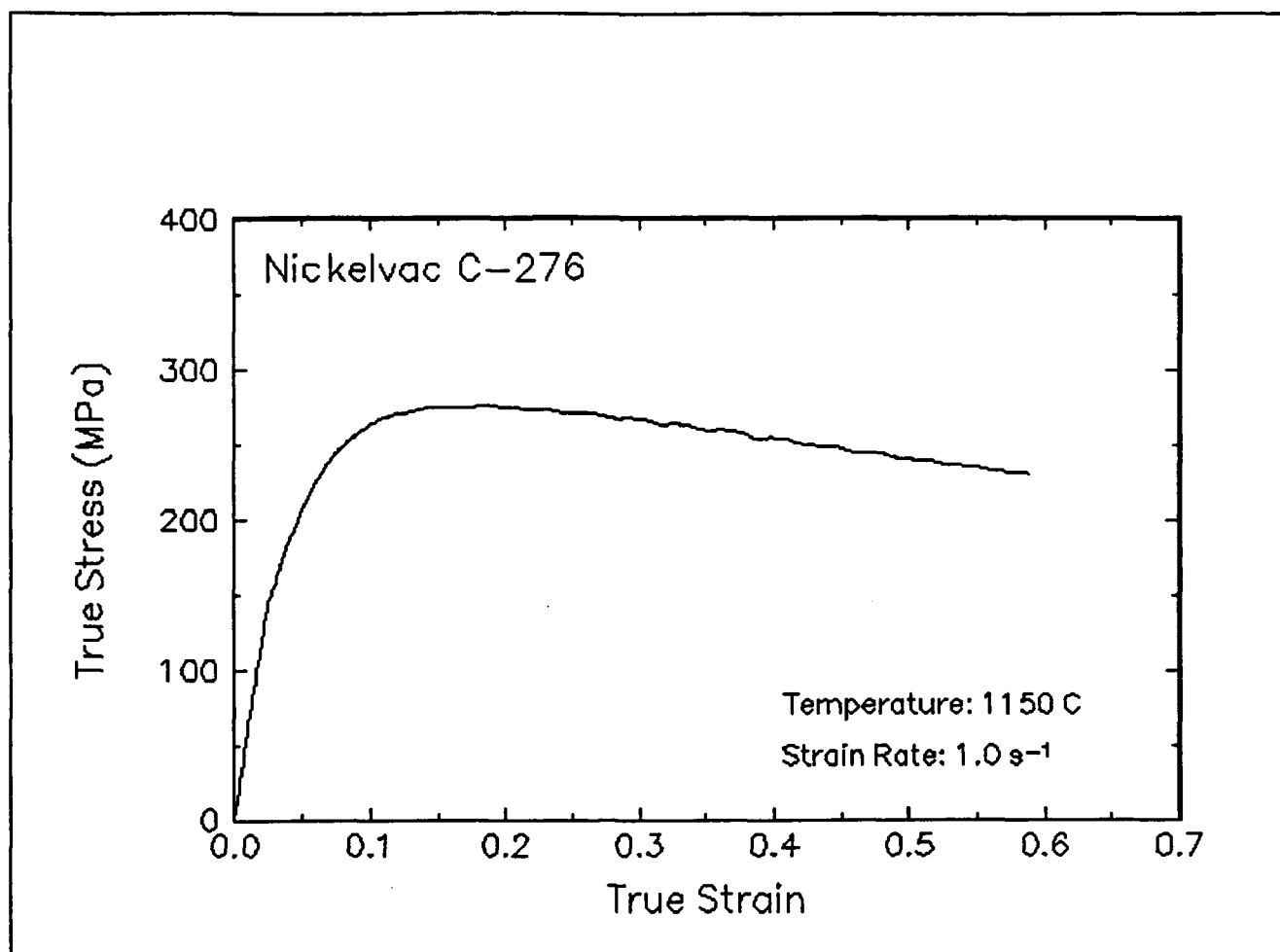


Figure 47. True stress-true strain curve and an optical micrograph from the center of the compressed sample cut through the compression axis, 1150 C and 1 s<sup>-1</sup>.



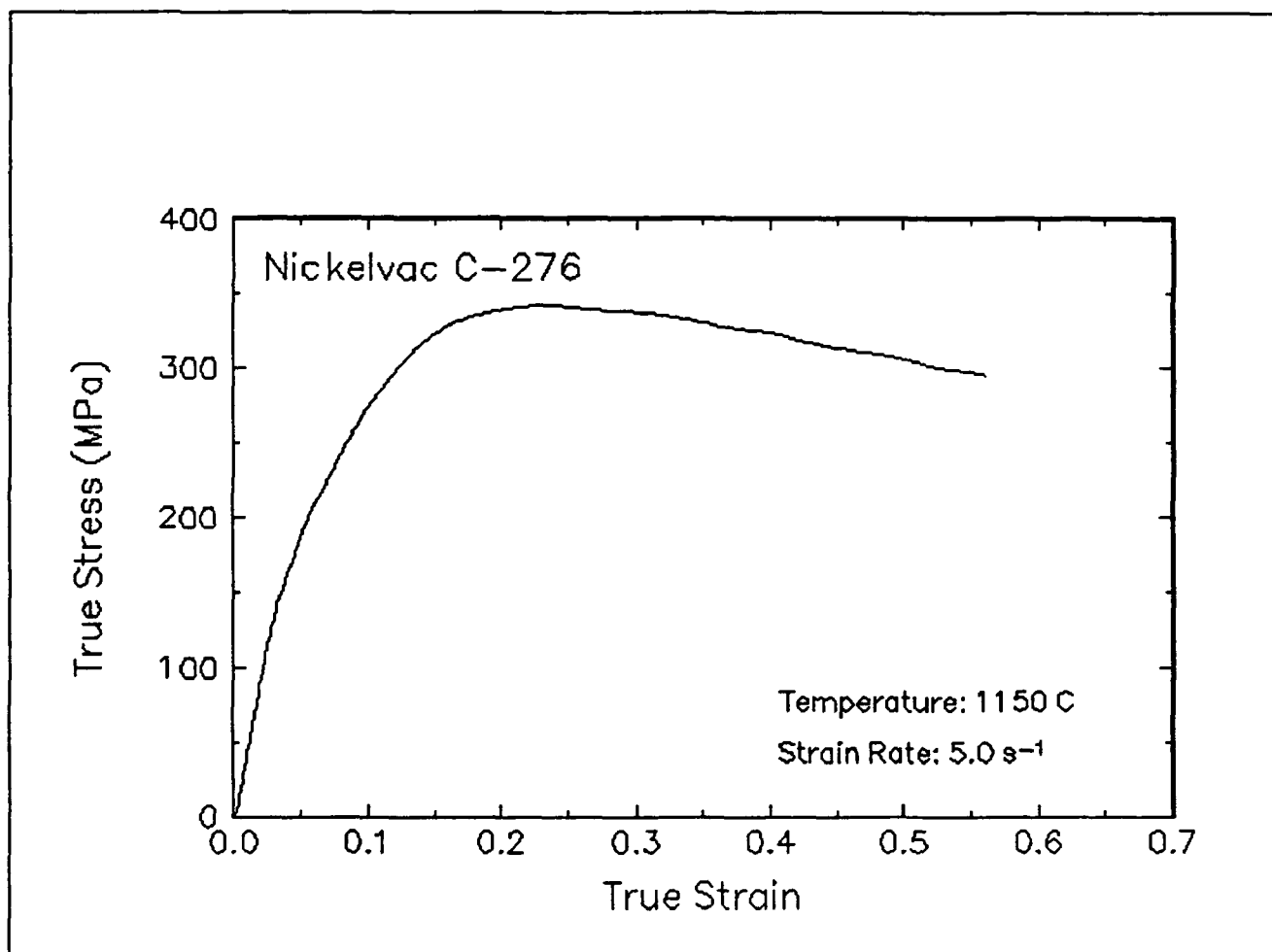


Figure 48. True stress-true strain curve, 1150 C and 5 s<sup>-1</sup>.

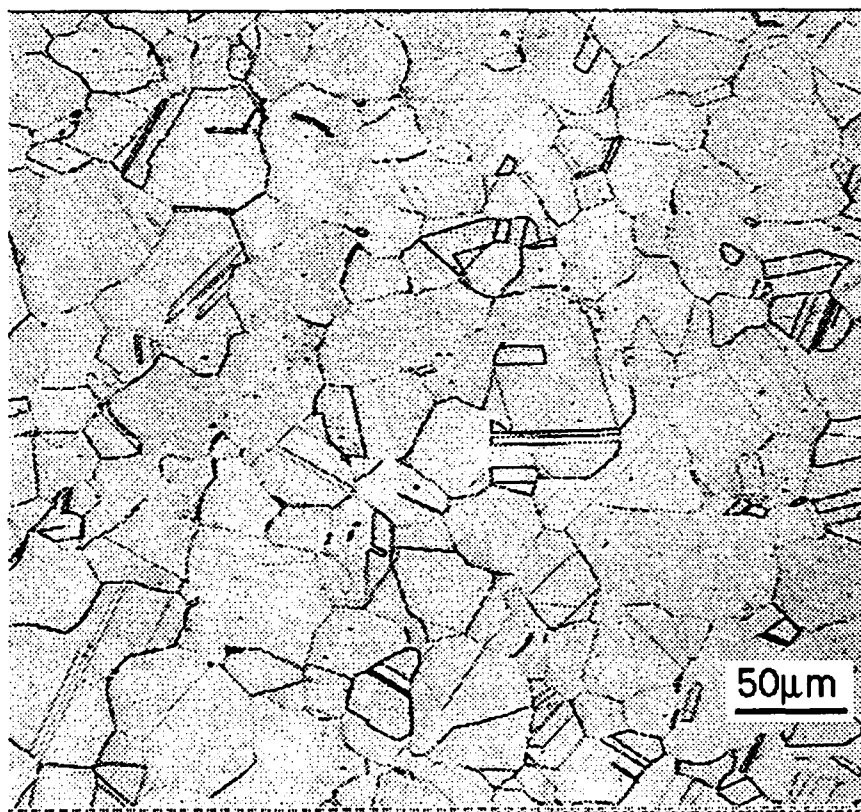
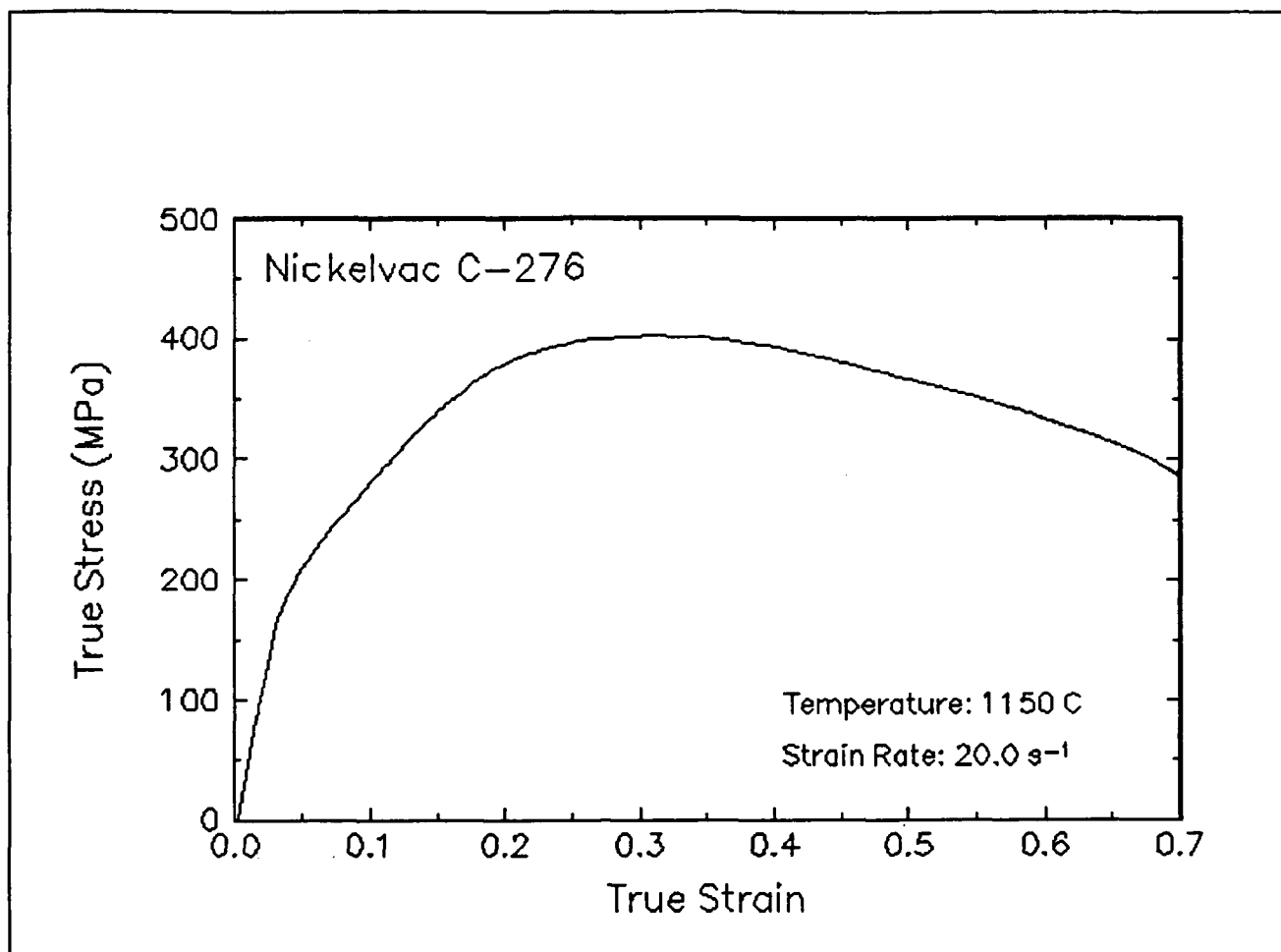


Figure 49. True stress-true strain curve and an optical micrograph from the center of the compressed sample cut through the compression axis, 1150 C and 20 s<sup>-1</sup>.

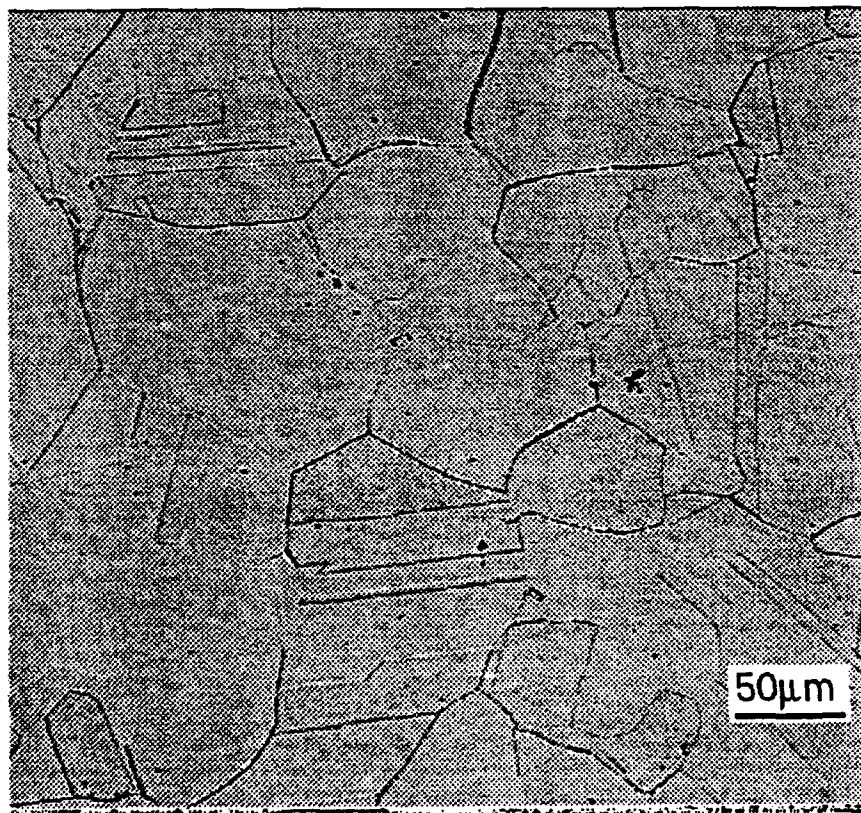
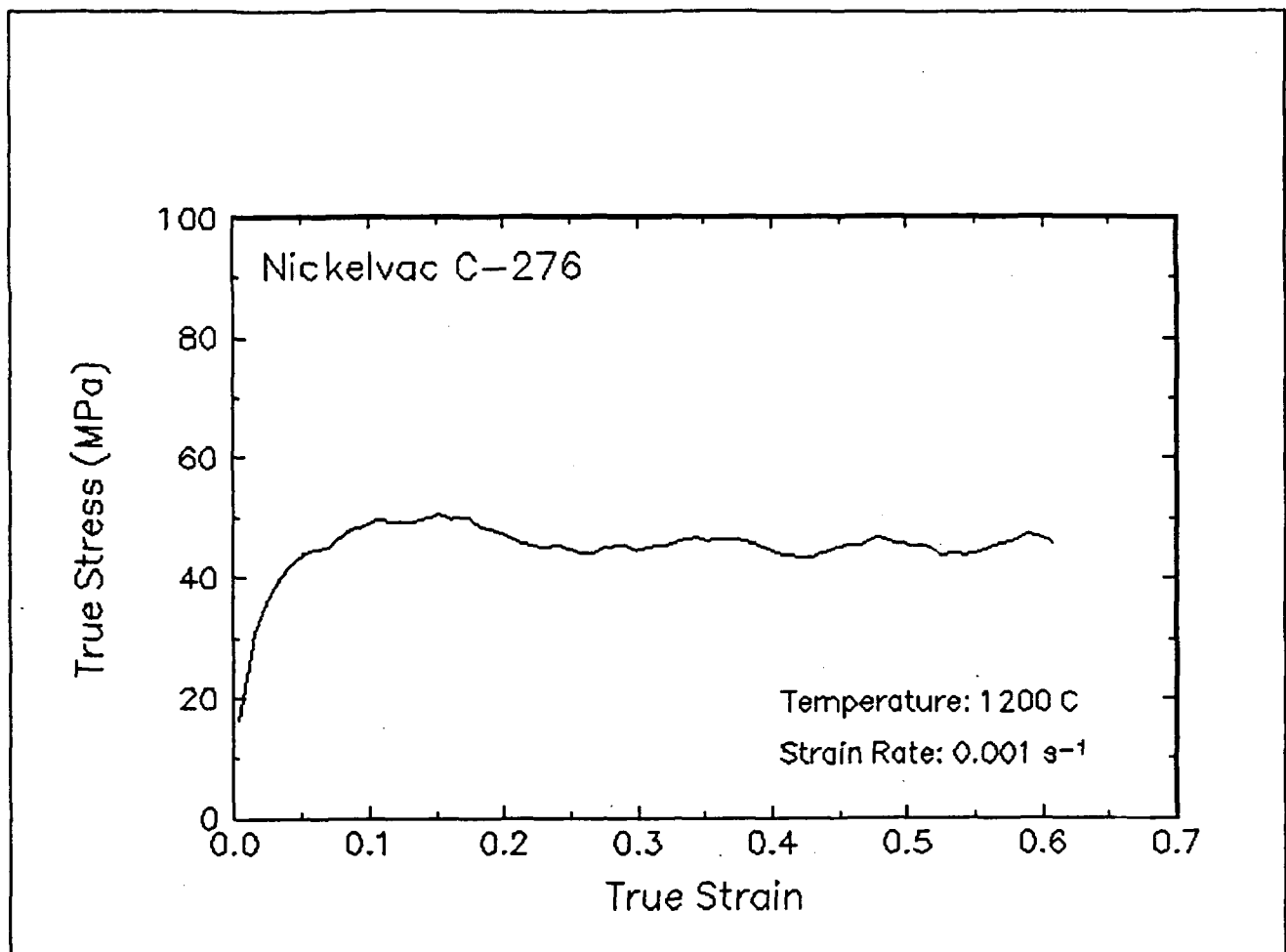


Figure 50. True stress-true strain curve and an optical micrograph from the center of the compressed sample cut through the compression axis, 1200 C and 0.001 s<sup>-1</sup>.

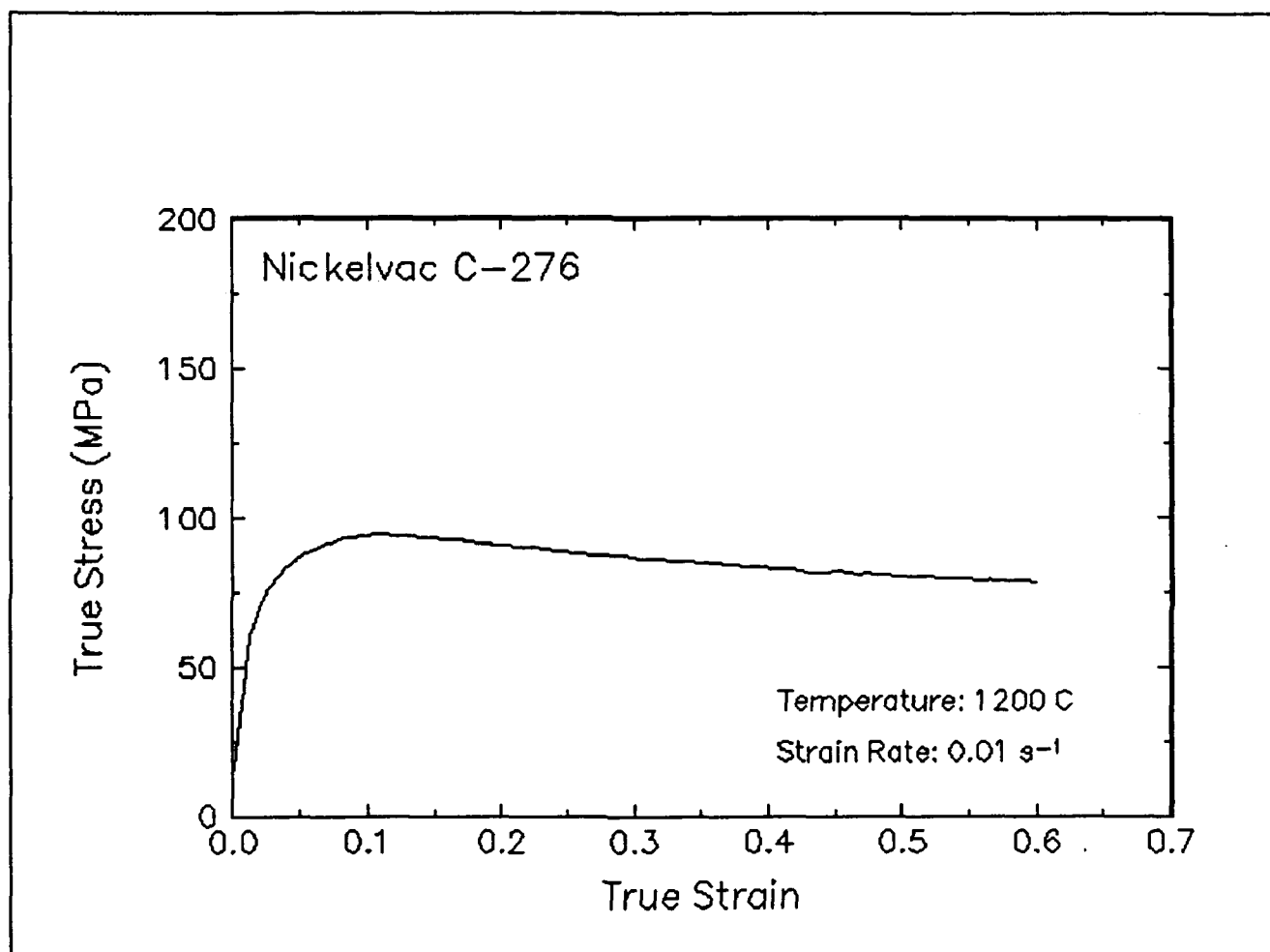


Figure 51. True stress-true strain curve, 1200 C and 0.01 s<sup>-1</sup>.

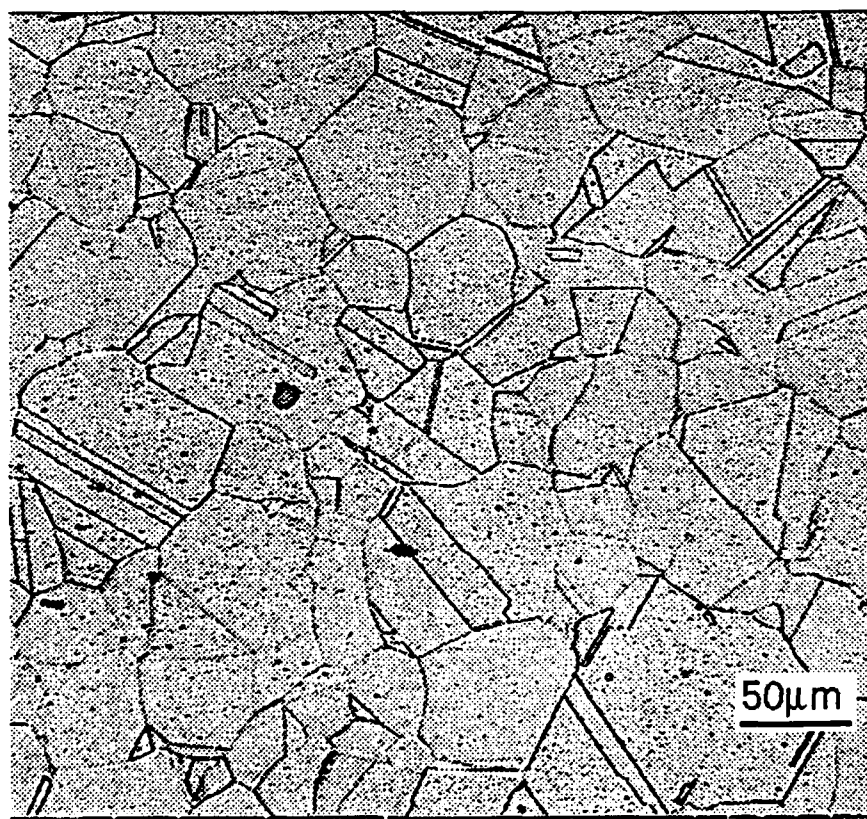
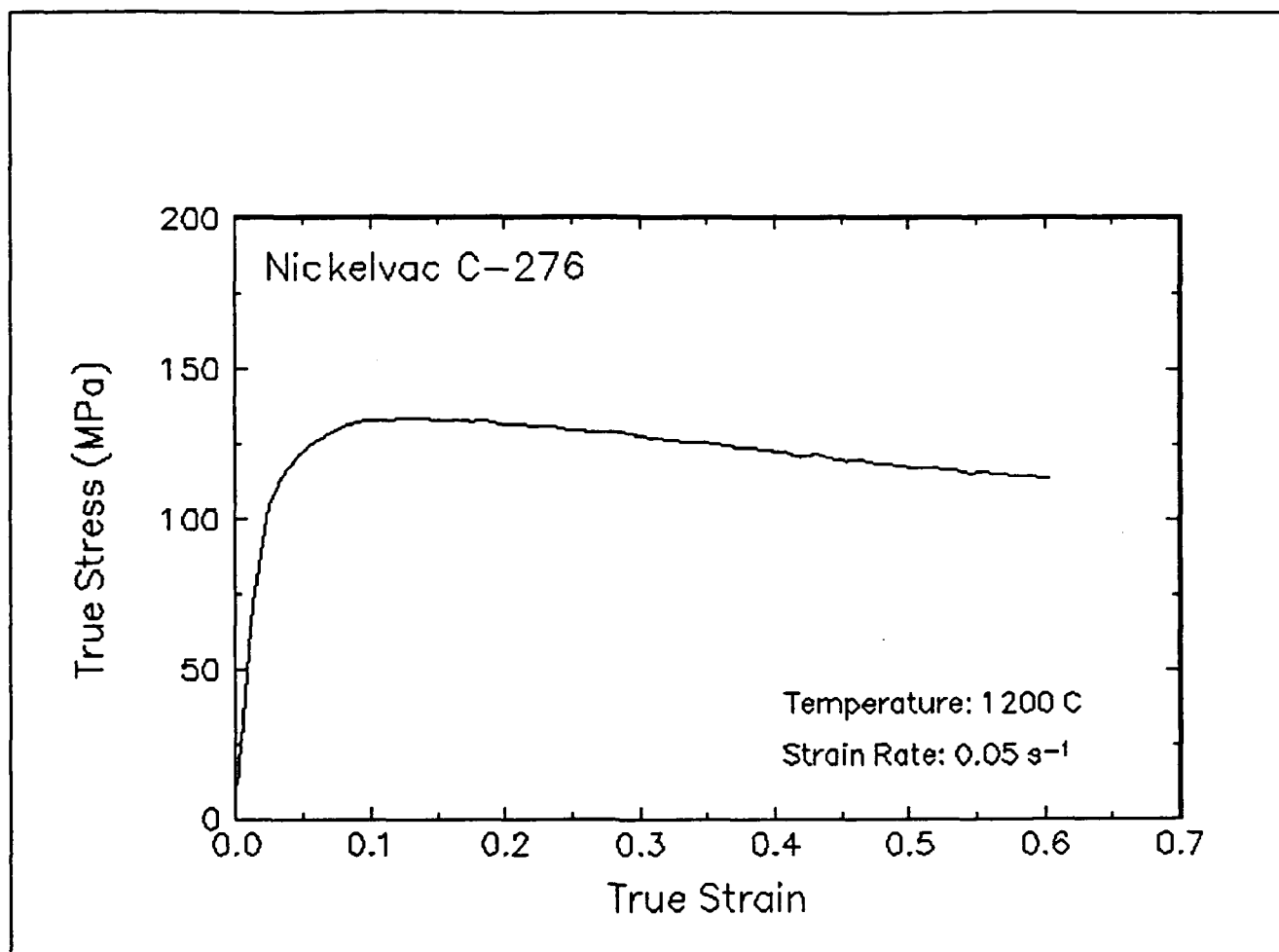


Figure 52. True stress-true strain curve and an optical micrograph from the center of the compressed sample cut through the compression axis, 1200 C and 0.05 s<sup>-1</sup>.

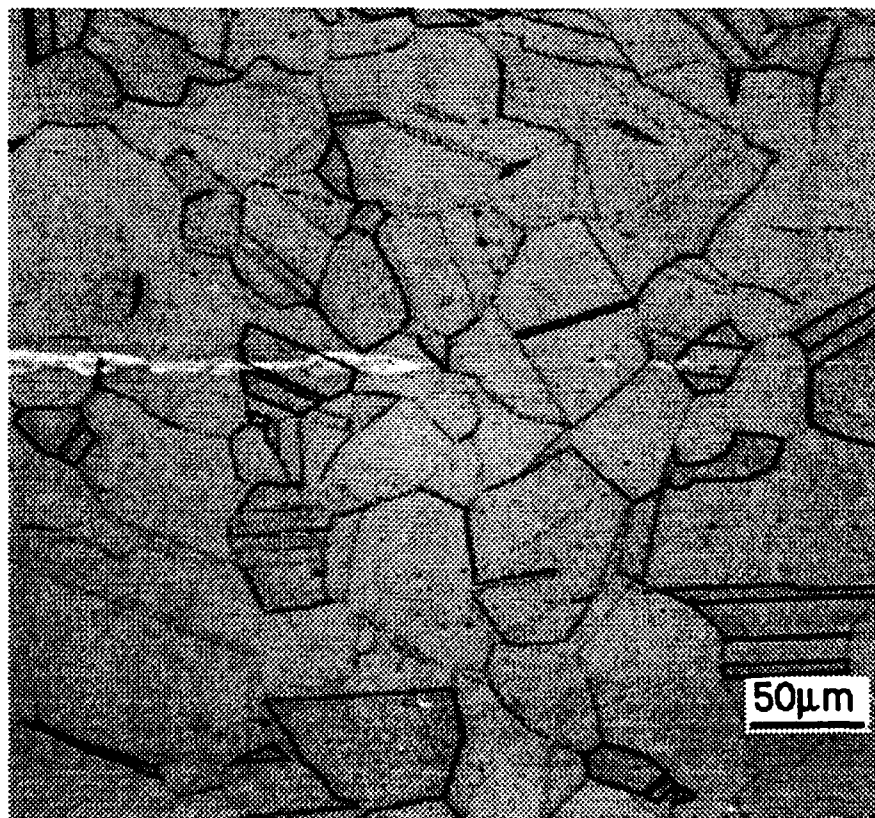
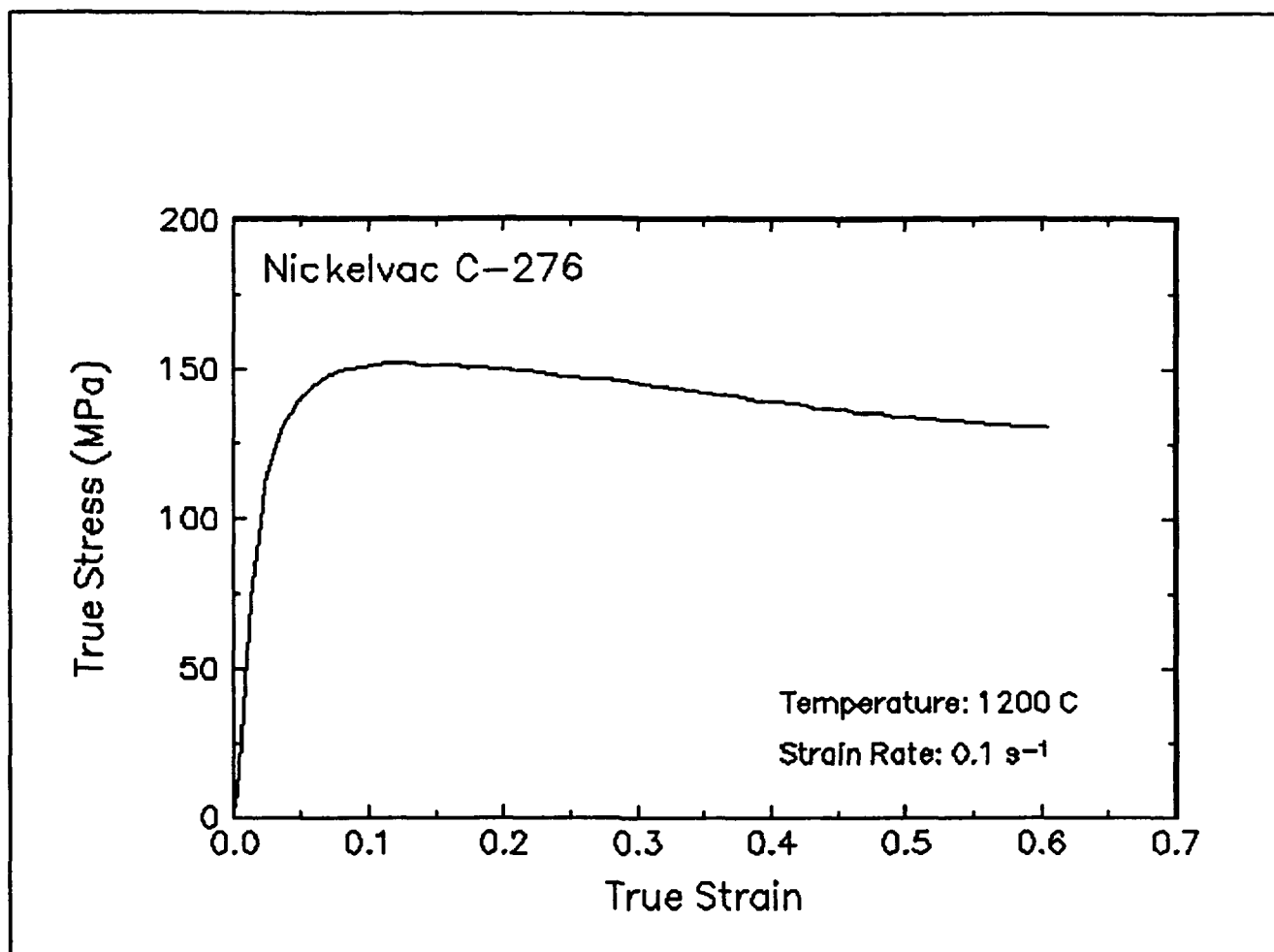


Figure 53. True stress-true strain curve and an optical micrograph from the center of the compressed sample cut through the compression axis, 1200 C and 0.1 s<sup>-1</sup>.

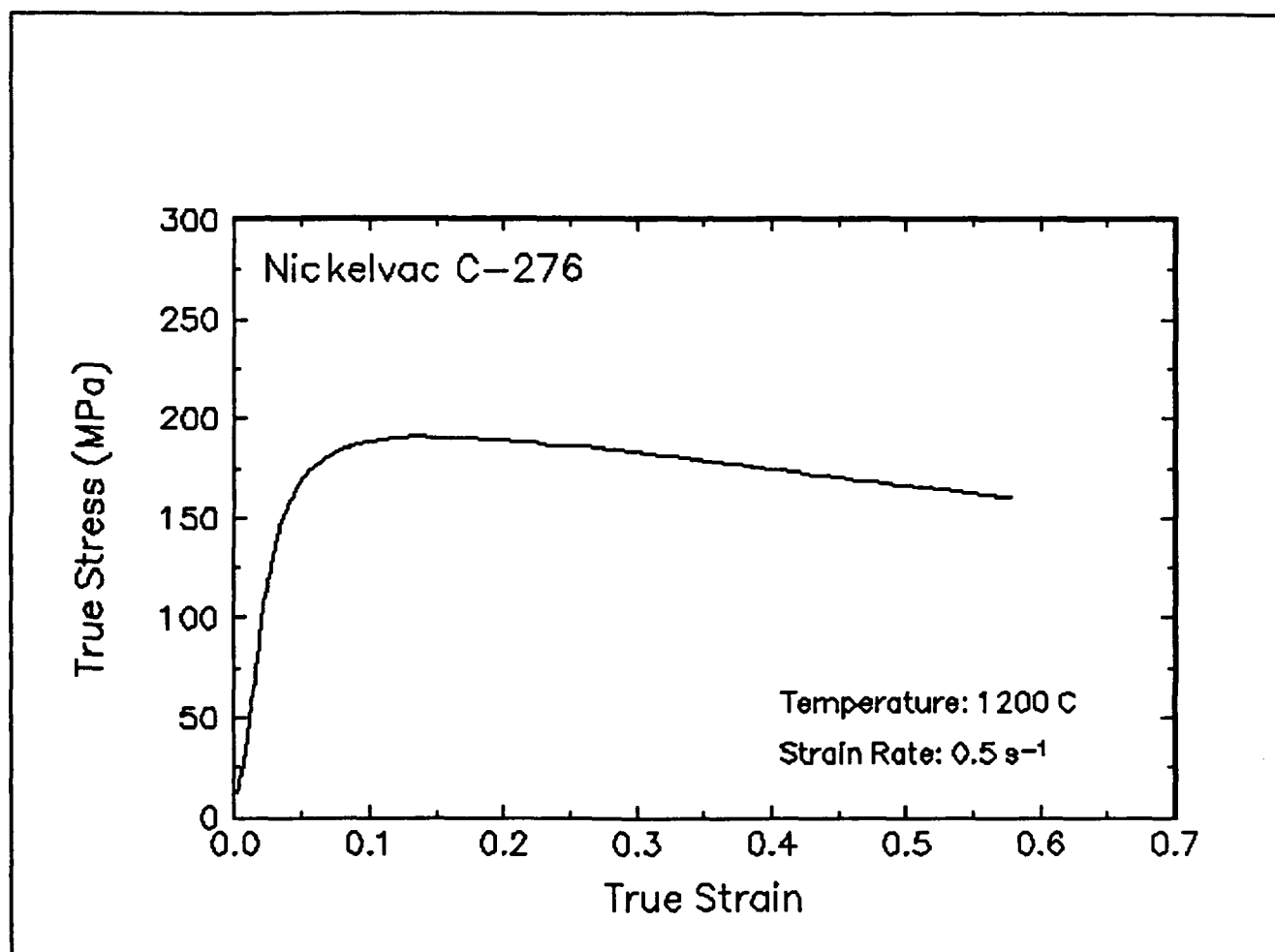


Figure 54. True stress-true strain curve, 1200 C and 0.5 s<sup>-1</sup>.

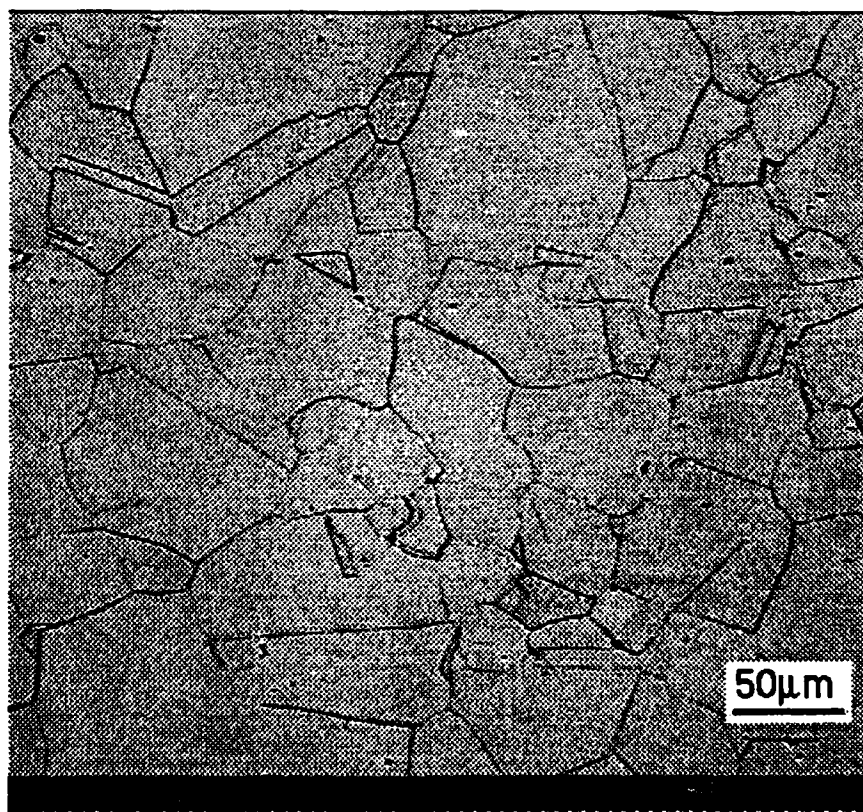
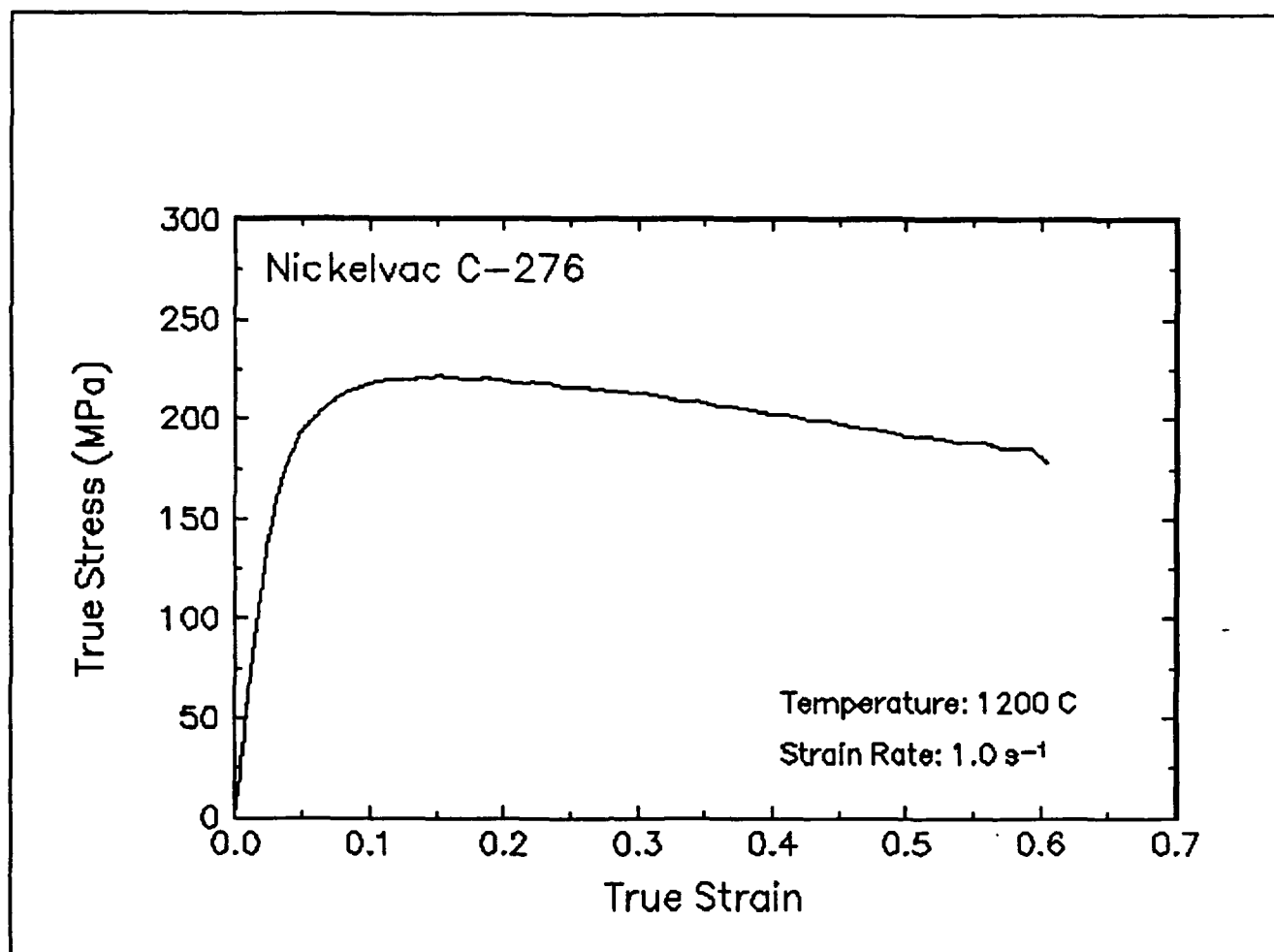


Figure 55. True stress-true strain curve and an optical micrograph from the center of the compressed sample cut through the compression axis, 1200 C and 1 s<sup>-1</sup>.



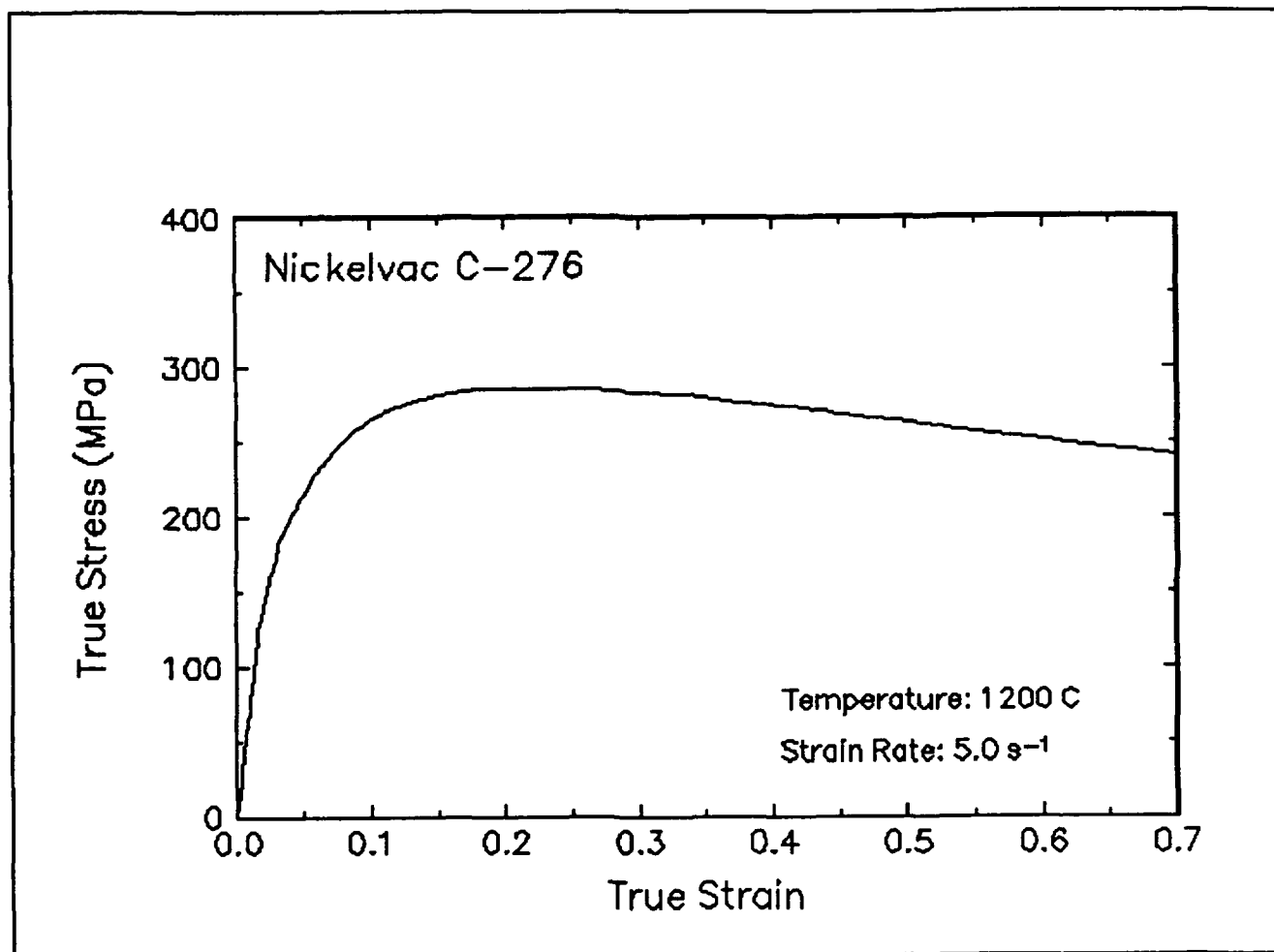


Figure 56. True stress-true strain curve, 1200 C and 5 s<sup>-1</sup>.

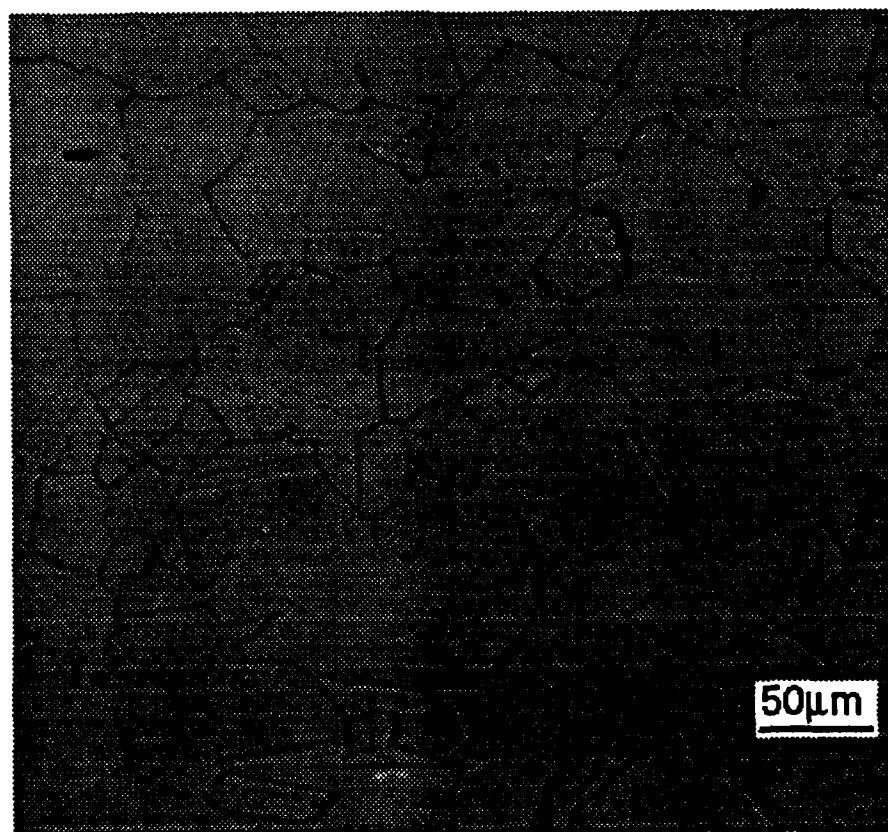
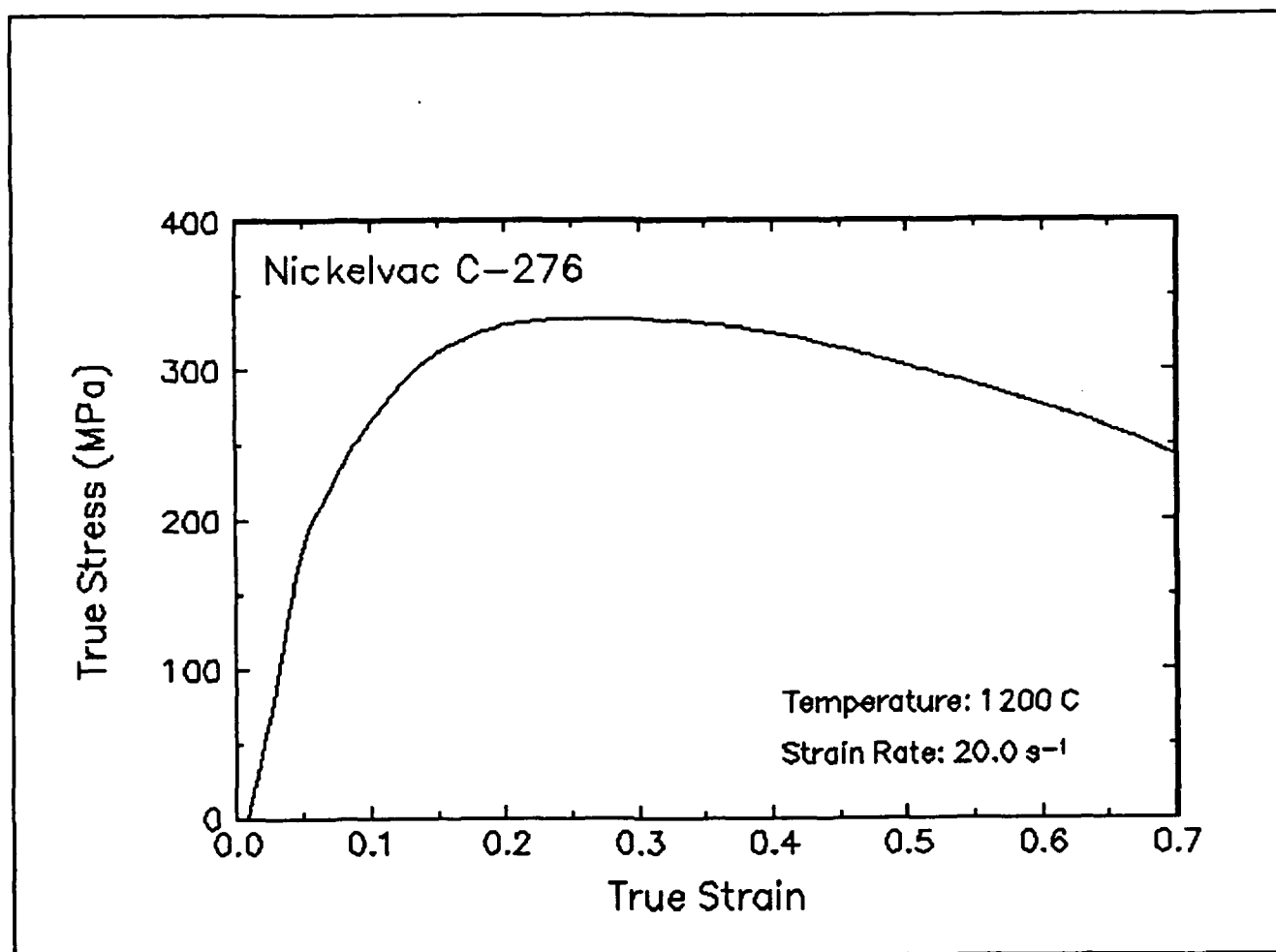


Figure 57. True stress-true strain curve and an optical micrograph from the center of the compressed sample cut through the compression axis, 1200 C and 20 s<sup>-1</sup>.

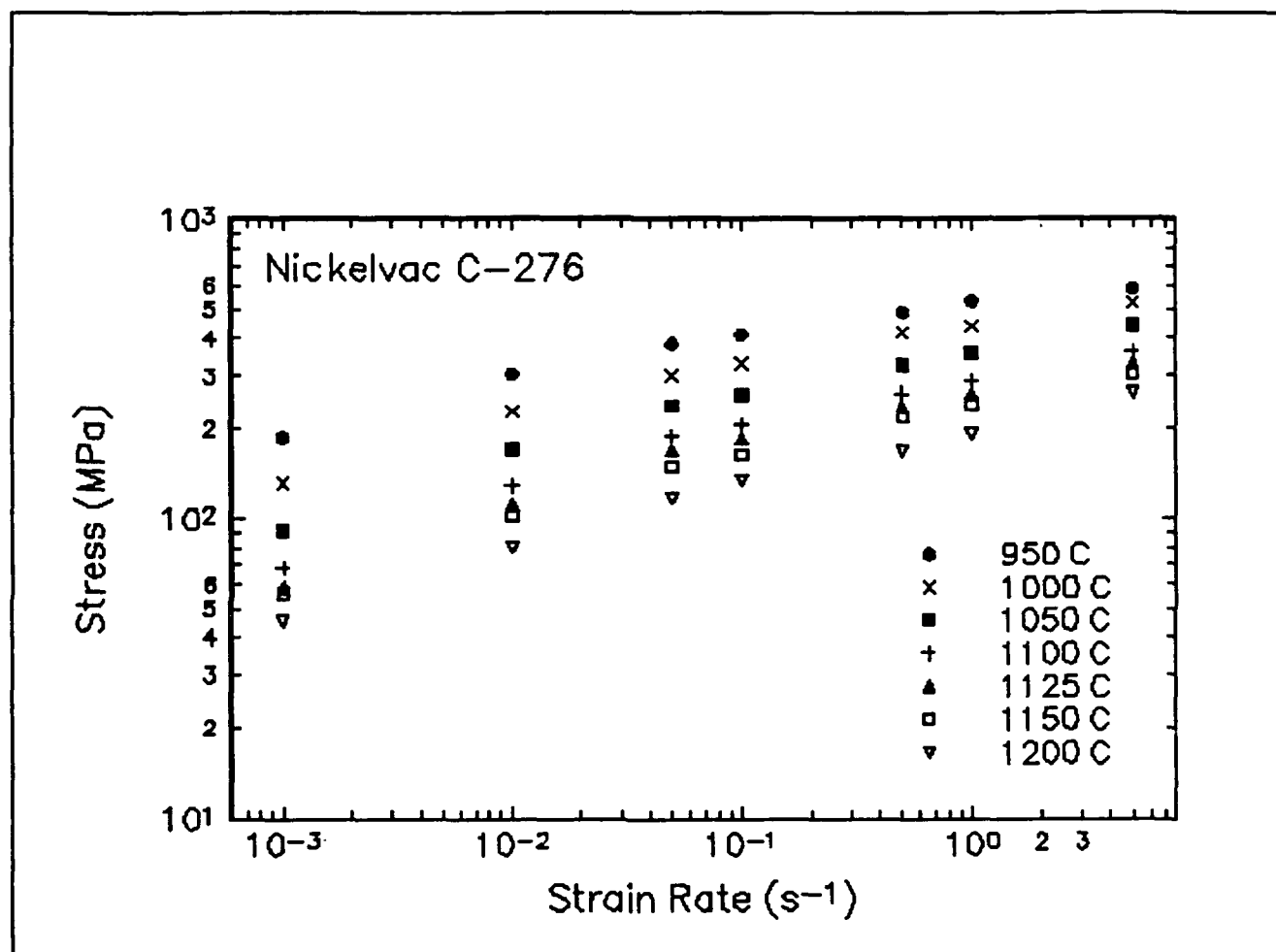


Figure 58. Effect of strain rate on stress in log-log scale at a true strain of 0.5 for Nickelvac C-276.

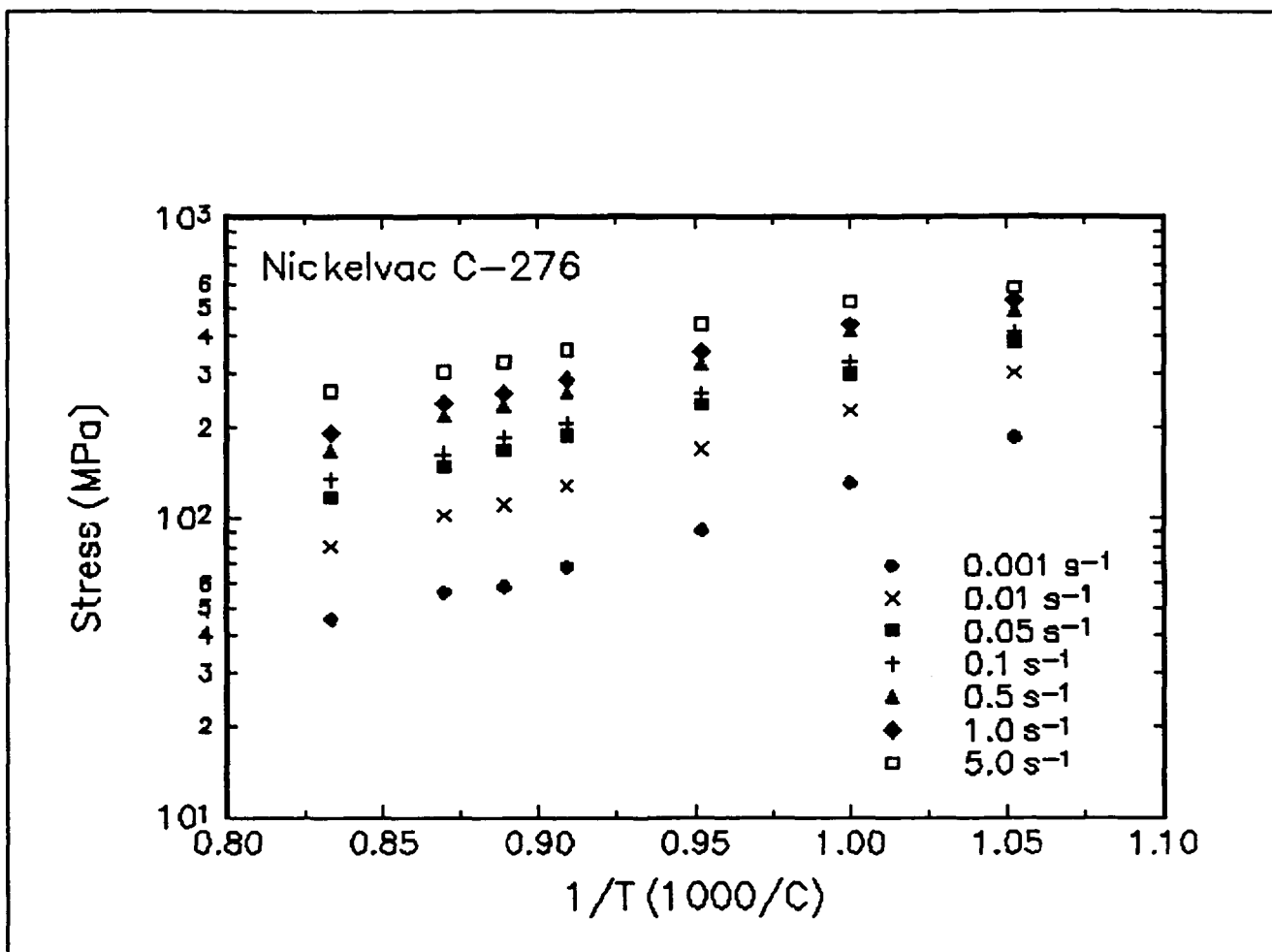


Figure 59. Effect of temperature on stress at a true strain of 0.5 for Nickelvac C-276.

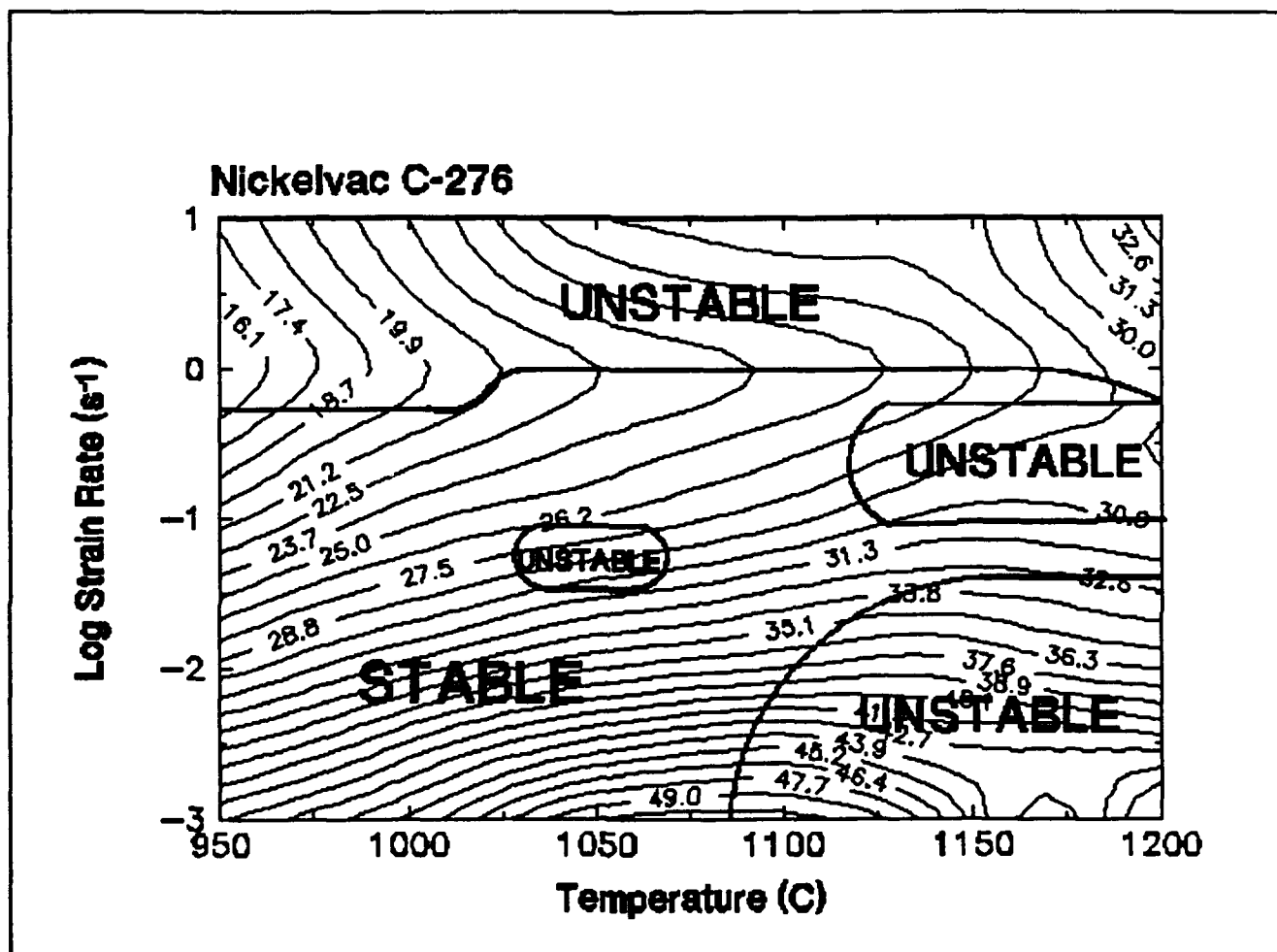


Figure 60. Processing map of Nickelvac C-276 at a true strain of 0.5.

## Summary

Compression tests have been performed on Nickelvac C-276 over a wide range of temperatures and strain rates. The experimental conditions used in this work are representative of those used in metalforming practices. From the stress-strain curves, the flow behavior was characterized and a processing map indicating the optimum processing condition was generated. This condition is 1075 C and  $10^{-3} \text{ s}^{-1}$ .

The deformed microstructures were characterized from the quenched specimens by optical microscopy and are presented, for selective testing conditions only, under the stress-strain curves.

### Implementation of Data Provided by the Atlas of Formability

The Atlas of Formability program provides ample data on flow behavior of various important engineering materials in the temperature and strain rate regime commonly used in metalworking processes. The data are valuable in design and problem solving in metalworking processes of advanced materials. Microstructural changes with temperature and strain rates are also provided in the Bulletin, which helps the design engineer to select processing parameters leading to the desired microstructure.

The data can also be used to construct processing map using dynamic material modeling approach to determine stable and unstable regions in terms of temperature and strain rate. The temperature and strain rate combination at the highest efficiency in the stable region provides the optimum processing condition. This has been demonstrated in this Bulletin. In some metalworking processes such as forging, strain rate varies within the workpiece. An analysis of the process with finite element method (FEM) can ensure that the strain rates at the processing temperature in the whole workpiece fall into the stable regions in the processing map. Furthermore, FEM analysis with the data from the Atlas of Formability can be coupled with fracture criteria to predict defect formation in metalworking processes.

Using the data provided by the Atlas of Formability, design of metalworking processes, dynamic material modeling, FEM analysis of metalworking processes, and defect prediction are common practice in *Concurrent Technologies Corporation*. Needs in solving problems related to metalworking processes can be directed to Dr. Prabir K. Chaudhury, Manager of Forming Department, by calling (814) 269-2594.